ABSOLUTE MEASUREMENTS OF LARGE MIRRORS

by

Peng Su

A Dissertation Submitted to the Faculty of the

COMMITTEE ON OPTICAL SCIENCES(GRADUATE)

In Partial Fulfillment of the Requirements
For the Degree of

DOCTOR OF PHILOSOPHY

In the Graduate College

THE UNIVERSITY OF ARIZONA

2008

THE UNIVERSITY OF ARIZONA
GRADUATE COLLEGE

As members of the Dissertation Committee, we certify that we have read the dissertation

prepared by   Peng Su

entitled Absolute Measurements of Large Mirrors

and recommend that it be accepted as fulfilling the dissertation requirement for the

Degree of Doctor of Philosophy

_____Jose Sasian_____	Date: Nov. 5, 2007
_____James H. Burge_____	Date: Nov. 5, 2007
_____Russell Chipman_____	Date: Nov. 5, 2007
_____Hurbert Martin_____	Date: Nov. 5, 2007
_____	Date:

Final approval and acceptance of this dissertation is contingent upon the candidate's
submission of the final copies of the dissertation to the Graduate College.

I hereby certify that I have read this dissertation prepared under my direction and
recommend that it be accepted as fulfilling the dissertation requirement.

_____Jose Sasian_____ Date: 4-24-08
Dissertation Director:

STATEMENT BY AUTHOR

This dissertation has been submitted in partial fulfillment of requirements for an advanced degree at the University of Arizona and is deposited in the University Library to be made available to borrowers under rules of the Library.

Brief quotations from this dissertation are allowable without special permission, provided that accurate acknowledgment of source is made. Requests for permission for extended quotation from or reproduction of this manuscript in whole or in part may be granted by the copyright holder.

SIGNED: Peng Su

ACKNOWLEDGEMENT

me to be involved in the New Solar Telescope (NST) project, the Giant Magellan Telescope (GMT) project, and the Discovery Channel Telescope (DCT) project, among others. The work covered in my dissertation focuses on the research I did while studying with Dr. Burge who is both very smart and wise with experience. He always offered good insight and creative suggestions towards the research I was involved in. In addition, he is an excellent mentor. Dr. Burge was always willing to spend time to discuss research problems with his students and he often took the time to organize many interesting outdoor events for his students. I really enjoyed working with him.

I would like to thank Professor Roger P. Angel. I did the TPF project and sunshade design to address global warming for him. Dr. Angel is full of enthusiasm about research and has fantastic insight to many different problems, even though he is involved in numerous research subjects each day. He impressed me very much and inspired me a lot.

I would like to thank the scientists, opticians, engineers and technicians in the Large Optics Facility and SOML at the University of Arizona. The success of the experiments in this dissertation is a direct result of their help.

I would like to thank my other committee members: Professor Hubert M. Martin and Professor Russell A. Chipman. They spent a lot of time reviewing my dissertation and offered me many good suggestions for improving my work. Moreover, I was able to work with each of them on separate projects, allowing me to learn from their individual experiences as well.

I would like to thank the people in the Sasián and Burge research groups. We spent lots of good time together. Many of them helped me a lot in my research and also offered valuable help with the revision of this dissertation.

Most importantly, I would like to thank my parents Furong and Yuhua, my sister Na, and my wife Lirong. Studying abroad has given me the opportunity to be involved in state-of-the-art research. However, this opportunity comes at the expense of time I should and could spend with my parents and sister. I know they miss me very much, just as I miss them. In our phone calls, they always encourage me to work hard and insist that I not worry about them. They are a key resource in my success as a student at the University of Arizona. I met my wife Lirong when we enrolled as graduate students at the College of Optical Sciences in 2003, and we got married in 2007. She is the most important person in my life. When I encounter problems in my research, get confused, or have to stay late in the lab, she offers a new point of view and asks me to consider things from a different perspective. When I get tired or upset, she is there to encourage me and offer me help with my experiments. It is her love and support that has helped to make this dissertation possible.

To My Wife

Lirong Wang

TABLE OF CONTENTS

LIST OF FIGURES

LIST OF TABLES

ABSTRACT

The ability to produce mirrors for large astronomical telescopes is limited by the accuracy of the systems used to test the surfaces of such mirrors. Typically the mirror surfaces are measured by comparing their actual shapes to a precision master, which may be created using combinations of mirrors, lenses, and holograms. The work presented here develops several optical testing techniques that do not rely on a large or expensive precision, master reference surface. In a sense these techniques provide absolute optical testing.

The Giant Magellan Telescope (GMT) has been designed with a 350 m^2 collecting area provided by a 25 m diameter primary mirror made out from seven circular independent mirror segments. These segments create an equivalent f/0.7 paraboloidal primary mirror consisting of a central segment and six outer segments. Each of the outer segments is 8.4 m in diameter and has an off-axis aspheric shape departing 14.5 mm from the best-fitting sphere. Much of the work in this dissertation is motivated by the need to measure the surfaces or such large mirrors accurately, without relying on a large or expensive precision reference surface.

One method for absolute testing describing in this dissertation uses multiple measurements relative to a reference surface that is located in different positions with

respect to the test surface of interest. The test measurements are performed with an algorithm that is based on the maximum likelihood (ML) method. Some methodologies for measuring large flat surfaces in the 2 m diameter range and for measuring the GMT primary mirror segments were specifically developed. For example, the optical figure of a 1.6-m flat mirror was determined to 2 nm *rms* accuracy using multiple 1-meter sub-aperture measurements. The optical figure of the reference surface used in the 1-meter sub-aperture measurements was also determined to the 2 nm level. The optical test methodology for a 1.7-m off axis parabola was evaluated by moving several times the mirror under test in relation to the test system. The result was a separation of errors in the optical test system to those errors from the mirror under test. This method proved to be accurate to 12nm *rms*.

Another absolute measurement technique discussed in this dissertation utilizes the property of a paraboloidal surface of reflecting rays parallel to its optical axis, to its focal point. We have developed a scanning pentaprism technique that exploits this geometry to measure off-axis paraboloidal mirrors such as the GMT segments. This technique was demonstrated on a 1.7 m diameter prototype and proved to have a precision of about 50 nm *rms*.

CHAPTER 1

INTRODUCTION

1.1. BACKGROUND

The demand for an increase in theoretical telescope resolution and light gathering power translates into a demand for high quality and large aperture optics that often are strongly aspheric in shape. An example of a telescope with a large aperture is the Giant Magellan Telescope (GMT) (Burge *et al*. 2006; Johns 2006) which is designed with a large segmented mirror that is 25 m in diameter. The GMT primary mirror comprises six off-axis mirror segments surrounding a central on-axis segment; each segment is 8.4 m in diameter. The segments create a mirror equivalent to an f/0.7 paraboloidal primary. The outer segments have an off-axis aspheric shape with a maximum aspheric departure of 14.5 mm from the best-fitting sphere. The fabricating of the GMT segments posses many new challenges to optical testing and optical metrology.

The main test system to be used to test the off-axis segments of the GMT employs two tilted spherical mirrors and a computer generated hologram (CGH) that act together as a null corrector. The accuracy of this test system highly depends on the alignment of all the system components. However, two other independent and absolute tests have been designed for verifying and validating the measurement of the main test. These include a so-called shear test and a scanning pentaprism test. Due to the off-axis asphericity of the

GMT segments, many new testing issues have been encountered and they have been solved for these two tests. At the time of this writing the first GMT mirror is under coasting and generating the shape. We have demonstrated the two tests by measuring the New Solar telescope (NST) primary mirror (Martin, *et al*. 2006), which is a 1.7m off-axis parabola or a 1/5 scaled version of the GMT off-axis segment.

In addition to the contributions made for testing large aspheric mirrors, the testing of large flat mirrors is also an important topic addressed in this dissertation. An algorithm that is based on the Maximum Likelihood (ML) method has been developed for processing testing data from a 1.6m flat mirror. This algorithm has also been successfully applied to reduce the data of the shear test mentioned above.

In all, the ML algorithm, the absolute testing of large flat mirrors, and the two absolute verification tests for the GMT off-axis segments are the technical contributions of this dissertation.

1.2. WORK IN THIS DISSERTAION

The technical contributions in this dissertation were made to support several optical fabrication projects at the University of Arizona optics shops and Steward Observatory Mirror Lab (SOML). These projects are the fabrication of a 1.6 m flat mirror, the fabrication of a 1.7 m off-axis parabolic mirror, and the fabrication of the first GMT off-axis parabolic segment. The metrologies developed are mainly used to determine optical surface shape in low and mid-frequency region, instead of surface roughness.

1.2.1. ABSOLUTE TESTING OF LARGE FLAT MIRRORS

As the size of an optical flat mirror to be fabricated becomes larger, its testing with a reference flat surface of equal or larger size becomes expensive. Sub-aperture testing has been a practical approach proposed for testing large flats using a smaller reference flat surface (Kim and Wyant 1981; Bray 1997). A 1.6m flat mirror was recently fabricated in the large optical shop at the College of Optical Sciences at the University of Arizona. A sub-aperture Fizeau interferometric test with a 1 m reference flat was setup to measure the 1.6 m flat mirror. The ML method (Su *et al.* 2006) was used to separate the optical figure error in the reference surface from the error in the mirror under test. The method also stitched the sub-aperture measurements to give the full aperture figure of the 1.6m flat mirror to an accuracy of 2 nm. This test is absolute in that optical figure is determined accurately without a precision master surface.

1.2.2. VERIFICATION TEST: SHEAR TEST

Interferometers with additional null test optics are frequently used for measuring aspherical optical surfaces. In optical testing, it is desirable to separate the figure measurement errors due to the test surface from figure errors that arise in the test equipment. When the optics under test has axially symmetry, error separation is accomplished by rotating the optics being measured with respect to the test system (Parks 1978; Burge *et al.* 2006). The measurement data can then be processed to separate the non-axially symmetric errors that are fixed in the test system. The axially symmetric figure errors cannot be distinguished with this technique.

In this dissertation, we present a variation of above technique for testing off-axis aspheric optics. The rotations here are performed by rotating the test surface about the optical axis of its parent surface, which may be outside the physical boundary of the test surface itself. As these rotations cannot be large, this motion is better described as a rotational shear of the optical surface with respect to the test optics. By taking multiple measurements with different amounts of rotational shear and using the maximum likelihood method for data processing, we separated the errors in the test optics from the irregularity in the optical surface under test. This rotational shear test was used to verify a null test measurement of a 1.7 m off-axis parabola and demonstrated to be accurate to 12 nm *rms*. The testing results from the shear test were consistent with the alignment error found in the null test.

1.2.3. VERIFICATION TEST: SCANNING PENTAPRISM TEST

The 1.7m NST primary mirror has been tested using an optical reference system created by a scanning pentaprism assembly (SPA). The SPA uses collimated light reflected from pentaprisms to project reference beams of light onto the NST primary mirror. When these beams are focused by the NST mirror, they provide information on low-order optical errors that would come from the mirror shape. The scanning pentaprism test has been successfully used for testing large flat mirrors (Yellowhair *et al.* 2007, Mallik *et al.* 2007) and axis-symmetric optical mirrors (Burge 1993). The work in this dissertation addresses some field aberration effects that arise in the SPA when an off-axis parabolic surface is tested. For example, the in-scan direction in mirror space, which is the direction for measuring the surface slope, is no longer maintained in the same direction during one scan. Different scans need to be well-combined so that the same field of view is measured during testing. This and other issues of the SPA test are discussed and solved in this dissertation.

1.3. ORGANIZATION OF THE DISSERTATION

This dissertation is organized into six chapters. Chapter 1, the introduction, gives a brief overview of the work in the dissertation. Chapter 2 reviews the history of absolute and sub-aperture testing, and also explains the basic principle of the ML method. Chapters 3-5 discusses in detail the testing methodology used for the measurement of the 1.6 m flat mirror and the two verification tests. The dissertation concludes with a summary and a prospect for future work.

CHAPTER 2

REVIEW OF ABSOLUTE TESTING AND SUB-APERTURE TESTING METHODS AND INTRODUCTION OF MAXIMUM LIKELIHOOD METHOD

Optical engineers occasionally face the need for fabricating an optical component to an accuracy better than the accuracy of the optical reference available. In addition, engineers test some optical components using a reference smaller than the test aperture. The basic principles of some well-known absolute test methods are reviewed in the first Section of this Chapter. Sub-aperture testing is an important approach for measuring surfaces with large apertures, fast numerical apertures, or certain aspheric surfaces. Some major developments of sub-aperture testing are discussed in Section 2. In Section 3 the principles of the Maximum Likelihood (ML) method are introduced. This method provides a general way of combining multiple interferometric testing data, and its applications are the focus of Chapter 3 and Chapter 4.

2.1. ABSOLUTE TESTING

Some optical components are required to be made more accurately than the available reference optics. This necessitates the use of absolute testing techniques (Schulz and Schwider 1967) so that the inaccuracies in the reference optics can be separated from the inaccuracies in the component being tested.

2.1.1. LIQUID FLAT TEST

Some of the earliest absolute testing techniques attempted to use a liquid flat (Barrell and Marriner 1948). It was assumed that at equilibrium the surface of the liquid has the same radius of curvature as that of the Earth or 6371 km. The deviation from a perfect flat can be calculated and removed from the test or can even be ignored for some applications. One successful example of a liquid flat test was the testing of a 240 mm diameter optical surface to an accuracy better than $1/100\lambda$ (Powell and Goulet 1998). However, a liquid flat test has some limitations. The liquid needs to satisfy certain requirements such as having high viscosity and low vapor pressure. The main drawback with the liquid-surface approach is the instability problems associated with the liquid itself. Any disturbance of the liquid, resulting from, for example, removal of a dust particle or environmental vibration, would take a long time to dissipate. Another issue is that electrostatic charges accumulate in the liquid and can be influenced by the proximity of the test surface. The static electricity charge can perturb the shape of liquid surface (Sprowl 2006).

2.1.2. SURFACE COMPARISONS

The common approach to absolute testing techniques is to compare surfaces. The traditional three-flat method can only obtain one profile of the surface each time. The modified versions of the three-flat technique try to recover the complete surfaces by either introducing more measurements, or by further making use of the test symmetry.

2.1.2.1. TRADITIONAL THREE-FLAT METHOD

In the traditional three-flat testing (Schulz and Schwider 1976), each flat is tested against another in a Fizeau fashion as shown in Fig. 2.1. The following three equations can be used to describe the test configurations:

$$A\ (x, y) + B\ (-x, y) = D\ (x, y),$$

$$C\ (x, y) + B\ (-x, y) = E\ (x, y), \tag{2.1}$$

$$C\ (x, y) + A\ (-x, y) = F\ (x, y),$$

where A, B, C = describe the individual optical surface errors,

$\quad\quad D, E, F$ = are the measured test wavefront errors.

 Since there are three equations and four unknowns—$A\ (x, y)$, $B\ (-x, y)$, $C\ (x, y)$ and $A\ (-x, y)$ —no point-by-point solution can be obtained for the total surfaces. Along the axis of inversion($x=0$), however, only three unknowns, $A\ (0, y)$, $B\ (0, y)$ and $C\ (0, y)$, remain. So this results in surface data only along a diameter determined by a single traditional three-flat test.
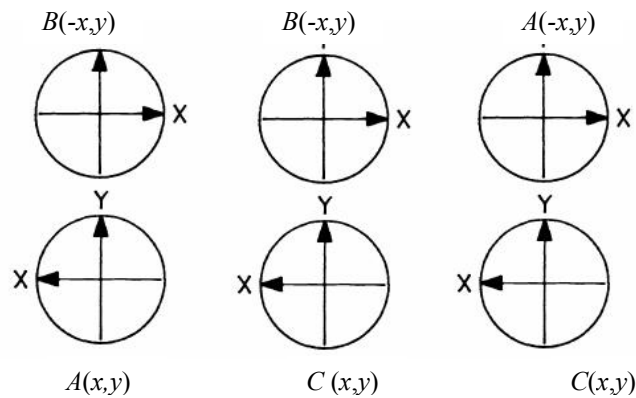
Figure 2.1 Test configurations of the traditional three-flat test

2.1.2.2. FRITZ'S METHOD

Fritz's method (Fritz 1984) is a variation of the traditional three-flat method. A fourth measurement is added with one of the flats rotating by an additional angle ϕ. Each flat surface is described by Zernike polynomials (Born and Wolf 1999). Polynomial coefficients of the surface are obtained by solving equations in a least squares sense. The method works well when smooth surfaces are being measured.

2.1.2.3. PARKS'S METHOD

Parks's method (Parks 1978) can remove rotationally asymmetric reference optics errors from the measurement. Two sets of measurements need to be taken. One is

$$W(r, \theta) = T(r, \theta) + R(r, \theta), \qquad (2.2)$$

where W = is the wavefront from the measurement,

   T = is the error contribution due to the component under test,

   R = is the error from reference optics.

The second measurement is taken after first rotating the component with respect to the reference by an azimuthal angle ϕ, then one has

$$W'(r, \theta) = T(r, \theta + \phi) + R(r, \theta). \qquad (2.3)$$

Subtracting the two measurements, one finds a shear equation

$$\Delta W = W'(r, \theta) - W(r, \theta) = T(r, \theta + \phi) - T(r, \theta). \qquad (2.4)$$

By representing the surface figure errors in the component with Zernike polynomials, Parks derives that the polynomial coefficients of the component under test can be calculated from the following equation:

$$a_l^{\pm k} = -\frac{1}{2}[\Delta a_l^{\pm k} \pm \frac{\Delta a_l^{\pm k} \sin k\phi}{(1 - \cos k\phi)}], \qquad (2.5)$$

where $a_l^{\pm k}$ = are the coefficients of the component under test

   $\Delta a_l^{\pm k}$ = are the coefficients obtained by fitting the shear data in Equation 2.4

      with Zernike polynomials.

The sensitivity of this method is discussed by Burge (1993). A plot of the sensitivity of the computed Zernike coefficients with respect to the rotation angle was given. Rotation angles of $\pm 55°$ are suggested to work well for finding all Zernike terms up to fifth order.

2.1.2.4. *N*-POSITION METHOD

The N-position method (Evans and Kestner 1996) makes use of multiple measurements with different rotation angles. Interferograms are obtained from a reference optics *R* and a test part *T*, and the test part is rotated *n* -1 times by an azimuthal angle ϕ (where $n\phi=2\pi$) relative to the reference. When the *n* phase maps are averaged, all the non-rotational symmetric errors in *T* sum to zero, except those with an angular order of *nk*, where *k* is an integer.

The average of the *n* interferograms contains three classes of errors: all the errors in *R*, the rotationally invariant errors in *T*, and the non-rotationally symmetric errors of azimuthal order *nk* (where *k* is an integer) in *T*. So an absolute measurement of the test part *T* can be obtained by subtracting the averaged data from an individual map. However, rotationally invariant errors and those with azimuthal order *nk* will be lost.

2.1.2.5. METHOD BASED ON FURTHER INVESTIGATING SYMMETRY

Fritz's method is not good at testing local irregularities in the surfaces since finite polynomials are used to represent surfaces. Ai and Wyant (1993) suggest a solution by making use of the four-fold symmetry properties of surfaces. Each point on the flat can be obtained without using the least squares method. The following shows their basic concept.

An arbitrary three-dimensional function $F(x, y)=z$ given in a Cartesian coordinate system can be expressed as a linear combination of four terms having symmetry

properties with respect to the origin of even–even, even–odd, odd–even, and odd–odd functions as described in equation 2.6.

$$z=F(x, y) =Fee+Feo+Foe+Foo \qquad (2.6)$$

Odd-even, even-odd, and even-even parts of a flat can be solved easily in traditional three-flat configuration. Odd-odd parts are obtained by adding additional measurements. Fig.2.2 shows a six-configuration measurement. In the figure, $A^{degrees}$ means surface A is rotated certain degrees, B^x is the reflection of B along x axis, and M is the measurement. By algebraic manipulation, odd-even, even-odd, even-even parts and lower order odd-odd parts of the flats can be solved completely. Higher frequency components of the odd-odd part can be obtained by adding more measurements.
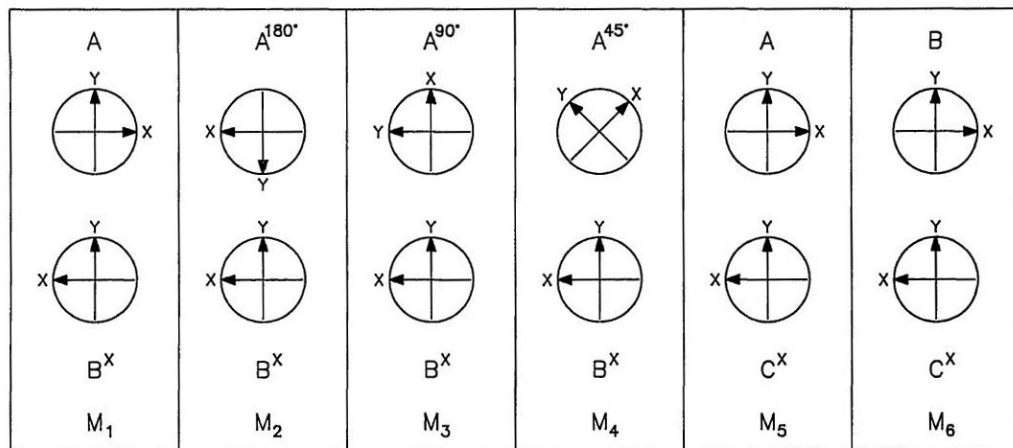
Figure 2.2 Six configurations in Ai and Wyant's method

Based on the fourfold symmetry concept and the *n*-position method, Parks gives a pixel-based solution (1998) by numerically rotating the data. Geiesmann (2006) recently also discusses a pixel-based solution using the two-fold symmetry and the *n*-position

method. Surface information measurement completeness of these two methods is both limited by the numbers of configurations being used.

2.1.3. OTHER ABSOLUTE METHODS

Another important absolute test method is the scanning pentaprism method. Light is deflected by a fixed angle (90°) when passing through a pentaprism. The exiting angle of the light is insensitive to the alignment and slight rotation of the prism. By scanning the pentaprism to different positions, an array of parallel beam can be generated, which can act as a large aperture collimated beam. The generated collimated light is useful for testing large flats (Yellowhair 2007) or parabolic mirrors where a large aperture reference beam is hard to obtain.

There are several discussions about absolute calibration for spherical surfaces in the literature. One popular method was well investigated by Karl-Edmund Elssner *et al.* (1989). One can achieve a calibration for a sphere by testing it at three positions: retro-reflection position, rotating it 180°, and the cat's eye position.

Computer generated holograms (CGH) have been widely used for testing aspheric surfaces (Burge 1993). Calibrating the aspheric wavefront generated from a CGH is receiving attention from researchers recently. One way to do the calibration is by simultaneously generating two wavefronts from the CGH by multiplexing (Reichelt *et al.* 2003). One may be a spherical wavefront, and it can be well calibrated by testing with other methods. Then the errors (due to fabrication) shown in the spherical wavefront can be transferred for calculating the errors in the aspheric wavefront.

2.2. SUB-APERTURE TESTING

Sub-aperture testing (SAT) was primarily proposed to solve the problems arising in testing large optical flats (Kim and Wyant 1981). By scanning the test part with a smaller flat, a large reference flat is replaced by an array of smaller optical reference flats. Interferograms from each smaller reference are "polluted" with misalignment errors from the small flat. The problem in SAT is then to convert sub-aperture measurement results to full aperture aberrations of the test part. This is hereafter referred to as the sub-aperture stitching problem.

SAT is not limited to testing flats. It also has been developed for measuring spherical surfaces and mild-departure aspheric surfaces. It plays an important role in solving metrology problems in testing surfaces with large aperture, fast numerical aperture, or certain aspheric surfaces.

2.2.1. KWON-THUNEN AND SIMULTANEOUS FIT METHOD

In an early version of SAT, there was no overlap between any two sub-apertures. Two approaches were presented for data reductions: the Kwon–Thunen method (1982), and the simultaneous fit method developed by Chow and Lawrence (1983). Both use Zernike polynomials to represent surfaces, and then a least squares fit of the sub-aperture data to obtain the coefficients of the test surface. A comparison of them was given by Jensen et al. (1984). Both methods suffer from the problem that polynomials are not good

at describing localized irregularities in the surfaces. And because there was no overlap between the sub-aperture data, these two methods are sensitive to alignment errors.

2.2.2. DISCRETE PHASE METHOD

To overcome the shortcomings of polynomial fitting methods, an algorithm, called the discrete phase method, was proposed by Stuhlinger (1986). The wavefront is represented not by Zernike polynomials but by phase values measured at a large number of discrete points across the aperture. The method requires that overlapping regions exist among sub-apertures. The relative piston and tilts between the reference and the test part are estimated by a least-squares (LS) fit to the differences at overlapping points. Then sub-aperture data can be combined together by adjusting the piston and tilt of adjacent sub-aperture data. This method has been developed into commercially available software (MB, Phase Mosaic).

2.2.3. NON-NULL ASPHERIC TEST

Besides testing large flats, sub-aperture testing has also been investigated as a non-null aspheric test method. By translating the reference surface or test surface, the reference sphere of an interferometer is adjusted to best match the local radius curvature of the aspheric surface under test. In certain test region, the interferogram fringes can then be reduced to within the dynamic range of an interferometer. A measurement can be taken without aliasing. The full aspheric surface can then be measured by stitching a

number of sub-aperture measurement data. To reduce the requirement for prior knowledge of fringe nulling or the alignment of sub-apertures, many iterative algorithms have been developed to estimate the positions of each sub-aperture (Chen *et al.* 2005).

2.2.3.1. ANNULAR STITCHING OF ASPHERES

One of the directions in developing non-null aspheric sub-aperture test is the annular sub-aperture test used to test rotational symmetric aspheric surfaces. By relative translation of the aspheric surface longitudinally along the optical axis of the reference sphere, different annual zones of the aspheric surface can be tested with best radius curvature match condition. A series of interferograms can be taken at different longitudinal position of the aspheric surface without fringe aliasing. All the sub-aperture data can then be stitched together to get a complete map of the aspheric surface. Issues such as sub-aperture arrangements (overlapping or complementary), data reduction methods have been widely investigated (Hou *et al.* May 2006).

2.2.3.2. GENERAL STITCHING OF ASPHERES

An important development in sub-aperture testing of aspheric surfaces was performed by QED Technologies. In 2003, QED Technologies developed a general-purpose stitching interferometer workstation (Fleig *et al.* 2003) that can automatically carry out high-quality sub-aperture stitching of flat, spherical, and mild-departure aspheric surfaces up to 200 mm in diameter. In their publications, they discussed in detail

issues encountered during sub-aperture testing including imaging distortion correction, alignment error correction, reference surface error correction, and constrained optimization in data reduction (Golini *et al*. 2003).

Stitching is realized using overlapping data. Error in the reference surface inherently creates inconsistency between the overlapping data and is an important error source in the stitching process. One way to solve this problem is calibrating the reference before using it. For example, one can use the absolute test method mentioned above to calibrate a flat, or use the method mentioned by Elssner (1989) to calibrate a spherical surface. Another way to calibrate a reference presented in QED's reference (Golini *et al.* 2003) is to use Zernike polynomials to describe the reference surface. Then data consistency in the overlap region is used as criteria to least squares fit the coefficients of the reference surface. This idea is a form of the ML method discussed below. However, the ML method discussion in the dissertation comes from a general point of view and the flexibility of ML method has been further explored, as shown in the shear test application.

2.3. BASIC PRINCIPLES OF MAXIMUM LIKELIHOOD METHOD

The maximum likelihood (ML) method provides a general way for combining multiple interferometric measurements. Given a set of data $\{y\}$, a set of physical parameters $\{x\}$ is to be estimated. If the statistics of the data $\{y\}$ are understood and if the problem in reverse (given physical parameters $\{x\}$, the values of $\{y\}$ can be calculated) is workable, then a statistical likelihood $L(x|y)$ can be created, which equals the probability

density function *pr(y|x)*. The maximum likelihood estimate is defined such that the likelihood of parameters {*x*} is maximized given the data set {*y*}.

2.3.1. LIKELIHOOD FUNCTION AND MAXIMUM LIKELIHOOD ESTIMATOR

The probability density function (PDF) *pr(y|x)* describes the sampling distribution of the data {*y*}, given parameters {*x*}, and we say that sample *y* is drawn from *pr(y|x)*. Given data {*y*}, *pr (y|x)* can be regarded as a function of *x*, called the likelihood of *x* for the given *y* and is noted by (Barrett *et al.* 2007)

$$L(x|y) = pr(y|x). \qquad (2.7)$$

The principle of maximum likelihood states that event occurrences presumably have had maximum probability of occurring (Frieden 1990). Given the likelihood law *L(x|y)* and fixed data{*y*}, {*x*} must have the property that of maximized the likelihood of occurrence of the data {*y*}. In the equation

$$L(x|y) = \text{maximum}, \qquad (2.8)$$

the set {*x*} that satisfies this condition is called the "maximum likelihood estimator."

2.3.2. STOCHASTIC MODEL

2.3.2.1 STOCHASTIC MODEL OF AN INTERFEROMETRIC MEASUREMENT

An interferometric measurement gives the optical surface figure difference between the reference surface and the surface under test. The data is usually polluted by noise such as air turbulence, environment vibration, and errors from the interferometer

itself. Normally the stochastic distribution of the interferometric data can be well described by a normal distribution based on the "law of large numbers." This assumption will be followed in the following discussions.

2.3.2.2 STOCHASTIC MODEL OF A SUB-APERTURE TEST

Multiple sub-aperture measurement data can be combined with the ML method. Surface differences (phase data) between a reference surface (A) and a part of a surface under test (B) are obtained during a sub-aperture interferometric measurement. The phase data D_{ij}, where i represents the ith sub-aperture measurement and j represents the jth phase value in a sub-aperture measurement, can be expressed as

$$D_{ij} = D_{ij}{}^a + residuals = -\sum_{p=5}^{m} A_p Z_p(x_{ai}, y_{ai}) + \sum_{p=5}^{n} B_p Z_p(x_{bi}, y_{bi}) + alignments + residuals \, ,$$

(2.9)

where $D_{ij}{}^a$ = the part of the data that can be described analytically by

         polynomials (basis functions),

    $residuals$ = the part of data that cannot be described by finite terms of

         polynomials (basis functions),

       Z = polynomials (basis functions) used to represent the surfaces, such

         as Zernike polynomials,

    m and n   =the indexes of the highest polynomial terms used for representing

         surface A and B,

$x_{ai}, \, y_{ai}, \, x_{bi}, \, y_{bi}$ = the global coordinates of surface A and B in a sub-aperture

measurement,

alignments = the terms describing the phase errors introduced by the alignment

such as piston, x tilt, y tilt and defocus.

The surface figure errors in A and B can be calculated by knowing the coefficients A_p

and B_p.

When the noise of the data is independent and identically distributed (*i.i.d*) and

residuals are small enough to be ignored, the likelihood function of a sub-aperture test

can be written as,

$$L(A_p, B_p \mid D_{ij}) = (\sqrt{2\pi}\sigma)^{-uv} \exp[-\frac{1}{2\sigma^2} \sum_{i=1}^{u} \sum_{j=1}^{v} (D_{ij} - D^a{}_{ij})^2] \qquad (2.10)$$

where σ = the standard deviation of the sub-aperture measurement, here

assumed to be equal in each measurement,

u = the number of sub-aperture measurements,

v = the number of phase data in the ith sub-aperture measurement.

By maximizing the logarithm of the likelihood $L(A_p, B_p \mid D_{ij})$, equation 2.11 is obtained

for finding A_p and B_q.

$$\sum_{i=1}^{u} \sum_{j=1}^{v} (D_{ij} - D^a{}_{ij})^2 = \sum_{i=1}^{u} \sum_{j=1}^{v} (D_{ij} + \sum_{p=5}^{m} A_p Z_p(x_{ai}, y_{ai}) - \sum_{p=5}^{n} B_p Z_p(x_{bi}, y_{bi}) - alignments)^2$$

$$= minimum \qquad\qquad\qquad (2.11)$$

Coefficients A_p and B_q can be obtained from Equation 2.11 with a least squares estimate.

If the standard deviation of each sub-aperture measurement is different, data from each

measurement has a different weight factor. The problem can then be solved as a weighted

LS problem.

The above derivations can be written into matrix form. The polynomial

coefficients of the surfaces and the alignment coefficients form a column vector x:

$x=$ [coefficients of surface A, coefficients of surface B, alignment coefficients]'.

$$(2.12)$$

Phase data of the sub-aperture measurements constitute a column vector y:

$$y= [D_{11}, D_{12}, ..., D_{uv}]'. \qquad (2.13)$$

A matrix M describing the relation in equation 2.9 can be construct to connect vectors x

and y. So a sub-aperture test can be modeled as

$$y=M \cdot x. \qquad (2.14)$$

Chapter 3 explains in detail the structure of the matrix M for the case of combining sub-

aperture data.

2.3.3. NUISANCE PARAMETERS AND NULL FUNCTIONS

One type of nuisance parameters is the parameters that influence the data but that

are of no interest for estimation (Barrett *et al.* 2007). For example, each sub-aperture

measurement data has different piston, tilt, and defocus due to the alignment. The

alignment errors affect the phase data; however, their exact values are of no interest in the

test. Another type of nuisance parameters is parameters in which we are interested, but

may not be well handled in the model. An example of that is when finite Zernike

polynomials are used to represent the surfaces; there exists residuals of the surfaces that

cannot be well described by finite Zernike polynomials. The residuals are the intrinsic nuisance parameters of our test.

Null functions are functions that do not influence the data and in principle cannot be determined from the data. For example, the rotational symmetric errors in the test system cannot be measured with Parks's method; they fall in the null space of that test. We refer to any data that falls into the null space as "ambiguous" because we cannot estimate its origin.

2.3.4. VARIANCE PROPAGATION MODEL AND CROSSTALK ISSUE

Equation 2.14 is solved in a least squares sense. With the independent Gaussian distribution of the phase data, the variance associated with the estimate coefficients x_q can be calculated from equations 2.15 (Press *et al.* chapter 15.4 1986; Appendix A)

$$\sigma^2(x_p) = C_{kk} \cdot \sigma_{y_q}^2$$

$$\boldsymbol{C} = (\boldsymbol{M^T M})^{-1} \tag{2.15}$$

where C_{kk} = the diagonal elements of the covariance matrix $\boldsymbol{C}$,

x_p and y_q = the elements in the column vectors $\boldsymbol{x}$ and $\boldsymbol{y}$.

The off-axis elements of matrix C describe the effect of crosstalk between different parameters to be estimated. The smaller the off-axis values are, the more linearly independent the parameters are, and the less coupling between different parameters occurs in the data.

Considering the estimation ability and crosstalk issue, several design strategies are worth paying attention to when designing a test system, which is represented by

matrix $\boldsymbol{M}$.

1. Choose basis function to efficiently represent the measurement data

The choice of basis functions is important. Ideally an orthogonal basis set that fully describes the physical range of data $\{y\}$, but poorly depicts the noise is preferred. Usually a prior knowledge of the surface is used to choose basis functions. Zernike polynomials are an example of the basis functions used to describe a reference surface and test surface. Based on surface shape or specific errors in the surface, another type of basis functions may work better to represent the data, giving a better estimate and less crosstalk. For example, for square shape surfaces, Legendre polynomials are orthogonal in the data region and can give less crosstalk. Also, in Chapter 3, when the 1.6m flat was measured, more rotational symmetric terms of the Zernike polynomials were chosen to represent the test surface, instead of using all the Zernike polynomial terms in order, because there are more rotational symmetric errors in the surface due to the fabrication method.

2. Choose the test geometry to minimize crosstalk and make parameter estimates more reliable

For a sub-aperture test, this guides one to design the sub-aperture test geometry, addressing the number of sub-aperture measurements and how they should be distributed. The test geometry of the 1.6m flat measurement (described in Chapter 3) is an example of this approach. Both the test flat and the reference flat were rotated during sub-aperture measurements. With this test geometry, parameters of the test flat and reference flat can be estimated independently; the crosstalk between them was minimized.

3. Investigate the higher order residual coupling

With finite numbers of polynomials representing the data, there will be higher order surface residuals. The residuals will alias and affect the estimate of the lower order terms. They can be checked by computing the $C_{kk'}$, the off-diagonal elements of the covariance matrix C, where k is related to the lower order terms to be estimated and k' corresponds to the higher order terms, which are not included in the basis functions during the test. If the $C_{kk'}$ is large enough, the corresponding higher order terms need be included to the basis functions.

2.4. SUMMARY

Developments in the absolute flat testing are first reviewed. These include liquid flat test, the traditional three-flat test and its modified versions. Sub-aperture testing, an important approach for measuring surfaces with large apertures, fast numerical apertures, or with certain asphericity, is discussed in following and its progress is reviewed. After that, the ML method, which offers a general way to combine multiple measurements, is introduced. The applications of the ML method, absolute sub-aperture testing of a 1.6m flat and verify an off-axis surface with a rotational symmetric parent (shear test), are the topics of the Chapters 3 and 4.

CHAPTER 3

ABSOLUTE MEASUREMENT OF A 1.6 METER FLAT WITH THE MAXIMUM LIKELIHOOD METHOD

3.1. INTRODUCTION

A 1.6m flat mirror was fabricated in the large optics shop at the College of Optical Sciences. A Fizeau interferometer with a 1m transmission reference flat was set up for the test. Multiple sub-aperture measurements were taken to get full aperture surface information for the test flat mirror, and the maximum likelihood (ML) method was used to combine the sub-aperture data and to remove errors introduced by the reference surface from the flat test data. The test setup and data collection are described in Section 3.2. Data reduction using the ML method is described in Section 3.3. The measurement results and the error analysis are given in Section 3.4 and 3.5. The comparison between the ML method and other data reduction methods is discussed in Section 3.6.

3.2. BASIC PRINCIPLES OF THE SUB-APERTURE FIZEAU TEST

3.2.1. SUB-APERTURE FIZEAU INTERFEROMETER SETUP
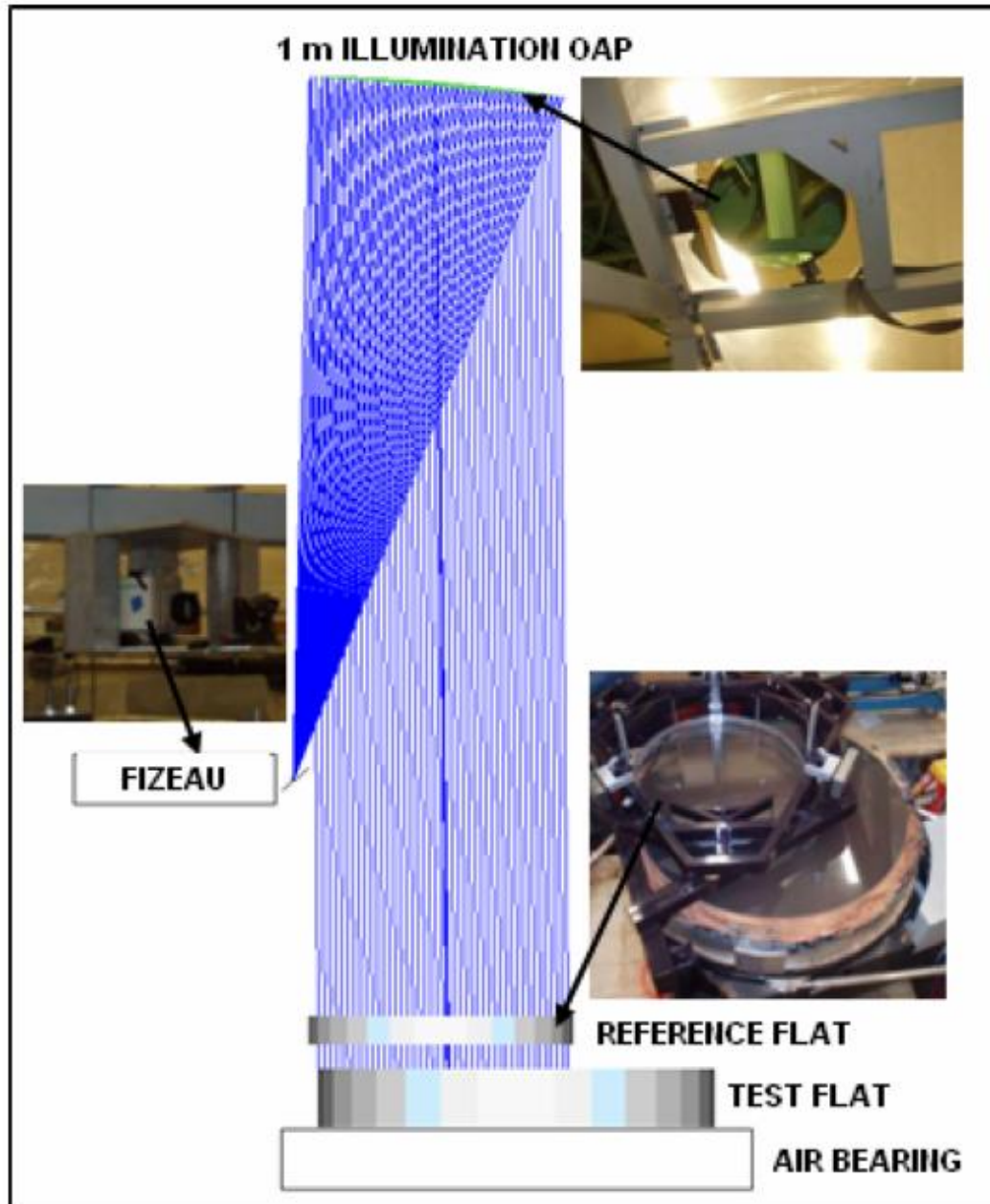
Figure 3.1 Sub-aperture Fizeau interferometric test setup

A Fizeau interferometer was set up to test the 1.6m flat as shown in Fig. 3.1(Yellowhair 2007; Sprowl 2006). Light from the instantaneous Fizeau interferometer was focused by an F/1.5 reference sphere to generate a point source for a 1m F/3.1 off-axis parabola (OAP). Collimated light from the OAP was partially reflected by a 1m fused silica transmission reference flat. Part of the light was transmitted through the reference surface and was reflected by the test mirror. These two beams of the light pass back to the interferometer and interfere with each other. The interferograms were processed using the Intelliwave™ interferogram analysis software, which determined the optical path difference between the reference and test surface.

The test flat was set up on a rotary air bearing table, which could rotate via computer control to an accuracy of 0.001 degree. The reference flat, 5/8 of the size of the test flat, was mounted to a frame with three feet. The reference flat and frame sit on top of another frame with six mounting pads spaced 60 degree apart. By mounting the reference flat at different pad locations, the reference can be rotated relative to the test flat. As shown in Fig 3.1, in the setup, the reference flat was placed so that it could overlap the edge of the test flat. By rotating the test flat using the air bearing table and taking multiple sub-aperture measurements, a full map of the test surface was obtained by stitching the sub-aperture measurements together. Further rotating the reference flat relative to the test flat allowed the figure errors in the reference to be removed. In fact all irregularities in both surfaces can be determined to the noise limit with the exception of power. Power, which is equivalent with curvature, cannot be determined from the data, and it falls into the null space of this test. The effect of power from either surface would

be constant for all data sets. However the difference in power between the two surfaces can be determined. In practice, a second measurement, the scanning pentaprism test (Yellowhair 2007), was used to determine power in the 1.6m flat.

3.2.2. INTERFEROMETER ABERRATION

One special part of the instantaneous interferometer (Intellium H1000) used here is that two orthogonally polarized beams (A and B) with a small angular shear between them, are employed for realizing instantaneous phase shifting. Light reflected back from the reference surface needs to have a different polarization state from the light coming back from the test surface. Since an OAP was included as part of the interferometer in our setup, the two polarized beams in fact followed a slightly different path through the OAP. This path difference between the reference and test beam generated ~ 82nm aberrations, which was mostly astigmatism, showed up in the interferogram. To eliminate this system error, two measurements were taken for each sub-aperture measurement. One with the polarized beam *A* reflected from the reference surface and the polarized beam *B* reflected from the test surface. The second measurement was done reversing the order of the beams. The aberration from the OAP was then cancelled out by averaging these two measurements.

3.2.3. INTERFEROMETER DISTORTION CORRECTION

Optics in the interferometer combined the light from reference and test surfaces to generate interference fringes. They also functioned as imaging optics to image the interferogram to the detector. As the interferometer imaging system was composed of an OAP, there was significant imaging distortion present. A simulation of the imaging effect in optical design software agreed with the imaging result from the real system with a fiducial mask placed on top of the reference surface shown in Fig. 3.2. The regularly distributed holes at the reference surface plane were imaged to an irregular distribution at the detector plane due to the distortion. The mapping relation was obtained by measuring the coordinates of the holes and the corresponding coordinates of the holes images at the detector. A least squares fit was used to find the coefficients of the polynomials for the mapping, and the inverse mapping was then applied to the phase map obtained from the interferometric measurement for correcting distortion effects (Zhao *et al.* 2006).
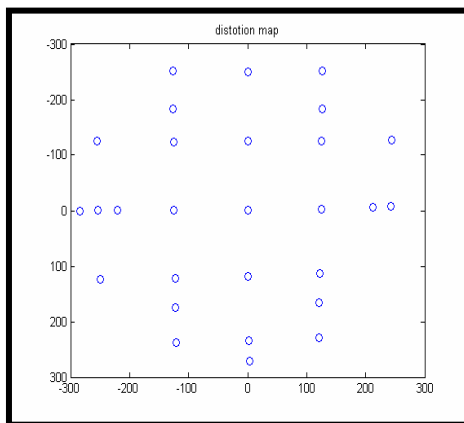
Figure 3.2 Distorted fiducial image

3.2.4. GEOMETRY OF THE 1.6M FLAT SUB-APERTURE TEST
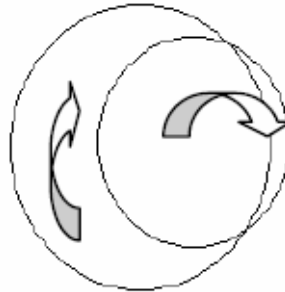
Figure 3.3 Geometry of 1.6m flat sub-aperture test

The position of the mirror under test relative to the reference surface is shown in Fig. 3.3. In the figure, the reference flat is represented by the small circle, while the test mirror is represented by the large circle. The combination of the rotation of the reference surface and the rotation of the test surface gave information to separate the errors in the reference surface from the errors in the test surface. In the final measurement of the 1.6m flat, 24 sub-aperture measurements were taken to reduce the noise effects. Both reference and test flats were rotated following an arrangement as shown in Table 3.1 to well sample both surfaces.

Table 3.1 Sub-aperture measurement arrangement

Reference flat rotation (degree)	0				60				120			
Test flat rotation (degree)	0	90	180	270	15	105	195	285	30	120	210	300
Reference flat rotation (degree)	180				240				300			
Test flat rotation (degree)	45	135	225	315	60	150	240	330	75	165	255	345

3.2.5. COORDINATES OF THE SUB-APERTURE MEASUREMENTS

To stitch the sub-aperture measurements together, the position of each sub-aperture relative to the test surface needed to be well known. They were determined by knowing the rotation angles and the centers of the reference and test surfaces. The rotation angles of the 1.6m flat were well controlled by the accuracy of the air bearing. The rotation angle of the reference flat was determined by its kinematic mount. Fiducial marks were drawn on the centers of each surface and imaged by the interferometer along with the phase map. From the fiducial images, the positions of the centers were known to less than 1.6mm accuracy (half pixel of the detector).

Since there was data overlap between each sub-aperture measurement in current measurement arrangement, the geometry information, rotation angles and coordinates of centers, were further determined by optimizing them to maintain the data consistency within the overlapping region. Monte Carlo simulations were performed to check the results of the optimization. A standard deviation (*std*) (1.6 mm/semi-diameter) of the mirror rotational angular errors and a std of 1.6 mm random lateral shifts or uncertainties in determining the center of each surface were introduced to the sub-aperture measurement data. By optimizing the structures of the influence matrix M explained in later Section, the geometric errors were well reduced and the estimation error of the surfaces was able to be controlled to less than 0.5 nm (Su *et al*. 2006).

3.2.6. DATA COLLECTION PROCEDURE

The measurement data was collected by Robert Sprowl (2006). The data collection procedure was as follows:

1. Tip and tilt the reference and test surface to get two sets of phase measurements with different polarization combination,

2. Correct the distortion of the phase maps,

3. Average two polarizations to remove aberration of the interferometer,

4. Gather fiducial coordinate information,

5. Supply the phase data to ML data reduction program.

3.3. ML DATA REDUCTION

In the 1.6m flat test setup, the available data were multiple sub-aperture measurements that included the errors from both reference and test surfaces. The goals were to estimate the full aperture surface figure of the test flat and to separate the errors introduced by the reference surface. With the ML method, polynomials were used to describe figure errors of the reference and test surface. By solving for the polynomial coefficients, estimates of the surfaces were obtained. From a mathematical point of view, by relatively translating and rotating the two surfaces, simultaneous equations can be generated. Then the coefficients of each surface can be solved from these over-determined equations.

3.3.1. BASIC PRINCIPLE OF THE ML DATA REDUCTION

Figure differences (Phase data) between the reference and the test surface are measured in each sub-aperture measurement. The phase data D_{ij}, where i represents the ith sub-aperture measurement and j represents the jth phase value in this sub-aperture measurement, can be described by

$$D_{ij} = D_{ij}{}^{a} + residuals = P_i Z_1(\rho_a, \theta_a + \phi_{ai}) + Tx_i Z_2(\rho_a, \theta_a + \phi_{ai}) + Ty_i Z_3(\rho_a, \theta_a + \phi_{ai})$$

$$+ De_i Z_4(\rho_a, \theta_a + \phi_{ai}) - \sum_{p=5}^{m} A_p Z_p(\rho_a, \theta_a + \phi_{ai}) + \sum_{p=5}^{n} B_p Z_p(\rho_b, \theta_b + \phi_{bi}) + residuals,$$

$$(3.1)$$

where $D_{ij}{}^{a}$ = data can be represented analytically,

         m = the number of the highest Zernike terms for surface A (reference

            surface),

         n = the number of the highest Zernike terms for surface B (test

            surface),

         Z   = Zernike polynomials,

    ϕ_{ai} and ϕ_{bi} = rotation angles of surface A and B respectively,

$P_i, Tx_i, Ty_i,$ and De_i = the amount of piston, x tilt, y tilt and defocus of the ith sub-

            aperture measurement,

     A_p and B_p = aberration coefficients of the reference and test surface.

As in the analysis in Chapter 2, the problem is to find the Zernike polynomial coefficients such that

$$\sum_{i=1}^{u}\sum_{j=1}^{v} (D_{ij} - D_{ij}^{a})^2 = mininum \qquad (3.2)$$

where u = the number of the sub-aperture measurements,

  v = the number of the phase data (sampling point) in ith sub-aperture

measurement.

3.3.2. MATRIX FORM

The problem above can be expressed in matrix form. A column vector x can be composed by the coefficients of the surfaces and the alignments as in equation 3.3.

  x= [coefficients of surface A, coefficients of surface B, alignment coefficients]'

$$(3.3)$$

The phase data from each sub-aperture measurement can form a phase data vector φ_i, where

$$\varphi_i = [D_{i1}, D_{i2}, \ldots, D_{iv}]'. \qquad (3.4)$$

In the experiment, each of the 24 sub-aperture measurements had 1024×768 pixels. To reduce the storage and computation requirement in data reduction process, the sub-aperture phase data vector φ_i was compacted by fitting the phase data with sub-aperture basis functions U_i as in equation 3.5.

$$y_i = (U_i)^{-1}\varphi_i. \qquad (3.5)$$

where y_i = compacted phase data vector.

The basis functions U_i are orthogonal in the sub-aperture region, numerically generated by the singular value decomposition (SVD) method. To generate basis functions U_i, first

a matrix T is created. The kth column of T is obtained by evaluating the kth Zernike polynomial at the coordinates of the phase data in the ith measurement. With matrix T, SVD is then used to decompose T to get basis functions U_i:

$$T = U_i S_i V_i' , \qquad\qquad (3.6)$$

where U_i = is a unitary matrix with orthogonal columns in the sub-aperture region.

Phase data in the sub-aperture region can be expressed as the linear combination of each column of matrix U_i as the number of Zernike polynomials used to create T goes to infinity or large enough. U_i is the set of basis functions of the ith sub-aperture measurement.

With all the y_i, a data vector y can be built as in equation 3.7:

$$y = [y_1, y_2, \ldots, y_u]' , \qquad\qquad (3.7)$$

where u = the number of the sub-aperture measurements.

To satisfy Equation 3.1, terms on the right side of the equation also need to be fitted by the basis functions U_i. In ith sub-aperture measurement, each polynomial (both surface and alignment polynomials) is first evaluated at the coordinates of the phase data. The values obtained forms a column vector Z_{it} (t=1-4, 5-m evaluated at surface A coordinates, 5-n evaluated at surface B coordinates). Then as in Equation 3.8, Z_{it} is fitted by U_i to get a compacted vector ZC_{it}.

$$ZC_{it} = (U_i)^{-1} Z_{it} \qquad\qquad (3.8)$$

All the ZC_{it} can then form a sub-matrix M_i as in Equation 3.9.

$$M_i = [\, ZC_{i1}, ZC_{i2}, \ldots ZC_{i4}, ZC_{i5A}, \ldots ZC_{imA}, ZC_{i5B}, \ldots ZC_{inB}]\ (3.9)$$

where $ZC_{i1}, ZC_{i2}, \ldots, ZC_{i4}$ = correspond to alignment polynomials,

$$ZC_{i5A,...,}\, ZC_{imA} \qquad = Z_{it} \text{ evaluated at surface } A \text{ coordinates (t=5-m)},$$

$$ZC_{i5B,...,}\, ZC_{inB} \qquad = Z_{it} \text{ evaluated at surface } B \text{ coordinates(t=5-n)},$$

For all the sub-aperture measurements, M_i forms the system matrix M.

$$M = [M_1, M_2, \ldots, M_u]' \tag{3.10}$$

where u = the number of the sub-aperture measurements.

The relationship in Equation 3.1 can then be expressed in its matrix form as in Equation 3.11.

$$y = M \cdot x \tag{3.11}$$

3.3.3. ML DATA REDUCTION PROCESS

Fig. 3.4 shows the flow diagram of the ML data reduction process. Distortion corrected sub-aperture measurement data and the test geometry are used as input information. Numerical orthogonal basis functions are created to describe the data within the sub-aperture region. From the test geometry, the system matrix M is assembled, which describes the influences produced by the reference and test surface to each sub-aperture measurement. With taking a matrix inverse of the system matrix, Equation 3.11 is solved and both the reference and test surface shapes are obtained. By checking the fitting residuals, the test accuracy can be estimated. Setting up a merit function with fitting errors allows sub-aperture measurement geometry uncertainties to be controlled by optimizing the structures of the system matrix.

```
                    ┌────────────────────────────────────┐
                    │  Take interferometric measurement  │
                    └────────────────────────────────────┘
                                      │
                                      ▼
┌──────────────────────┐   ┌────────────────────────┐
│ Use fiducial         │   │   Correct distortion   │
│ measurement          │──▶│                        │
│ to determine mapping │   └────────────────────────┘
└──────────────────────┘              │
                                      ▼
┌──────────────────────┐   ┌────────────────────────────────────┐
│ Using SVD to         │   │ Represent data using orthogonal    │
│ determine            │──▶│ basis                              │
│ orthogonal basis     │   └────────────────────────────────────┘
│ for the data         │              │
└──────────────────────┘              ▼
┌──────────────────────┐   ┌────────────────────────────────────┐
│ Use geometry         │   │ Apply ML method to estimate        │
│ information           │──▶│ surfaces and alignment terms       │
│ to generate matrix M │   └────────────────────────────────────┘
└──────────────────────┘
        ▲                             │
        │                  Optimize   ▼
┌──────────────────────┐   ◀──────────
│ Estimate correction  │
│ to geometry          │
└──────────────────────┘
                                      │
                                      ▼
                           ┌────────────────────────┐
                           │ Optimal estimates,     │
                           │ Residuals from estimate│
                           └────────────────────────┘
```

Figure 3.4 Flow diagram of ML data reduction process

3.3.4. NUISANCE PARAMETERS AND NULL SPACE OF THE TEST

Parameters associated with the alignment terms, including piston, tilts, and defocus, are parts of the nuisance parameters in the ML data reduction process. Also, as in Equation 3.1, each surface is described by Zernike polynomials:

$$W = \sum_p A_p Z_p(\rho, \theta) + residuals \qquad (3.12)$$

where W = represents surface errors

   $residuals$ = are the errors that can not be represented by the Zernike polynomials

used.

Here the residuals are the information of interest; however, it cannot be obtained from the estimate. They also belong to nuisance parameters. Singular value decomposition of the system matrix *M* gives the null space of the matrix, which corresponds to the null space of the test. For instance, the power of each surface cannot be estimated from the sub-aperture test. The power of the test flat was measured separately by a scanning pentaprism test (Yellowhair *et al*. 2007).

3.4. MEASUREMENT RESULTS

3.4.1. MEASUREMENT RESULTS OF THE 1.6M FLAT

The first 22 terms and all rotational symmetric terms up to power 30 of the Zernike standard polynomials were used to represent the 1.6m flat. These polynomial terms were selected based on the knowledge of the mirror fabrication method. Also more polynomial terms were included to check the convergence of the data reduction results. The measurement result of the surface error of the 1.6m flat before it was put into a mounting cell was 6nm *rms* (power was not included), as shown in Fig.3.5 left. After it was put into the cell, the surface error increased to 21nm *rms* (Fig.3.5 middle). Most of errors were in forms of astigmatism caused by the changing of the supports. Removing the astigmatism terms numerically, the error of the surface went back to 6nm *rms* (Fig.3.5 right).

(a)   (b)   (c)
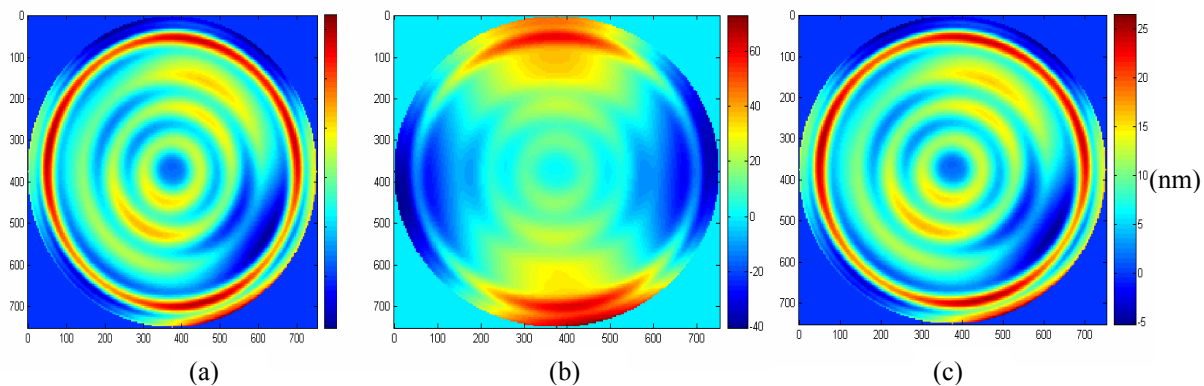
Figure 3.5 (a) measurement results of the 1.6m flat rms=6nm, before it was put into cell. (b) rms=21nm, after it was put into cell. (c) rms = 6nm, after it was put into cell and astigmatisms were removed.

Fig. 3.6 shows the final measurement result of the 1.6m flat, including 11nm power that was obtained from a pentaprism test (Yellowhair *et al*. 2007). The *rms* error was 24nm.
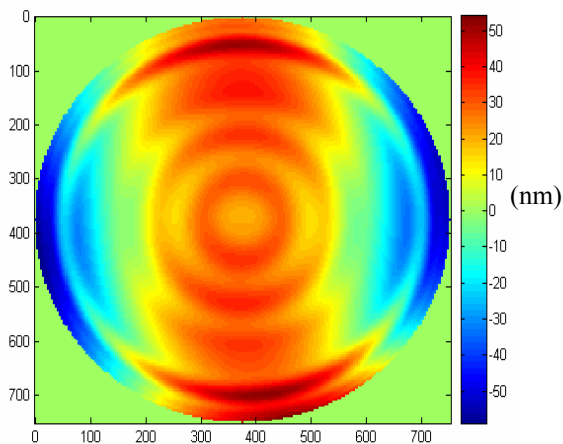
Figure 3.6 Final surface measurement result of the 1.6m flat including power, *rms*= 24nm

3.4.2. MEASUREMENT RESULTS OF THE REFERENCE FLAT

As the ML method realized an absolute test, it also gave the measurement result of the reference flat. The first 79 terms of Zernike standard polynomials were used to describe the surface errors of the reference flat. The *rms* error of the reference transmission flat was 42nm, as shown in Fig. 3.7. Trefoil was the dominant error in the reference flat as can be expected from the mounting structure used.
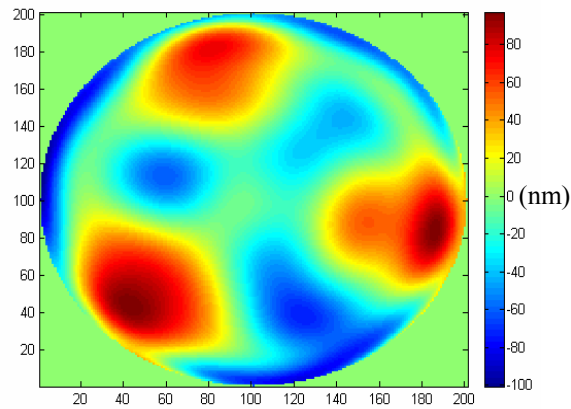
Figure 3.7 Surface measurement result of the reference flat *rms*= 42nm

Fig. 3.8 shows the two independent measurements of reference flat taken before and after the 1.6m flat was put into the cell. Their difference was 1.8nm *rms*. The 1.6m flat shape has been changed, while the reference flat measurement result stayed the same as expected. This proves that our measurement has very good repeatability and reliability.
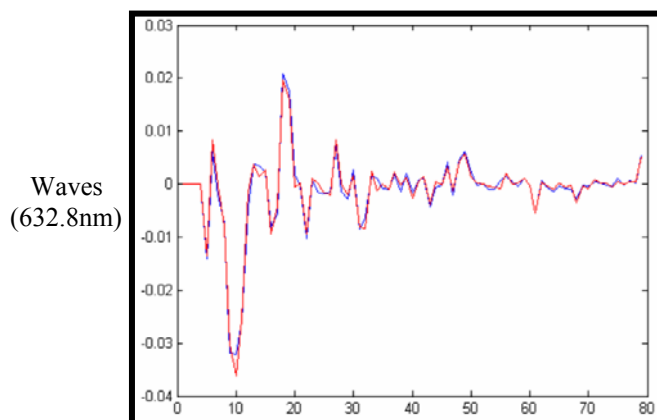
Figure 3.8 Zernike coefficients from two independent measurements of the reference flat (The difference was 1.8nm *rms*)

Measuring the reference flat has also been tried by using several different ways (Sprowl May 2006). These included the liquid flat test, Parks's method, and the *n*-rotation test. The liquid flat test was not very successful; the stability of the liquid flat in particular was a problem. Parks' method and the *n*-rotation test (six rotations), with their limitation of measuring only non-symmetric aberrations, gave quite similar results as shown in Fig. 3.9.
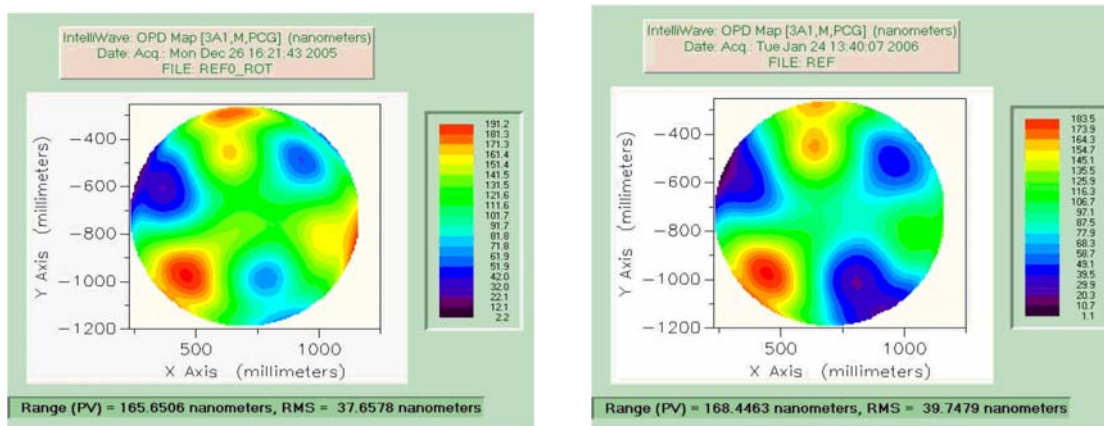
Figure 3.9 Measurement result of the Parks' method (left) was 37nm *rms*, measurement result of the 6 rotation method (right) was 39nm (Sprowl 2006).

3.5. ERROR ANALYSIS

A key advantage of ML method over other method is that it provides an estimate of the measurement uncertainty in addition to the estimate itself. The following will discuss the measurement errors contributed from various sources.

3.5.1. SURFACE DEFORMATION DURING THE MEASUREMENT

Changing the relative position of the reference and test surfaces can deform the surface figure to a different shape, if there is apparent change in the support or mounting. This will cause inconsistency between each sub-aperture measurement. For the 1.6m flat test, this effect was minimized due to the symmetry of the mounting and excellent mechanics.

3.5.2. ERROR DUE TO RANDOM NOISE

Errors contributed from random noise are estimated by the variance propagation model (Press *et al.* 2006). Equation 3.8 is solved in a least square sense. With the assumption of an identical independent Gaussian distribution of phase errors, the variance associated with the estimate coefficients x_i can be found from Equation 3.13 (William Press *et al.* 2006; Appendix A):

$$\sigma^2(x_i) = C_{kk}\, \sigma_y^2 ,$$

$$C = (M^T M)^{-1} , \qquad\qquad (3.13)$$

where C_{kk} is the diagonal elements of covariance matrix C. Given the phase standard

deviation σ_p from experiment data (from Equation 3.4, with the same arguments in Equation 3.10), the standard deviation of σ_y can be calculated as following:

$$\sigma^2(y_i)=CY_{jj}*\sigma_p^2,$$

$$\textbf{CY}=(\textbf{U}_i^T\textbf{U}_i)^{-1}, \qquad\qquad (3.14)$$

$$\sigma_y^2=\Sigma(\sigma^2(y_i))/N,$$

where N is the number of phase data. From Equations 3.13 and 3.14, the measurement uncertainties due to random noise in the phase measurements can be obtain. In Equation 3.14, $\textbf{U}_i$ is the orthogonal numerical basis generated by the SVD. $\textbf{U}_i$ is a unitary matrix, such that

$$CY_{jj}=1;\ \sigma^2(y_i)=\sigma_p^2=\sigma_y^2 \qquad\qquad (3.15)$$

Fig. 3.10 shows the numerically generated covariance matrix $\textbf{C}$ of the 1.6m flat test, including the alignment terms, which show in red color in the figure. Red means that the estimates of the alignment terms have relatively large uncertainties compared to the estimates of the surface coefficients. Along the main diagonal line of the matrix $\textbf{C}$, the first 30 terms of C_{kk} correspond to the coefficients of the 1.6m flat, and the rest of the 75 terms correspond to the coefficients of the reference flat. The sum of the first 30 terms is 0.0034. So the phase error of the 1.6m flat σ_a introduced by random noise is

$$\sigma_a= sqrt(0.0034)*\ \sigma_p =0.3nm, \qquad\qquad (3.16)$$

where σ_p, which is the repeatability of the interferometer we used, equals 5 nm from experiment measurement. The sum of the 75 reference terms is 0.0078, so the phase error of the reference surface σ_b introduced by random noise is

$$\sigma_b = sqrt(0.0078)*\ \sigma_p =0.4nm. \qquad\qquad (3.17)$$

The **C** matrix is also a function of the number of data. More sampling points and measurements will provide a smaller C_{kk} and a better signal to noise ratio.
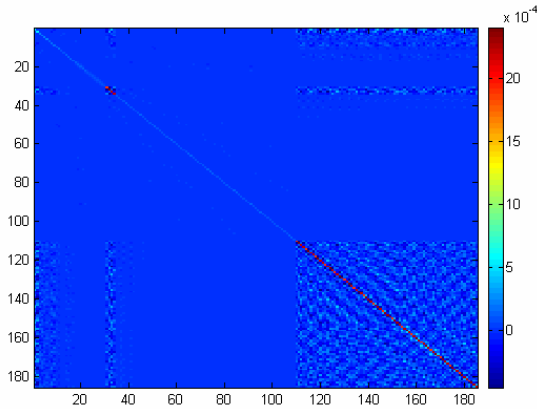
Figure 3.10 Numerically generated covariance matrix **C**

3.5.3. GEOMETRY MODEL ERRORS

Geometric model errors are the uncertainty in the rotation angles and the relative lateral position of the surfaces. Because these are essentially shearing errors, phase errors introduced are related to the derivatives of the surface error.

The angular derivatives of the Zernike polynomials show that with a rotation angle errors $\Delta\theta$, the introduced *rms* surface error of each Zernike polynomial terms is

$$rms=\Delta\theta*m*coefficient \qquad (3.18)$$

where m = is the angular frequency number of the Zernike polynomial.

For example, if the original surface has 40 nm astigmatism (Z5) with 0.1° angular errors, then the *rms* error of 0.0017*2*40=0.14 nm will be introduced to that sub-aperture measurement. Similarly, from the x and y derivative of the Zernike polynomials, the lateral displacement sensitivities can be obtained. Table 3.2 gives the x displacement

scale factors corresponding to several low order Zernike standard polynomial terms. In the 1.6m flat test, the centers of both surfaces were known better than 1.6mm. With 42nm surface error and 1m diameter of the reference flat, a scale factor 6 being used will give a *rms* error of 0.76 nm as shown in Equation 3.19.

$$rms = 1.6/500 *6*42 = 0.8nm \qquad (3.19)$$

With 6 nm surface error and 1.6m diameter of the test flat, a scale factor 6 being used will give a *rms* error of 0.07 nm as shown in Equation 3.20.

$$rms = 1.6/800 *6*6 = 0.07nm \qquad (3.20)$$

Table 3.2 x displacement scale factors of Zernike standard polynomial Z5-Z14

Z5	Z6	Z7	Z8	Z9	Z10	Z11	Z12	Z13	Z14
0	0	3.5	3.4	3.5	3.4	6.3	6.3	6.3	4.5

With the optimization routine introduced in the ML method (Su *et al*. 2006) and considering the magnitude of the *rms* error in the 1.6m flat, contributions from geometric errors in the 1.6m flat estimate can be ignored.

3.5.4. HIGH FRENQUNCY SURFACE RESIDUALS

In the ML method, because finite polynomial terms are used to describe the surfaces, the high frequency parts of the surface information σ_r are left as fitting residuals. Since the higher order polynomials terms are not included in final surface estimate result, σ_r will contribute a certain systematic error to the estimate. Moreover, there will be

crosstalk between the estimates of the lower order aberration terms and the high frequency residual, because these residuals that are buried in the phase data also join the estimation process. The crosstalk mechanism was checked by adding some higher order Zernike terms in the test surface or reference surface, while using fewer terms to describe the test and reference surfaces and the basis functions. For example, one wave of spherical aberration (Z11) was put in the test surface, but only the first ten Zernike polynomials were used to describe each surface and the basis functions. After data processing, reference surface showed 0.04 waves surface errors, while the test surface showed 1.0004 waves surface errors. Comparing the estimate results and the input data, 0.04 waves reference surface estimate error was obtained, while the estimate error of the test surface was 0.03 waves. Looking into the data reduction process, one can find that the crosstalk was due to the non-circular shape of the overlap region in the sub-aperture test. The surface error Z_{11} term shown in the overlap region was no longer orthogonal to the basis created from low order terms with the SVD method. Certain values were then coupled to the column vector y. When minimizing Equation 3.2, those values coupled into the estimate coefficients of the surfaces.

Crosstalk also increases as the number of terms used to describe each surface increased. A simulation result is shown in Fig 3.11. One wave of the Zernike standard polynomial term 80 was introduced to the test surface, the magnitude of the crosstalk error was plotted with respect to the number of terms used for representing the test surface.
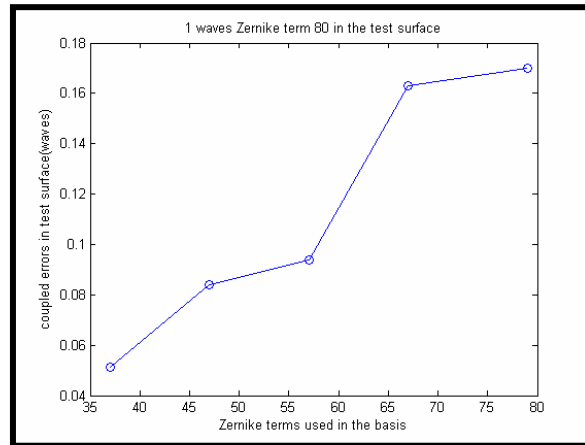
Figure 3.11 Crosstalk errors increase as more terms are involved

Fig. 3.12 shows the result of an investigation looking into how the crosstalk errors vary with the order of the residuals when the same numbers of basis terms, 79 terms, are used. For the 1.6m flat test, the crosstalk errors are less than 20%.
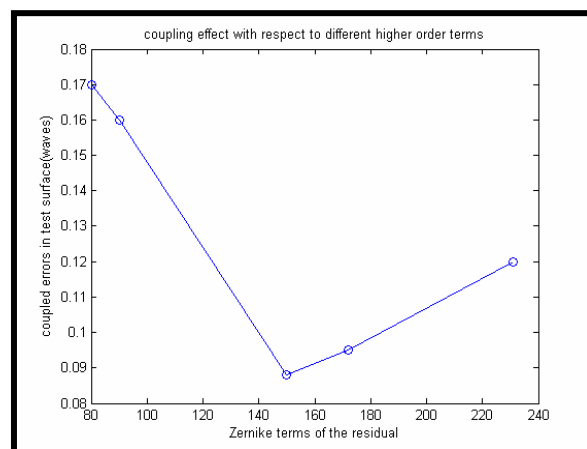
Figure 3.12 Crosstalk errors vary with the order of the residuals

Based on the analysis above, as discussed in Chapter 2, to reduce crosstalk errors,

basis functions need to be well selected so that they can efficiently represent the measurement data. More measurements and better sub-aperture geometry can also reduce the magnitudes of the off-diagonal elements of the *C* matrix, giving smaller crosstalk effects.
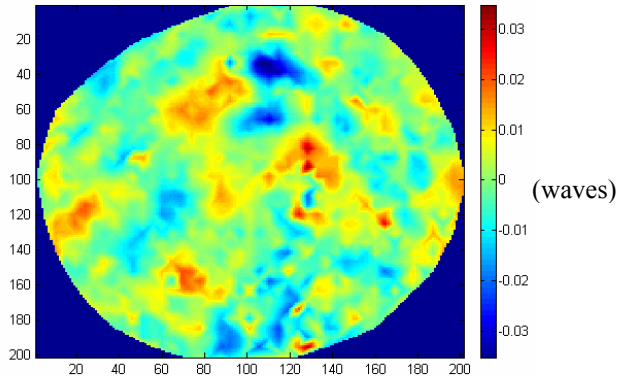
Figure 3.13 One of the sub-aperture L-S fitting residual maps

Fig. 3.13 shows one of the sub-aperture residual maps (system residuals) after the errors from the mirror and reference surface were removed, in which the *rms* error is ~5.5nm. System residuals can be decomposed as shown in Equation 3.21.

$$(\text{System residuals})^2 = (\text{random noise})^2 + (\text{fitting residual in } A)^2 + (\text{fitting residual in } B)^2$$

$$(3.21)$$

In Equation 3.21, system residuals are ~5.5nm, and random noise is ~5nm. Assuming fitting residuals from surface *A* and *B* are at same level, we get that σ_r is 1.6nm. So the magnitude of the system error σ_{sr} induced by the high frequency residuals to each surface is 1.6nm. Using the 20% rule from the high frequency residual coupling analysis above, the crosstalk error to the 1.6m flat σ_{rra} is:

$$\sigma_{rra} = 0.2 * \sigma_r = 0.32 \text{nm} \qquad (3.22)$$

The crosstalk error to the reference flat σ_{rrb} is

$$\sigma_{rrb} = 0.2* \sigma_r = 0.32nm \tag{3.23}$$

3.5.5. TOTAL MEASUREMENT ERRORS

Taking each error contribution as independent, the total measurement error of the flats can be calculated from the root sum square of the random noise error, residual induced systematic error and residual induced random error. The total measurement error of the 1.6m flat from the ML method is

$$rms = sqrt(\sigma_a^2 + \sigma_{rra}^2 + \sigma_{sr}^2) = 1.6nm \tag{3.24}$$

And the total measurement error of the reference flat is

$$rms = sqrt(\sigma_b^2 + \sigma_{rrb}^2 + \sigma_{sr}^2) = 1.6nm \tag{3.25}$$

3.6. COMPARISON BETWEEN ML METHOD AND COMMON STITCHING METHOD

The ML method estimates both the reference and the test surfaces, gives a global optimal for consistency. Common stitching method such as discrete phase method does not estimate the reference surface and is designed to optimize the consistency in the data overlap region. We compared the 1.6m flat measurement results between the ML method and MBSI (Zhao *et al.* 2006), which is a commercial stitching software.

Processing data from sub-aperture measurements with ML method gave the estimate result of the 1.6m flat in Zernike coefficients. The estimation also provided the

estimate of the reference surface. With the common stitching method, data from sub-aperture measurements were first reduced by removing the errors contributed from the reference surface which were obtained from ML estimate. Then the sub-aperture data were stitched together to give a full phase map of the 1.6m flat. Least squares fitting the stitched data gave the Zernike coefficients of the 1.6m flat. Fig. 3.14 shows the measured Zernike coefficients of the 1.6m flat from both the ML method and MBSI. The *rms* difference is 1.38nm. Fig. 3.15 shows the difference between the phase map from MBSI and the phase map generated from Zernike coefficients obtained from ML method. The *rms* error is 5nm. Compared with the coefficients difference above, 5nm here also included the errors from high order frequency residuals and random errors.
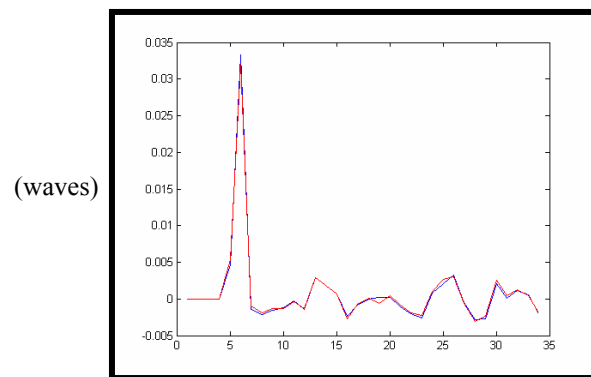
Figure 3.14 Estimated Zernike coefficients of 1.6m flat from ML method and MBSI
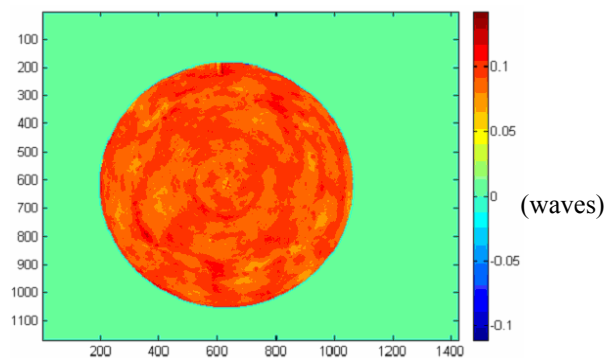
Figure 3.15 Difference map between MLE and MBSI

Numerical simulations were also performed to check the measuring ability of the ML method and the common stitching method. Given 20 waves random tilt and 0.1 waves Gaussian random noise, the estimate results from both methods turns out to be the same as shown in Fig. 3.16 and 3.17. Since both methods base on least squares fit during the calculations, the estimate results of them are equivalent given same level of noise.
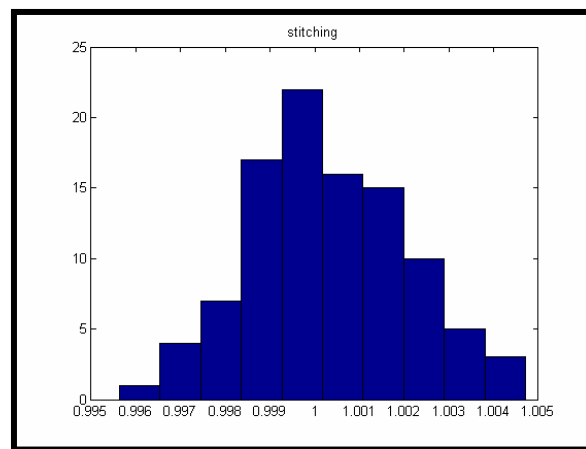
Figure 3.16 Estimate from sub-aperture stitching (mean= 1.0003; standard deviation= 0.0018)
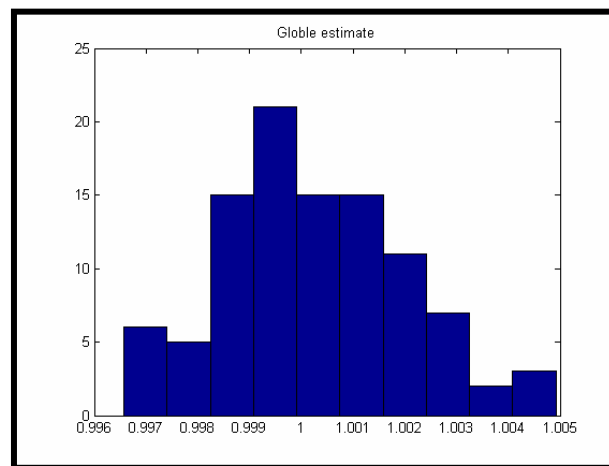
Figure 3.17 Estimate from ML method (mean= 1.0003; standard deviation= 0.0018)

3.7. SUMMARY

In Chapter 3, the work performed for the absolute measurement of a 1.6m flat mirror with the ML method was summarized. The basic principle of the ML method for the large flat test, the experiment setup, the measurement results and the error analysis are described. The flat mirror was measured with an accuracy up to 2nm. The accuracy is limited by the residual errors of the surfaces.

CHAPTER 4

SHEAR TEST OF AN OFF-AXIS PARABOLIC MIRROR

4.1. INTRODUCTION

The symmetry of a mirror segment with respect to rotation about its parent optical axis can be exploited to verify the accuracy when the mirror is under optical testing. A perfect off-axis segment can be rotated about its parent axis, and the apparent shape of the mirror will not change. This geometry is shown in Fig 4.1. The interferometer views the mirror in fixed coordinates that do not rotate with the segment, so any changes in an imperfect mirror shape would be due to figure errors that are not symmetric about the parent axis of symmetry. This change is independent of errors in the test system. This technique is a variation of a common method that is used for axially symmetric surfaces (Parks 1978).
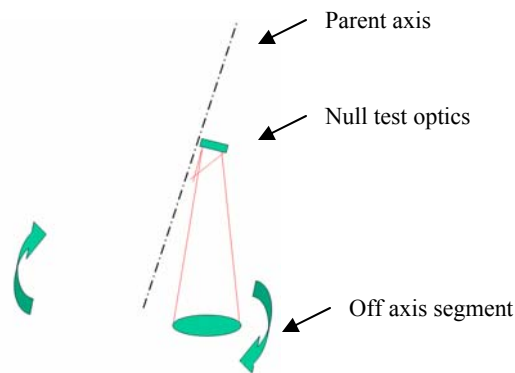
Figure 4.1 The concept of the shear-test for an off-axis segment

A shear-test to verify for verifying the main test for the New Solar Telescope (NST) primary mirror, which is an off-axis parabola, is discussed here. The shear in this test is realized by rotating the mirror around its parent axis while the null test optics is unchanged. The data of the test are the interferograms taken at different shearing positions. This shear-test allows the errors that move with the mirror to be separated from the errors that stay in the null test optics. The maximum likelihood (ML) method and singular value decomposition (SVD) (Press *et al*. 1986) are used to perform a least-squares-estimate of both the mirror and the null optics. The setting of the estimate threshold is based on the Wiener filter concept (Press *et al*. 1986), and the null space of this test is systematically determined from numerical analysis. The outputs of the shearing test are separated into four parts: errors in the test surface, errors in the null test optics, terms in the null space (that could come from either the mirror or the null test), and noise in the measurements.

4.2. THE NST MIRROR AND ITS MAIN TEST

4.2.1. NST PRIMARY MIRROR AND ITS FABRICATION

The NST primary mirror (Martin *et al*. 2004 and 2006) is a 1.7m diameter off-axis parabola. It has a radius curvature of 7.7m, an off-axis distance 1.84m and a maximum p-v aspheric departure 2.7mm. This mirror is a 1/5 scale for the GMT segments. The NST mirror will be supported actively by 36 actuators in the telescope. For polishing and measurement in the lab, the actuators are replaced by passive hydraulic cylinders whose

forces match the operational support forces for zenith-pointing. The aspheric surface of the NST mirror was generated to an accuracy of about 15μm *rms* by ITT Industries. Loose-abrasive grinding and polishing were performed by the Steward Observatory Mirror Lab (SOML). A stressed lap was used for loose-abrasive grinding of the mirror to remove subsurface damage and improve the figure accuracy to about 1μm *rms*. During this phase, the surface was measured with a laser tracker. After that, the surface was polished and figured with the stressed lap and small passive tools. An interferometric principal test was used for measuring the surface.
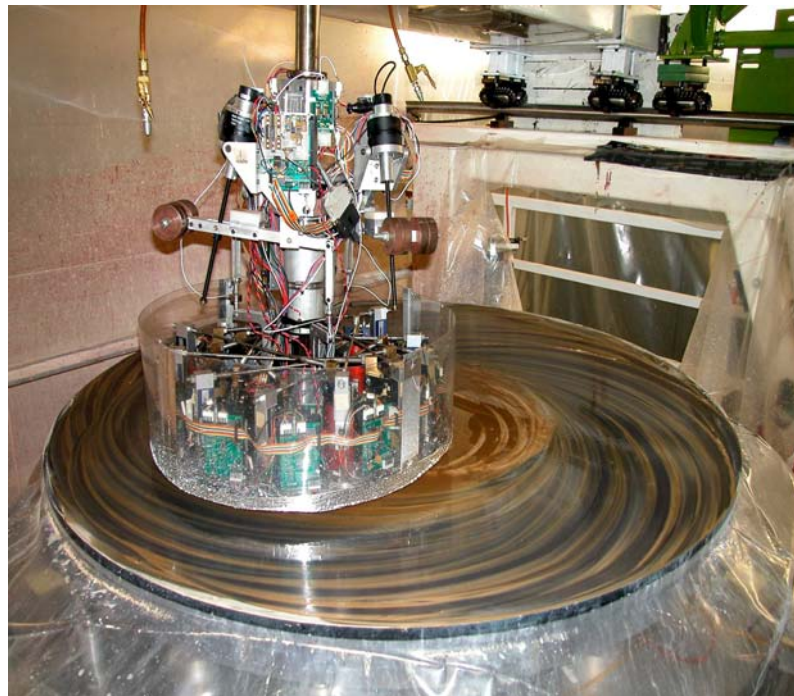
Figure 4.2 NST mirror in polishing by 30cm stress lap

4.2.2. THE MAIN OPTICAL TEST FOR THE NST MIRRROR
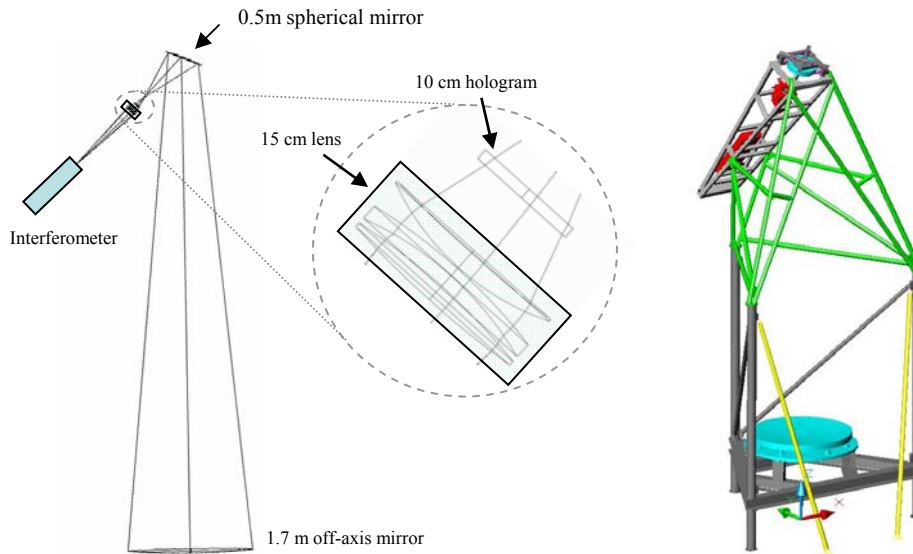
Figure 4.3 The main optical test system for the NST mirror

The main test for the NST mirror is a full-aperture interferometric test that uses a hybrid reflective-diffractive null corrector to compensate for the mirror's aspheric departure. The test system is shown in Fig. 4.3. Most of the compensation is accomplished by an oblique reflection off a 0.5m diameter spherical mirror, and the rest is done by a computer-generated hologram (CGH). This test is a prototype for the main optical test of the GMT segment; although the GMT test requires two spherical mirrors (3.8m and 0.75m diameter) to compensate for the 14 mm aspheric departure. The alignment of the NST null test system is very challenging. From the tolerance analysis, many parameters need alignment to 10um levels (Zehnder *et al*. 2006).

4.2.2. ASPHERIC WAVEFRONT CERTIFIERS

A spherical wavefront can easily be generated by its nature, so the spherical surface is easily fabricated and has been widely used in optical systems. The beauty of aspheric surfaces is that they can dramatically reduce system element numbers as well as reduce system size and complexity. However, an aspheric wavefront is hard to generate and verify which leads to the difficulty in fabricating aspheric surfaces. Null tests, CGH, and the combination of them have been the main metrology methods for testing aspheric optics (Burge 1993; Zhao *et al*. 2005). To generate a correct aspheric wavefront, a null optical system usually sets a tight tolerance for the alignment of the system and the element quality. To verify the aspheric wavefront, a certifier, such as another CGH (Burge *et al*. 1993) or a diamond turned mirror (Palusinski *et al*. 2004), may be used.

The role of a certifier is to simulate the optical property of the surface under test. When an aspheric wavefront generated from a null system meets the certifier and is reflected back, the rays follow the same path as if it were to reflect from the surface under test. So the certifier can be used to verify the null system. The advantage of the certifier is that it has a much smaller size and can been fabricated quite accurately with other techniques. However, as the surface under test becomes larger, the certifier also needs to become large to avoid a caustic region, in which rays overlay each other, creating ambiguity (Su *et al*. 2005). This sometimes makes the certifier solution impossible. The GMT off-axis segment is an example where a practical certifier solution is not available. So to verify a null test system, other types of verification tests need to be considered

(Burge *et al*. 2006). The shear test discussed in this chapter is one of the verification tests planned for the GMT main test.

4.3. THE PRINCIPLE FOR THE NST SHEAR-TEST
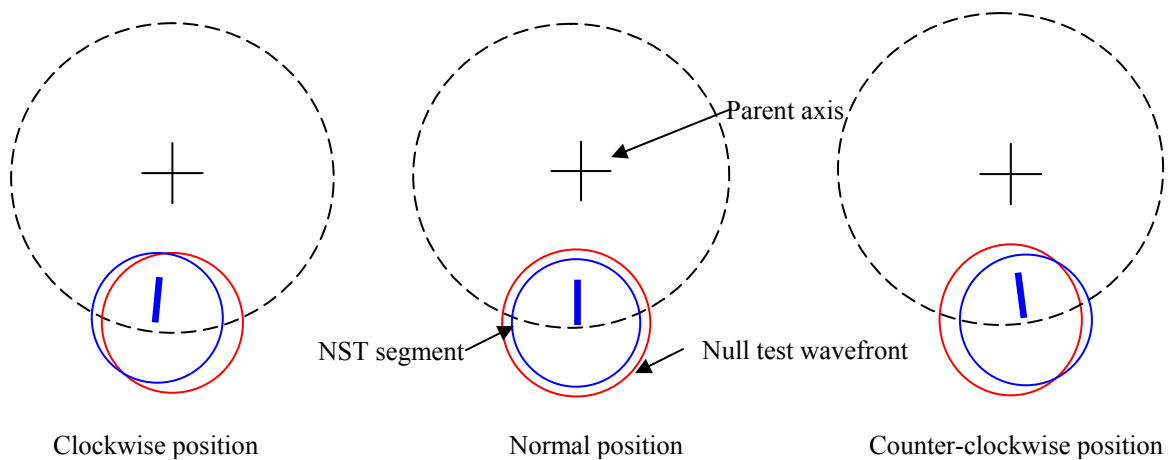
Figure 4.4 The principle of the shear-test

The principle of the NST shear-test is shown in Fig. 4.4. The mirror is rotated clockwise and counter-clockwise about its parent axis by approximately 3º, and three sets of interferograms were taken at each position. The maximum likelihood (ML) method is then used to reduce the interferometric data.

4.3.1. BASIC PRINCIPLE

The null optics wavefront (*A*) and the NST mirror (*B*) are represented by Zernike polynomials. Data from the three set of measurements can then be expanded as:

$$D_{ij} = D_{ij}{}^a + residuals$$

$$= P_i Z_1(x_{bi}, y_{bi}) + Tx_i Z_2(x_{bi}, y_{bi}) + Ty_i Z_3(x_{bi}, y_{bi}) + De_i Z_4(x_{bi}, y_{bi}) +$$

$$alignment \quad aberrations - \sum_{p=5}^{m} A_p Z_p(x_a, y_a) + \sum_{p=5}^{n} B_p Z_p(x_{bi}, y_{bi}) + residuals$$

$$(4.1)$$

Where i =index of the measurement

D_{ij} = the *j*th phase data in *i*th measurement

$D_{ij}{}^a$ = the phase data which can be described using polynomials

x_a, y_a = coordinates of the null optics wavefront

x_{bi}, y_{bi} =Global coordinates of the mirror in *i*th measurement

Z_p =Zernike polynomials

$P_i Z_1(x_{bi}, y_{bi})$ = piston

$Tx_i Z_2(x_{bi}, y_{bi})$ = tilt x

$Ty_i Z_3(x_{bi}, y_{bi})$ = tilt y

$De_i Z_4(x_{bi}, y_{bi})$ =defocus

alignment aberrations   =combination of coma and astigmatism induced by mirror

misalignment

4.3.1.1. ALIGNMENT ABERRATION
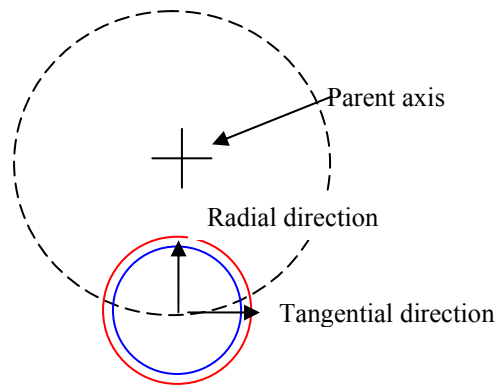
Figure 4.5 Tangential and radial direction of the misalignment

Alignment aberrations arise from mirror misalignment, which is the special property of an off-axis parabola. When the parabolic mirror is misaligned relative to the null optics wavefront by shifting along the tangential direction as shown in Fig.4.5, sine astigmatism and cosine coma as described in equation 4.2 will be generated in the interferogram.

$$alignment \quad aberration = S_1 * (-17.3 * \sqrt{6} * \rho^2 \sin(2\theta) + 2.2 * \sqrt{8} * (3\rho^3 - 2\rho)\cos(\theta))$$

(4.2)

where S_1 = a scale factor related to the magnitude of the tangential shift

ρ, θ = polar coordinates of the mirror

$\rho^2 \sin(2\theta)$ =Zernike sine astigmatism

$(3\rho^3 - 2\rho)\cos(\theta)$ =Zernike cosine coma

Similarly, when there is a radial misalignment, cosine astigmatism and sine coma will be generated as follows:

$$alignment \quad aberration = S_2 * (-477 * \sqrt{6} * \rho^2 \cos(2\theta) - 43 * \sqrt{8} * (3\rho^3 - 2\rho)\sin(\theta))$$

$$(4.3)$$

where S_2 = a scale coefficient related to the magnitude of the radial shift

        $\rho^2 \cos(2\theta)$ = Zernike cosine astigmatism

   $(3\rho^3 - 2\rho)\sin(\theta)$ = Zernike sine coma

With Equation 4.1, simultaneous equations can be obtained from the three set of interferometric measurement. However, alignment aberrations are not linearly independent from astigmatism and coma in the surfaces. To be able to measure the astigmatism and coma in the mirror or the null optics, during the data reduction process, the alignment aberrations in the measurement from the normal position are numerically removed in a least squares sense to minimize the *rms* wavefront error. It has the same effect as when we align the mirror to the null optics to minimize the wavefront error. The astigmatism and coma left in the measurement after minimizing are assumed to be in the mirror or in the null optics (Caution is needed here. The shifts for minimizing the rms wavefront error must be within the tolerances of the off-axis distance and the clocking

angle of the mirror.). After that, when solving the simultaneous equations in a least squares sense, the astigmatism and coma in the surfaces are solved to maintain consistency in the three measurements, and the coefficients of the alignment aberrations in the other two measurements are automatically determined to minimize the total residuals.

4.3.1.2. COORDINATE RELATIONSHIPS

Data from the interferometric measurements are the phase differences at certain positions of the mirror and the null optics wavefront. For phase data in a single measurement, the coordinates x_a, y_a (coordinates of the null optics wavefront which stayed unchanged in the three measurements) can be found from the measurement in the normal position by knowing the pixel corresponding to the center of the wavefront and pixels representing the edge of the wavefront. Normalized coordinates can then be determined, with the edge of the wavefront normalized to one.

Similarly a normalized coordinate for the mirror at its normal position can be defined. When the mirror is rotated, x_{bi}, y_{bi} can be obtained by finding which position on the mirror in its normal position is associated with each pixel in a rotated phase map. Knowing the rotation angle of the shear, this relationship can be described by x, y translation and a pure rotation around the mirror center.

With phase data and coordinate information, simultaneous equations created from equation 4.1 are then ready to be solved.

4.3.1.3. MATRIX FORM

As in Chapter 3, the shear test can be described by the matrix Equation 4.4

$$y=M \cdot x, \qquad\qquad (4.4)$$

where x = the solution vector, including the coefficients of the mirror and null

optics wavefront and the alignments

y = the data vector, phase data from the three measurements, have been

compressed by basis functions

M = the system matrix, determined by test geometry

The solution vector x is solved with the SVD method to get a good estimate of the result

under the presence of noise.

4.3.2. NULL SPACE OF THE SHEAR TEST

By intuition, we know that certain kinds of errors cannot be separated between the

test surface and the null optics from the shear motion performed. For instance, these

errors include errors with rotational symmetry around the parent axis, errors with

periodicity that repeat with shear angle, and shape error terms related to the alignment

errors (piston, tilts, power, and alignment aberrations). These errors constitute the null

space of the shear test. As they are the inherent properties of the test, they can be

numerically derived from the system matrix M.

To determine the null space, the SVD method is used to decompose the system

matrix M. SVD can be thought to be a generalized spectrum analysis of the rectangular

matrix (Press *et al*. 1986). M can be uniquely decomposed as

$$M = USV',$$ (4.5)

where   *U*   = a unit matrix describing the range of the shear test,

          S   = singular value matrix; its diagonal components are the singular,

             values of the matrix *M*, which reflect the noise sensitivity of the surface

             error modes,

          V   = a unitary matrix describing the domain or the solution space of the test.

             The columns in *V* which correspond to zero singular values are the null

             space of the matrix *M*.

4.3.2.1. DETERMINING NULL SPACE

Errors in the null space cannot be separated between the null optics (*A*) and the NST mirror (*B*), so the solution vectors formed by their combinations satisfy the requirement for the null space of the system matrix ($M{\cdot}x$=0). In the same way, the null space vectors calculated from SVD ($M{\cdot}x$=0) imply that certain errors in *A* will cancel certain errors in *B*, and no signal will be generated. So these vectors are the null space of the test. In all, *the null space of the matrix is the null space of the test.*

Based on the above argument, the null space of the test can be obtained directly from the matrix *M*. It is the null space of the matrix *M*, which can be calculated with the SVD method. Fig. 4.6 shows an example of the calculated null space. Thirty-seven Zernike terms are used to represent surface *A* and *B*. The alignment error is not considered here. Errors in the null space are rotationally symmetric errors as shown in

Fig. 4.6. Fig. 4.7 shows the null space of the test in which 231 Zernike polynomials are used to describe surfaces and alignment terms are included during the calculation.
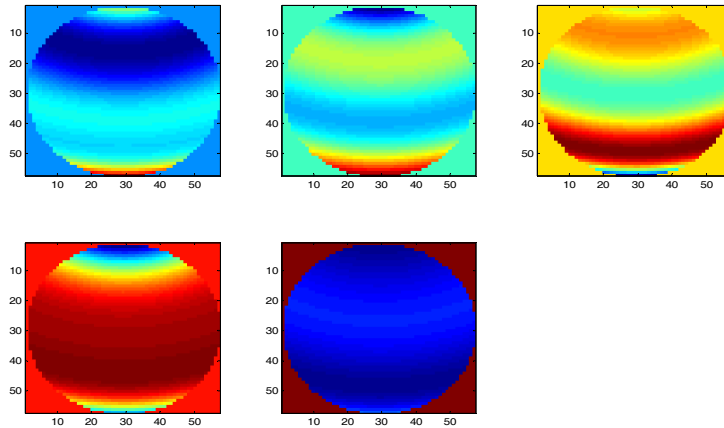
Figure 4.6 Null space without considering alignment terms
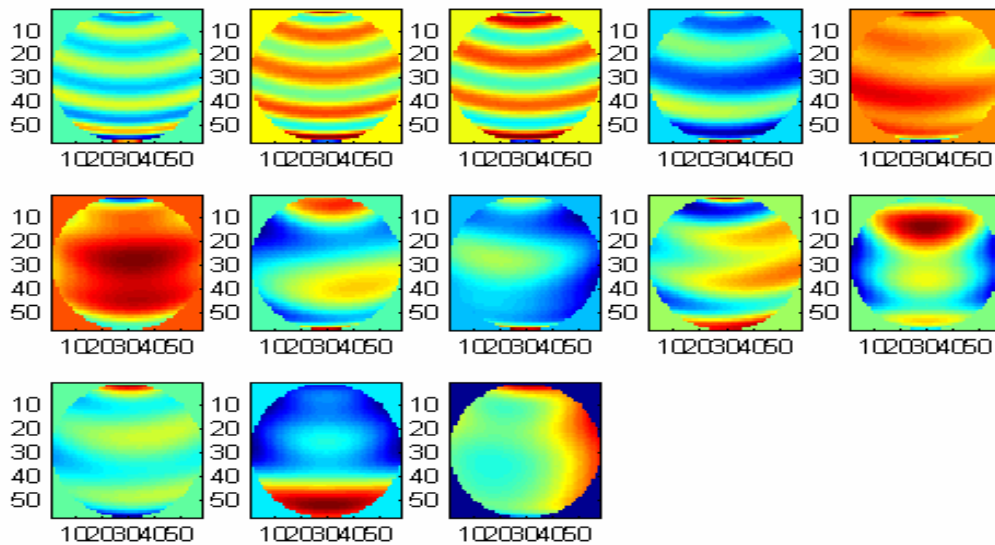
Figure 4.7 Null space generated with 231 terms Zernike polynomials. Measurement ambiguities from alignment are included.

4.3.2.2. REMOVE ERRORS IN THE NULL SPACE FROM SURFACE ESTIMATES

Errors in the null space are not separable between test surface and null optics. When the ML is performed to estimate the surfaces, these errors fall into the estimates of the two surfaces based on the minimal norm criteria. So the estimated results need to be further processed to remove the null space errors out of the surface estimates. This can be realized by least squares fitting the surface estimate results with null space vectors generated from the SVD and then removing the fitting result from the surface estimates.

The following is an example of removing the null space. A 100nm *rms* coma, as shown in Fig. 4.8 (a), was used as an input of surface *A,* and no error was put into surface *B*. Then three simulated measurement data were generated, and simultaneous equations were solved by SVD to give least squares estimates of *A* and *B*. After removing the null space, 71nm of the surface information was left as shown in Fig. 4.8 (b), which can be estimated accurately without noise. This would have been the measurement if we would have had 100nm *rms* of coma in surface *A*. In Fig. 4.8 (c), the blue line represents the input Zernike coefficients in surface *A* and *B*, while the red lines are the estimated results before the null space is removed. As we can see, the estimated results are polluted by the null space errors. Fig. 4.8 (d) shows that after removing the null space errors, there is no error left in surface *B*, and in surface *A,* the estimated results (the red curve, on top of the blue curve) has the exact same values as the expected data (the blue curve) calculated by removing the null space from the original input. Fig. 4.8 shows that the surfaces can be estimated accurately after the null space is removed.

(a)

(b)

(c)

(d)
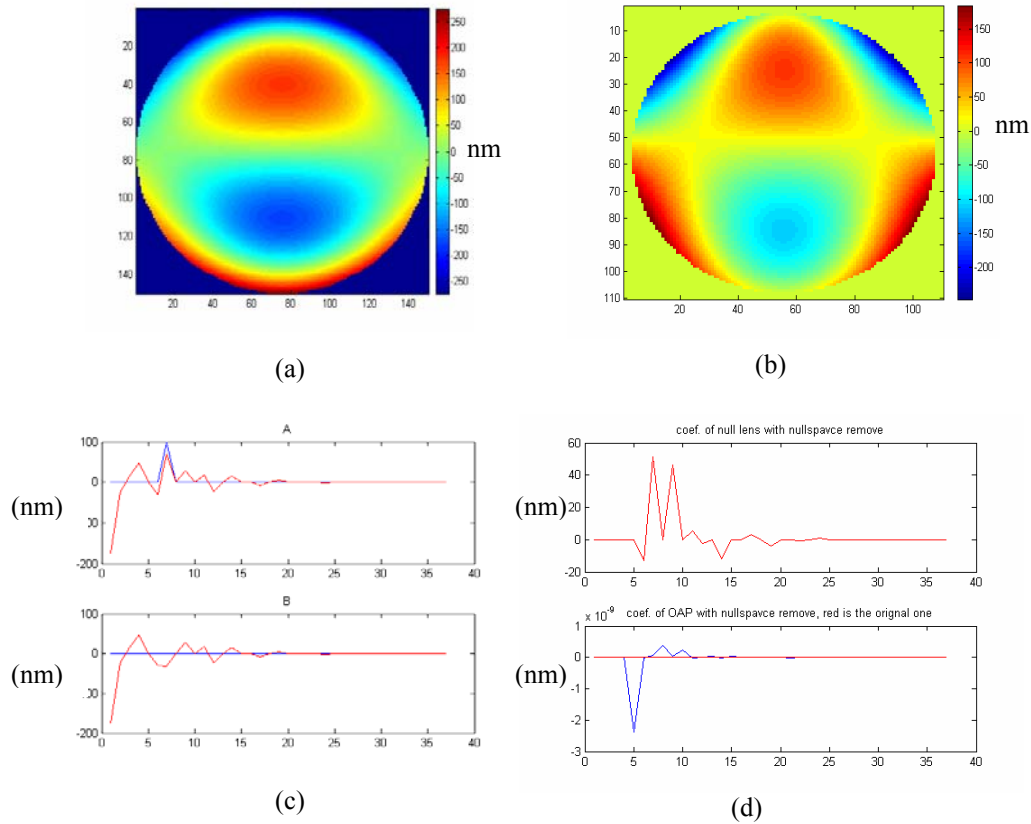
Figure 4.8 Removing null space errors from surface estimates. (a) 100nm *rms* coma in surface A, (b) estimate of the surface A, *rms*= 71nm when null space is removed, (c) Blues are the input Zernike coefficients of the surface A and B, total 37 Zernike terms are used; Red are the estimated results before null space is removed, (d) After null space is removed, input Zernike coefficients (blue) match the estimated coefficients (red).

4.3.3. SOLUTION SPACE AND NOISE SENSITIVITY

Using SVD, the estimate of the solution vector x can be expressed as (Press *et al.* 1986):

$$x = \sum_{i=1}^{n} \frac{yU_i{}'}{\omega_i} V_i \; , \tag{4.6}$$

where y = the data vector

       U_i = the ith column of matrix U

ω_i = the ith singular value in matrix $\boldsymbol{S}$

V_i = the ith column of matrix V.

V_i can be thought of as a certain combination of errors in surfaces A and B. This combination is a certain mode to be estimated. Errors in A and B can be decomposed as the combinations of columns in V. The singular value ω_i tells how many units of signal U_i will be generated with one unit of a mode in V. The larger the singular value of a certain mode, the bigger the signal generated during the shear test, and the better the insensitivity to noise. Thus, the above equation means that the phase data is first projected to the range vectors U, and then divided by the singular value. The result will be the magnitude of a certain mode in the surfaces. The estimate is a combination of different modes. Robustness of the modes is determined by the signal magnitude generated by one unit of the mode, which is the corresponding singular value of that mode. Rather than stating that a certain term in A or B is insensitive to the noise, it should be stated that a certain combination of the errors can be well estimated.

4.3.4. ESTIMATE THRESHOLD

A mode V_i with a small singular value will amplify the noise greatly because the mode is being divided by a small value as shown in equation 4.6. This makes the estimates of the surface coefficients become extreme large. A simple way to reduce this noise amplifying effect is by discarding the modes with singular values less than a certain threshold during the summation calculation in equation 4.6. To further make use of the

property of the noise in the test (normally Gaussian noise), a set of factors ϕ_i used to multiply each mode V_i to give a best least squares estimate of the surfaces under the existence of noise was derived based on the concept of Wiener filter (Press *et al*. 1986).

$$x = \sum_{i=1}^{n} \frac{y.U_i'}{\omega_i} V_i \cdot \phi_i \qquad (4.7)$$

$$\phi_i = \frac{yU_i'yV_i'}{yU_i'yV_i'+NU_i'NV_i'} \qquad (4.8)$$

where N = an estimate of the phase noise vector

ϕ_i can be calculated from equation 4.8. For extreme situations, equation 4.8 shows that when signals are dominant, the factor ϕ_i tends toward one, and when the noise is dominant, ϕ_i approaches zero.

4.3.5. SURFACE ERROR ESTIMATEABILITY AND NOISE SENSITIVITY

To simplify the procedure without losing the significance, zero and one are used as the values for the above factors ϕ_i. A threshold is selected to discard the modes when singular values are smaller than the threshold. Table 4.1 gives the Monte Carlo simulation results of the ability to estimate surface errors in the forms of Zernike polynomial 5-16. For example, as shown in the table, surface *A* and *B* each have 10nm surface errors of Zernike polynomial term 11. When the threshold is zero, after removal of null space errors, there is 9.1nm surface information remaining in both surfaces. When the threshold is set to 10, based on the noise level, part of the surface information is lost and only 8.9nm information is left. There are also 0.9nm estimate errors fall into the

surface estimates. From the data in Table 4.1, it can be concluded that lower order aberrations such as astigmatism, coma, and trefoil could not be fully estimated. However, the shear test is very good at detecting higher order aberrations.

Table 4.1 Ability to estimate Zernike terms 5-16

Zernike terms (A=10 nm B=10 nm)	Z5 (Sine astigmatism) (nm)	Z6 (Cosine astigmatism) (nm)	Z7 (Sine coma) (nm)	Z8 (Cosine coma) (nm)
Estimate with threshold =0	rmsa =10 rmsb= 10 rmserrora =0 rmserrorb=0	rmsa = 1.8 rmsb= 1.8 rmserrora =0 rmserrorb=0	rmsa = 7.1 rmsb= 7.1 rmserrora =0 rmserrorb=0	rmsa =10 rmsb =10 rmserrora=0 rmserrorb=0
Estimate with threshold =10	rmsa = 0.9 rmsb = 0.9 rmserrora = 9.1 rmserrorb = 9.1	rmsa = 1.8 rmsb = 1.8 rmserrora = 1 rmserrorb= 1	rmsa = 7.1 rmsb = 7.1 rmserrora= 0.3 rmserrorb= 0.3	rmsa = 6.9 rmsb = 6.9 rmserrora=3.2 rmserrorb=3.2
Zernike terms (A=10 nm B=10 nm)	Z9 (Sine trefoil) (nm)	Z10 (Cosine trefoil) (nm)	Z11 (Spherical aberration) (nm)	Z12 (nm)
Estimate with threshold =0	rmsa =7 rmsb= 7 rmserrora =0 rmserrorb=0	rmsa =10 rmsb= 10 rmserrora =0 rmserrorb=0	rmsa =9.1 rmsb= 9.1 rmserrora=0 rmserrorb=0	rmsa =8 rmsb= 8 rmserrora =0 rmserrorb=0
Estimate with threshold =10	rmsa = 7 rmsb= 7 rmserrora =0.2 rmserrorb=0.2	rmsa = 5.7 rmsb = 5.7 rmserrora=4.5 rmserrorb=4.5	rmsa = 8.9 rmsb = 8.9 rmserrora=0.9 rmserrorb=0.9	rmsa = 7.8 rmsb = 7.8 rmserrora=1 rmserrorb=1
Zernike terms (A=10 nm B=10 nm)	Z13 (nm)	Z14 (nm)	Z15 (nm)	Z16 (nm)
Estimate with threshold =0	rmsa = 10 rmsb= 10 rmserrora =0 rmserrorb=0	rmsa = 7.7 rmsb= 7.7 rmserrora =0 rmserrorb=0	rmsa = 10 rmsb= 10 rmserrora =0 rmserrorb=0	rmsa = 10 rmsb= 10 rmserrora =0 rmserrorb=0

Estimate with threshold =10	rmsa =9.9	rmsa =7.7	rmsa =9.7	rmsa =10
	rmsb = 9.9	rmsb = 7.7	rmsb=9.7	rmsb =10
	rmserrora = 0.6	rmserrora =0.5	rmserrora= 1.2	rmserrora = 0
	rmserrorb = 0.6	rmserrorb =0.5	rmserrorb=1.2	rmserrorb =0

In table 4.1, *rmsa* and *rmsb* are the *rms* values of the surface *A* and *B*, *rmserrora* and *rmserrorb* are the estimated errors of rmsa and rmsb.

4.4. EXPERIMENTAL RESULTS

A shear test was performed to measure the NST mirror. The mirror was rotated clockwise and counter-clockwise by approximately 3 degrees around its parent axis. Three sets of interferograms were taken. Because there was relatively large uncertainty in measuring low order aberrations, the data was first reduced to investigate higher-order aberrations only. After that, the data was analyzed again, considering the lower-order aberrations.

4.4.1. SURFACE ESTIMATES WITH LOWER-ORDER ABERRATIONS REMOVED

Lower order aberrations of piston, tilt, power, coma and astigmatism were removed from the input data. The data is shown in Fig.4.9. After removing lower order aberrations, the repeatability of the interferometric measurement was ~10nm. By mechanical control and geometric measurement, we knew the mirror position to ~1mm.

Mirror edge

Clockwise position   Normal position   Counter-clockwise position
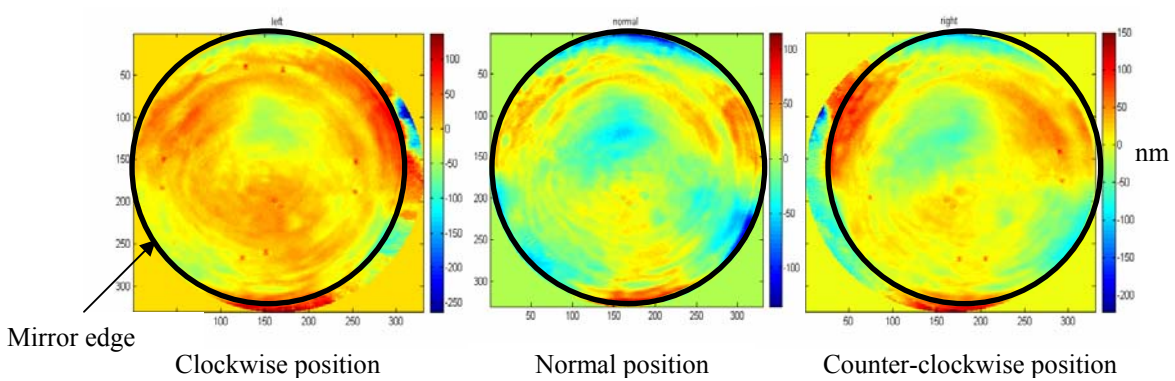
Figure 4.9 Interferograms of the NST shear test

A total of 231 terms of Zernike polynomials were used to represent each surface (*A* and *B*) in the ML method. Estimated results are shown in Fig. 4.10. The estimate of the mirror was 21nm *rms* (left), while the estimate of the null optics was 15nm (middle), and there are also 13nm *rms* errors in the null space (right).
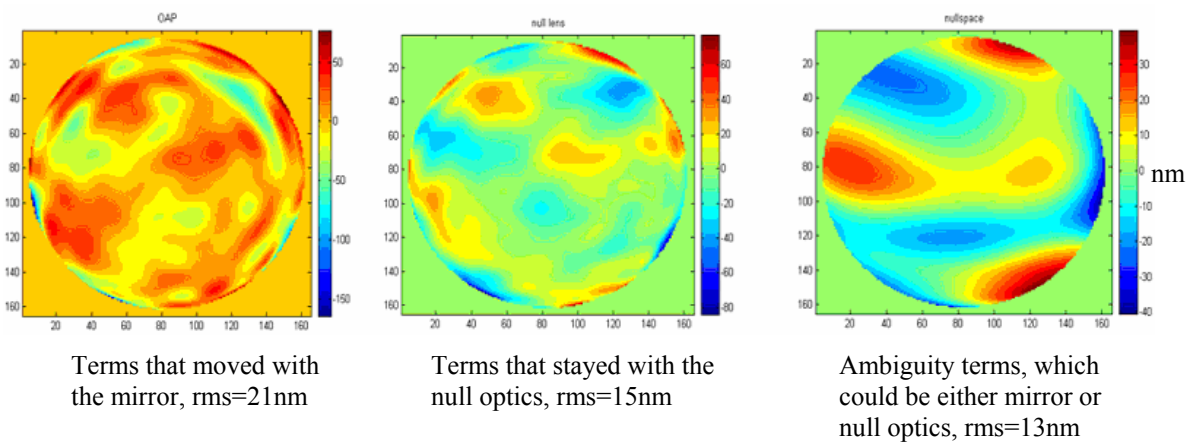
Terms that moved with   Terms that stayed with the   Ambiguity terms, which
the mirror, rms=21nm   null optics, rms=15nm   could be either mirror or
                                                                  null optics, rms=13nm

Figure 4.10 Estimate results of the NST shear test (lower order aberrations removed)

Subtracting the estimated errors of the null optics from the phase data of the normal position, we estimated that the mirror errors rose from 24nm to 28 nm. Here Zernike terms 1-13 were removed from the data due to the noise issue.
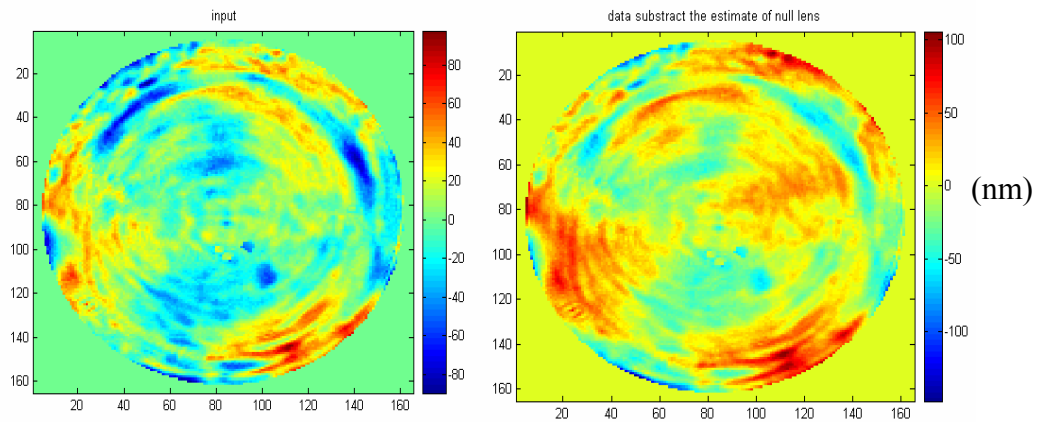
Figure 4.11 Single measurement rms=24nm and result after correcting null optics error rms= 28nm

With 231 terms of Zernike polynomials, we could not fully describe the input data. When the input data was fitted by basis functions, there were ~11nm of higher order residuals left in each interferogram as shown in Fig. 4.12.

Clockwise position   Normal position   Counter-clockwise position
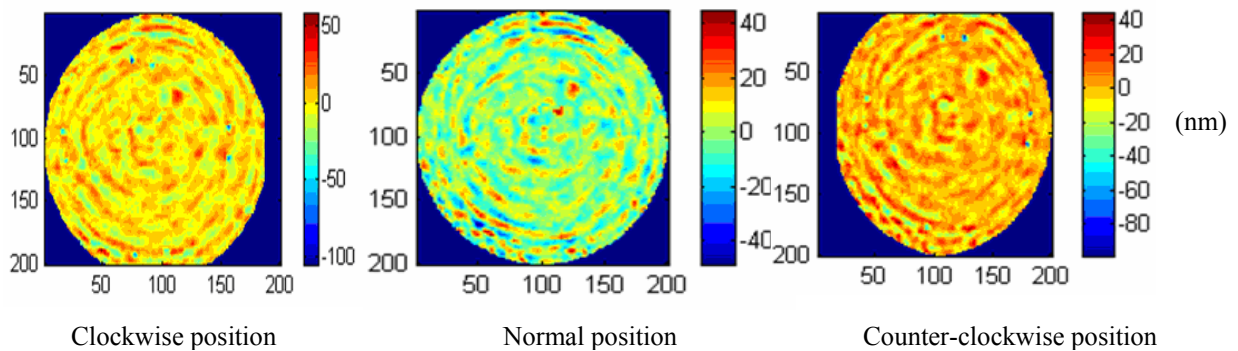
Figure 4.12 Basis error of the NST shear test, rms=~11nm

There were also ~6 nm analysis residuals as shown in Fig. 4.13, which were the residuals from least squares fit when the simultaneous equations were solved. They reflected the consistency between the ML model and the measurement data, and also the consistency between the three sets of the data.

Clockwise position   Normal position   Counter-clockwise position
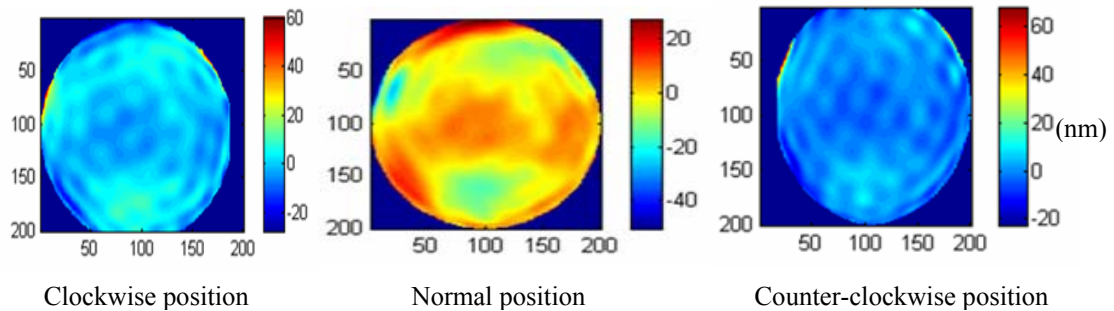
Figure 4.13 Analysis error of the NST shear test, rms=~6nm

4.4.2. SURFACE ESTIMATES CONSIDERING LOWER-ORDER ABERRATIONS

Mirror
edge   rms=98nm   rms=134nm   rms=130nm

Clockwise position   Normal position   Counter-clockwise position
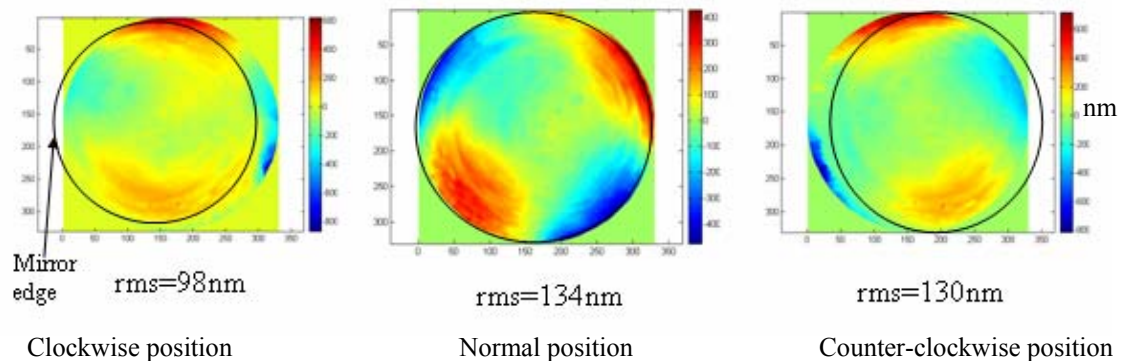
Figure 4.14 Interferograms of the NST test with lower-order aberration included

The three sets of data containing lower-order aberrations shown in Fig.4.14 were used as input to the ML method. Fig. 4.15 shows the estimated results. Comparing this with the coma shown to be zero in normal position after removing the alignment errors,

the shear test result suggests that there is a quite large amount of coma in the null optics and the mirror. This is consistent with the penta-prism test measurement result (Chapter 5). It also means there is a misalignment in the principal test. However, because we had relatively large measurement uncertainties in the lower order aberrations, there were about 20-30 nm analysis residuals left, which reflected the inconsistency between the measurement data, as shown in Fig. 4.16. This could be the real surface shape changing due to the change of the support between the measurements.
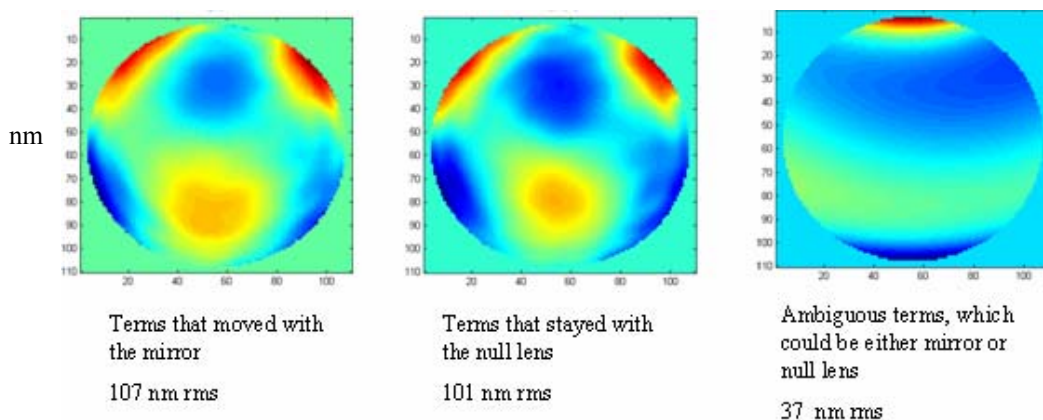
Figure 4.15 Estimate results (low aberration orders included)
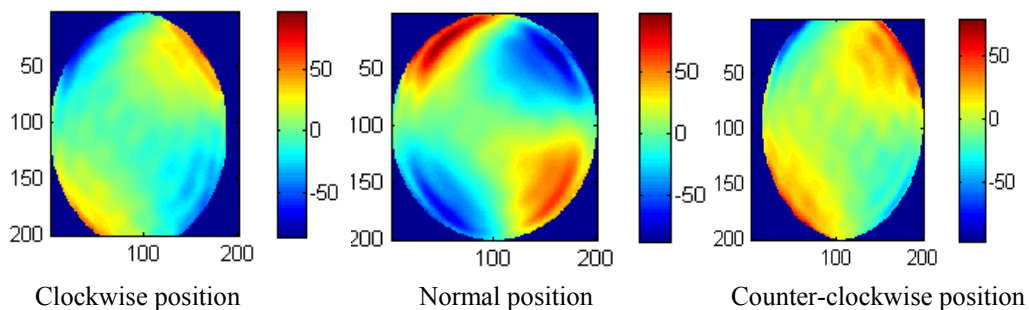
Figure 4.16 Analysis residuals rms=33, 20, 18 nm

4.5. DISCUSSION

4.5.1. MEASUREMENT ACCURACY

From the result of the Monte-Carlo analysis of the shear test in Table 4.1 and considering the basis error and analysis error, we estimate the measurement error in higher-order aberration to be less than 12nm.   The estimate of the low-order aberration is limited by uncertainty in the measurement and surface deformations from the support change.

4.5.2. OTHER DATA REDUCTION METHODS

Parks's method (1978) has been used in the situation of measuring axially symmetric surfaces. Based on his method, some calculations were done for the shear test. The parent of the off-axis parabola was represented by Zernike polynomials in the calculation. However, the data reduction process was very sensitive to the noise.

Another way to solve the problem is by integration. The measurement data from the normal position is

$$M1 = mirror(\theta_0) - nulloptics(\theta_0), \qquad (4.9)$$

where θ_0 = the original angle of the mirror and the null optics wavefront.

The measurements after the shear can be described as:

$$M2 = mirror(\theta_0 + \theta_1) - nulloptics(\theta_0),$$

$$M3 = mirror(\theta_0 - \theta_2) - nulloptics(\theta_0), \qquad (4.10)$$

where θ_1 and θ_2 = clockwise and counter clockwise shearing angle.

Subtracting Equation 4.10 from 4.9, one can get data with only the information of the mirror:

$$M2 - M1 = mirror(\theta_0 + \theta_1) - mirror(\theta_0),$$

$$M3 - M1 = mirror(\theta_0 - \theta_2) - mirror(\theta_0),$$

$$M3 - M2 = mirror(\theta_0 - \theta_2) - mirror(\theta_0 + \theta_1).$$

(4.11)

Similarly, by numerically rotating measurement 2 or 3 back to nominal position, one can get

$$M2(-\theta_1) = mirror(\theta_0) - nulloptics(\theta_0 - \theta_1)$$

$$M3(\theta_2) = mirror(\theta_0) - nulloptics(\theta_0 + \theta_2)$$

(4.12)

Subtracting Equation 4.12 from 4.9, one can get data with only the information of the null optics:

$$M2(-\theta_1) - M1 = nulloptics(\theta_0) - nulloptics(\theta_0 - \theta_1)$$

$$M3(\theta_2) - M1 = nulloptics(\theta_0) - nulloptics(\theta_0 + \theta_2)$$

$$M3(\theta_2) - M2(-\theta_1) = nulloptics(\theta_0 - \theta_1) - nulloptics(\theta_0 + \theta_2)$$

(4.13)

With Equations 4.11 or 4.13, one can numerically integrate the surface along the shear line. Here the shear line refers to the line rotationally symmetric about the parent

axis. So data reduction becomes a 1-dimension integration problem. With this method, one cannot get the 2-D surface shape, however.

Equations 4.11 and 4.13 provide very useful data as these manipulations will only contain the information of one of the surfaces. Fig. 4.17 shows one of the shear maps from Equation 4.11. From this shear data figure, higher-order errors in the mirror can be examined. Local irregularities in the surface, which cannot be well described by finite polynomials, can be investigated using this kind of shear data.
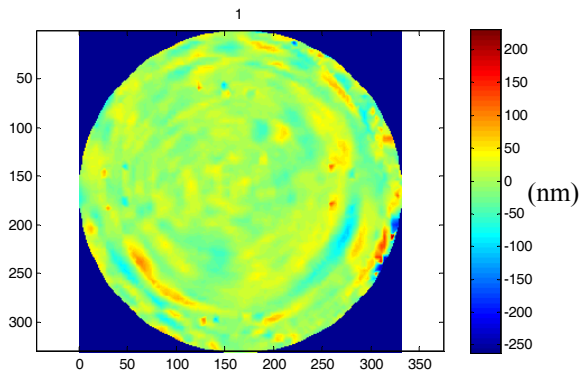
Figure 4.17 Shear data with mirror information only

4.5.3. BASIS FUNCTIONS

Fig. 4.18 shows the estimate of the mirror (higher-order) in which 1023 terms of Zernike polynomials were used. Comparing with Fig. 4.10 (left), more surface details are shown in this estimate. However, as the polynomial terms increase, data storage and computing force requirements also increase dramatically. So better basis functions, which can more completely describe the data with fewer terms, may be worth investigating for a certain type of surface errors.
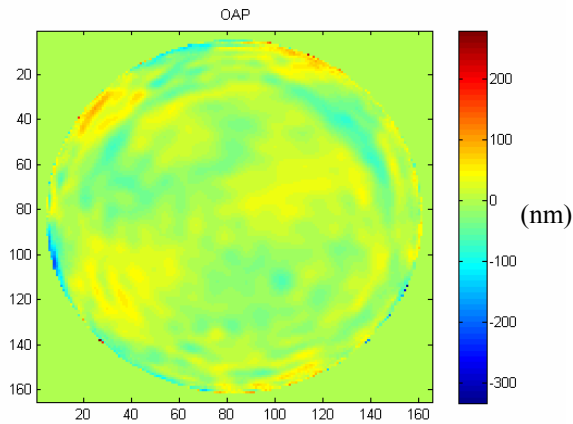
Figure 4.18 Estimate of the mirror with 1023 terms of Zernike polynomials

4.6. SUMMARY

A shear test for an off-axis surface with axi-symmetric parent was investigated. The test allows error separation in the test optics from errors in the surface under test. The accuracy can be further improved by correcting for surface distortion resulting from the support change. Also, a better set of basis functions is worth investigation to improve the description of higher-order surface errors.

In all, this shear test has the advantages of ease of implementation and low cost. It is especially good at detecting high frequency information, low-order errors with large magnitude and local edge effects of the mirror. Consequently, the ML data reduction method is a general tool for reducing the data from the shear test of an off-axis surface with an axi-symmetric parent.

CHAPTER 5

MEASUREMENT OF AN OFF-AXIS PARABOLIC MIRROR WITH A SCANNING PENTAPRISM TEST

5.1. INTRODUCTION

The scanning pentaprism test has been an important absolute test method for flat mirrors, for parabolic mirrors and also for collimation systems (Burge 1993; Yellowhair 2007; Mallik 2007).

During a measurement, a pentaprism is used to relay a collimated beam from an autocollimator or a beam projector to the surface under test. The angle of the reflected beam from the surface is a measure of the surface slope of the mirror. The pentaprism scans in a line along the surface to obtain a series of slope measurements. Integrating the slope data gives the surface profile along the scan. Multiple scans can be combined together to get aberration information of the surface under test. The unique advantage of using a pentaprism is that it deviates light by a fixed angle (nominally 90 degrees) regardless of the orientation of the pentaprism to the incident beam. Thus, the resulting

measurements are relatively insensitive to the prism movement errors or alignment errors. The off-axis segments of Giant Magellan Telescope (GMT) have a conic constant of -0.998286. To verify that the surface being fabricated has the right shape, the scanning pentaprism test has been proposed as another verification test. As GMT mirrors are not ready for the test yet, the 1.7 meter New Solar Telescope (NST) primary mirror was tested recently with the scanning pentaprism method. Since rotational symmetry is broken for an off-axis surface, the test had many differences from measuring flat mirrors or rotationally symmetric surfaces.

In this chapter, the principles and the implementation of the scanning pentaprism test are described, as developed for testing an off-axis parabolic mirror. The sources of error are explained and these are related to the system and component requirements.

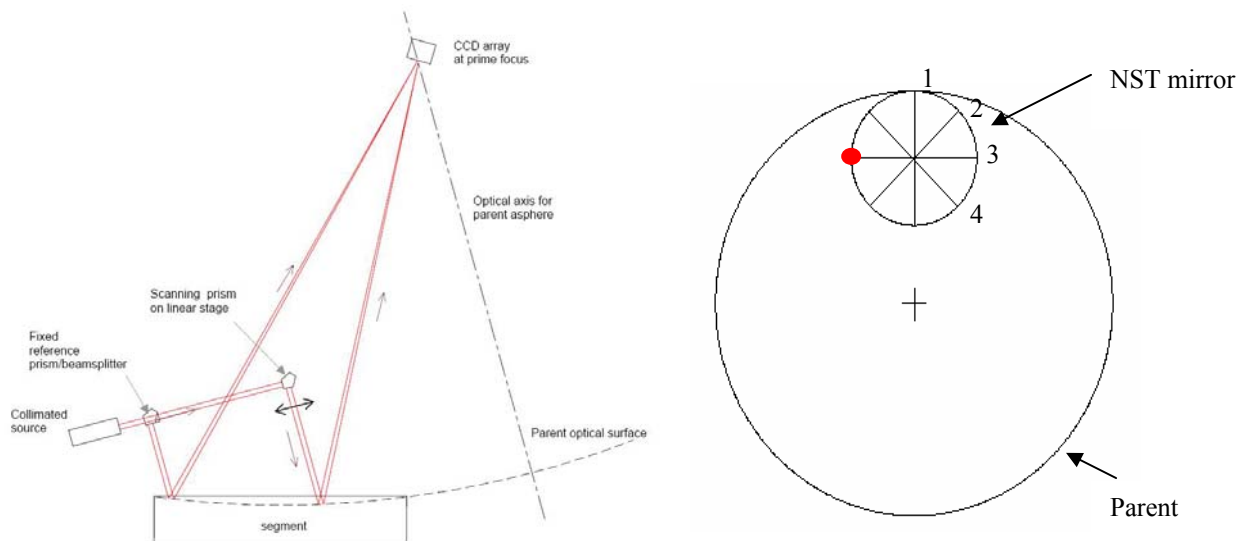## 5.2. PRINCIPLES OF THE NST SCANNING PENTAPRISM TEST

Figure 5.1 Basic principle of the NST scanning pentaprism test (Burge 2006)

5.2.1. BASIC PRINCIPLE

An ideal parabolic mirror will focus on-axis parallel rays to a point at the focus. One can measure errors in the surface by sending parallel rays into the mirror and measuring where they intercept the focal plane. The NST scanning pentaprism assembly (SPA) was developed to create a set of rays that perform the same function. The NST primary is a 1.7m diameter off-axis parabola, with a 1.84 m off -axis distance. The vertex radius of curvature of its parent is 7700 mm. Four pentaprism scans were used to test the mirror as shown in Fig.5.1 (right). The mapping between image space spot location and pupil position gives a complete measurement of the low order surface errors.

The NST SPA uses two pentaprisms on a rail. A collimated light source projects light along the rail. One pentaprism is located at one end of the rail. The other pentaprism can be positioned at any point along the rail using the motor control. The pentaprisms deviate light by 90 degrees, independent of small tilts in the prism itself. The NST mirror focuses these beams to two spots in the focal plane of the mirror. A detector is located there to capture spot images. A correlation method (Jain 2002) is then used to calculate the centers of the spots. With two pentaprisms, errors introduced from rail tilting in slope measurement direction can be removed by measuring the motion of the spot from the scanning prism, relative to the spot motion from the fixed prism.

The correlation method utilizes the concept of the matched filter. It finds the center of the spot by first cross correlating the test spot with a filter image and then using a second degree polynomial fit to find the center of the correlated image data. The filter is a pre-stored spot image file.

The pentaprism provides complete isolation of measurement errors from errors in the motion control system for one direction only. Fig. 5.2 defines the degrees of freedom for the prism as roll, pitch, and yaw. Even though the prism will suffer finite pitch rotation as it is scanned, the deviated beam will have no motion in the pitch direction. Its corresponding direction in the focal plane of the mirror is defined as the in-scan direction, which is the direction for measuring the mirror slope. The direction perpendicular to it is the cross-scan direction. The test spot motion in the focal plane can be divided into the in-scan and cross-scan motion. In-scan motion is insensitive to the tilts of the prism. There are second-order effects, however, that must be considered. The yaws of prisms and the beam projector will introduce quadratic motions in the in-scan direction. Table 5.1 lists sources of line of sight error, to second order. As shown in the table, beam projector pitch also contributes to the in-scan motion. This effect is removed by measuring the differential motion between the spots from the scanning prism and the fixed prism. There is one more important factor that must be considered. The in-scan direction, as defined by the pentaprism, must be determined in the focal plane. An error of $\Delta\theta$ in determining the orientation of the in-scan direction in the focal plane will cause a coupling of roll and yaw into the measurement. This can be expressed as (in-scan error) = (roll and yaw) $\times \Delta\theta$.

Table 5.1 Contributions to line of sight error from prism or beam projector

Contributions to in-scan motion	Contributions to cross-scan motion
Beam projector pitch	Beam projector yaw
(Prism yaw)^2	Prism yaw
(Prism yaw) x (beam projector yaw)	Prism roll

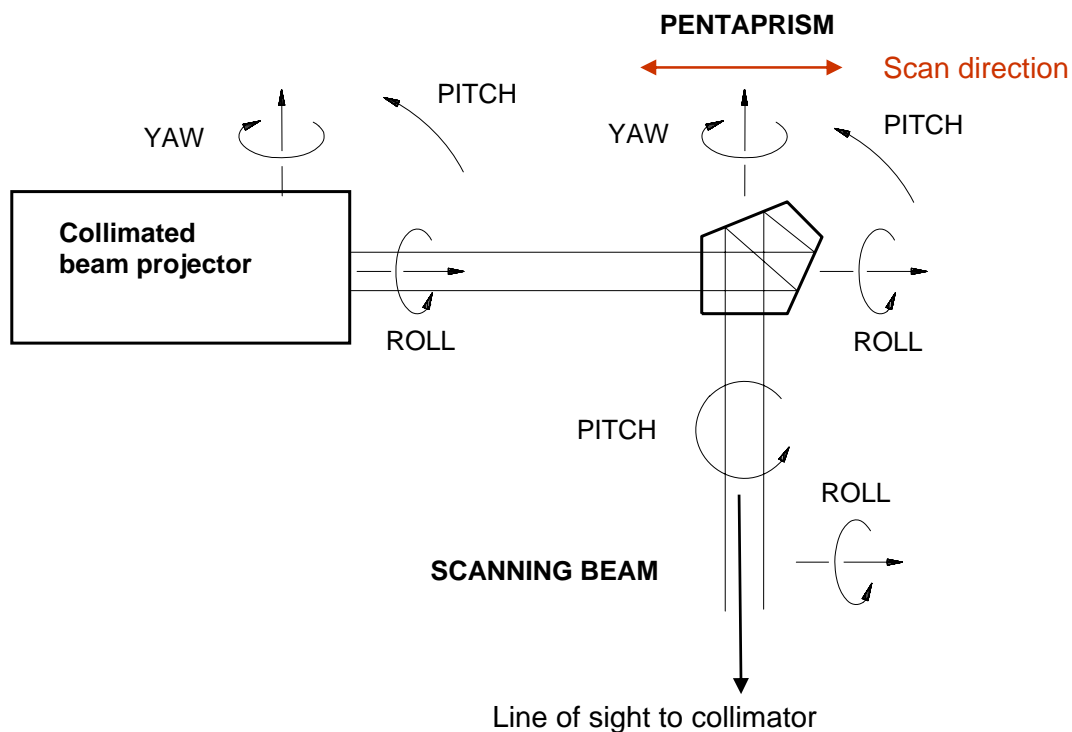| (Prism roll) x (beam projector yaw)	(Prism roll) x (beam projector pitch)
	(Prism yaw) x (beam projector pitch)

Figure 5.2 Definition of degrees of freedom for scanning pentaprism

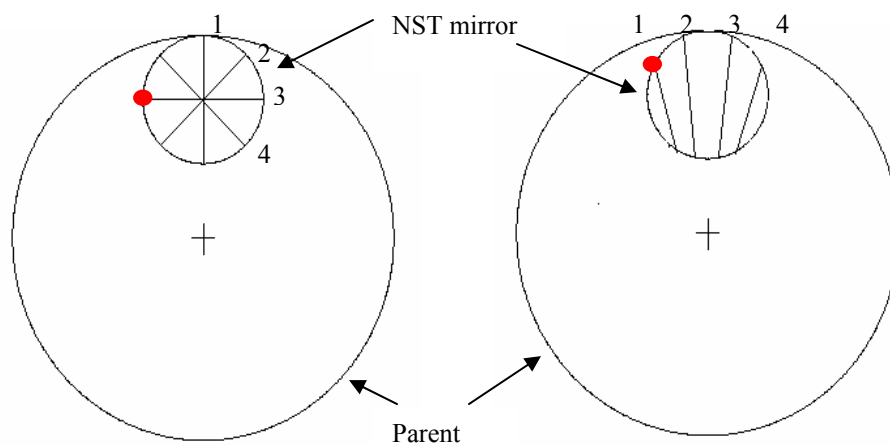## 5.2.2. SCANNING CONFIGURATION

Figure 5.3 Scan configurations

The advantage of the configuration on the right is that the scans pass toward the center of the parent. Rotational symmetry is maintained so that testing an off-axis component is the same as testing a rotational symmetric surface. It will not have the issue of in-scan directions changing at different pupil positions of the mirror as discussed in Section 5.2.5. However, from a Monte Carlo analysis of the test noise sensitivity, where 1urad *rms* Gaussian random noise is added to the slope data, the configuration on the right is about four times more sensitive to the noise than the configuration used during the NST test, as shown on the left. Because the configuration on the right is not good at measuring mirror slopes in x direction.

5.2.3. FIELD ABERRATIONS

If the parabolic mirror is illuminated with collimated light that is parallel to its axis, all reflected rays go through the focal point of the parabola. If these rays are not parallel to the axis, the rays will shift away from the focal point and they no longer intersect at a point. For a full axially symmetric mirror, this effect is described as Seidel coma. The off axis portion simply samples this, which appears as a linear combination of astigmatism and coma in the wavefront. The magnitude of this aberration is linear with the misalignment. Fig. 5.4 shows simulated wavefront maps of the field aberrations given $\pm 0.001°$ incident beam angles in two orthogonal directions, *y* and *x*, which are the directions in the plane symmetry of the mirror and the perpendicular direction. There are

rms 0.149 waves of astigmatism, -0.019 waves of coma and -0.003 waves of trefoil generated in the wavefront due to the field misalignment.

When the fabricated mirror is mounted to the telescope, mirror position (changing field) is also used as a degree of freedom to compensate for the errors in the mirror surface, because field aberration can cancel astigmatism and coma in the mirror surface itself. So an error budget for the mirror segment which is a combination of the surface error and mirror movement (field) was defined for fabrication. During the alignment of scanning pentaprism test, field aberrations need to be aligned to within a certain tolerance.

Since there are field aberrations in the test, measurements from the same field of the mirror are needed during the four scans, otherwise random field aberrations will be introduced to the different scans. This was done by aligning the SPA to focus the light to the same pixel in the detector plane during the four scans.
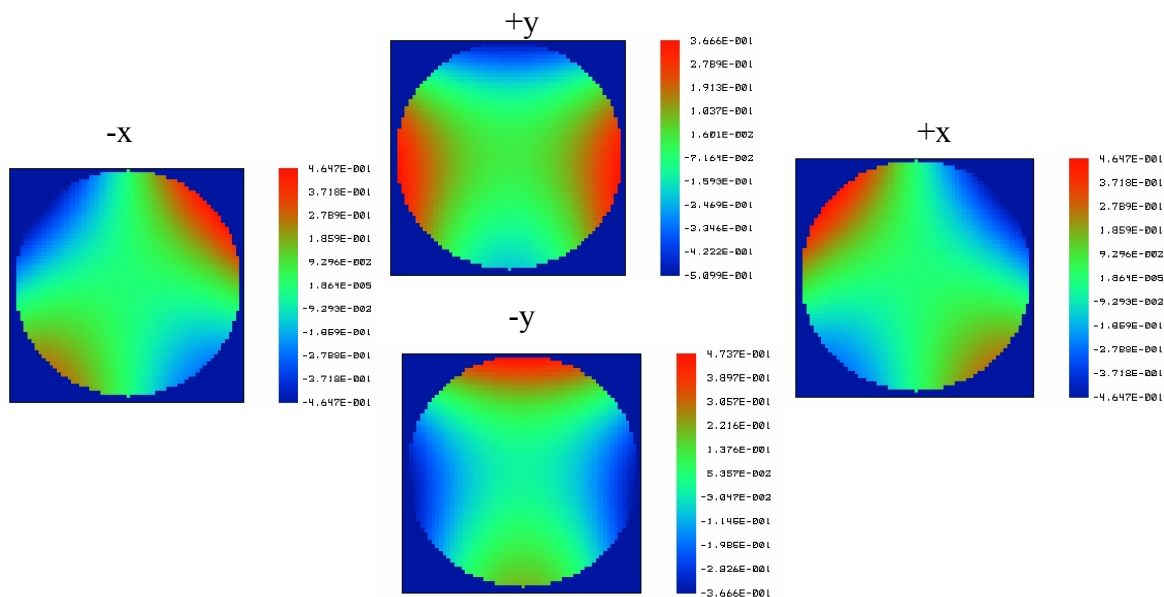
Figure 5.4 Wave aberrations due to 0.001° field of views in waves unit

5.2.4. SPOT DIAGRAMS IN IN-SCAN DIRECTION

Four scans were used to test the NST mirror as shown in the left of Fig. 5.3. The primary purpose of the scanning pentaprism system is to measure lower order aberrations in the system. Figures 5.5-5.12 show how the data appear for each of the four scans (at 0°, 45°, 90°, and 135°) and the wavefront error for the case of the surface error described by a single term of Zernike standard polynomial. In general, all of these aberration terms will be present in the data to some degree, and the amount of each will be determined using a least squares fit. The slope error of the system wavefront can be determined by dividing the ray aberration by the surface focal length 4069.8mm. So one micron in the image plane corresponds to 0.246urad (0.05arcsec) system slope error.
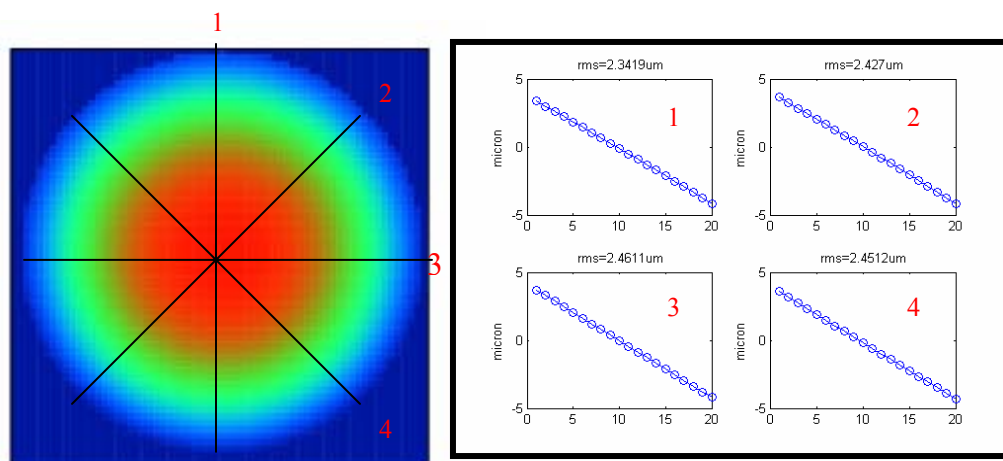
Figure 5.5 Wavefront and spot diagram with 0.18 waves of power
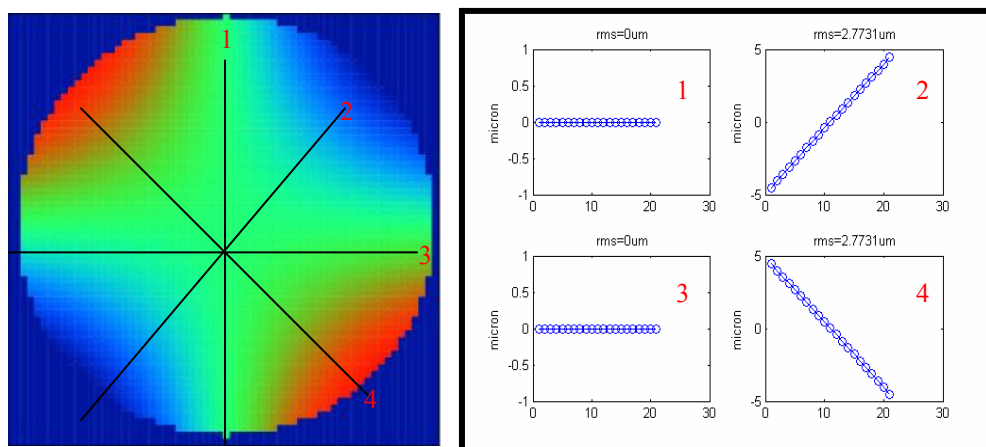
Figure 5.6 Spot diagram with 0.18 waves of sine astigmatism
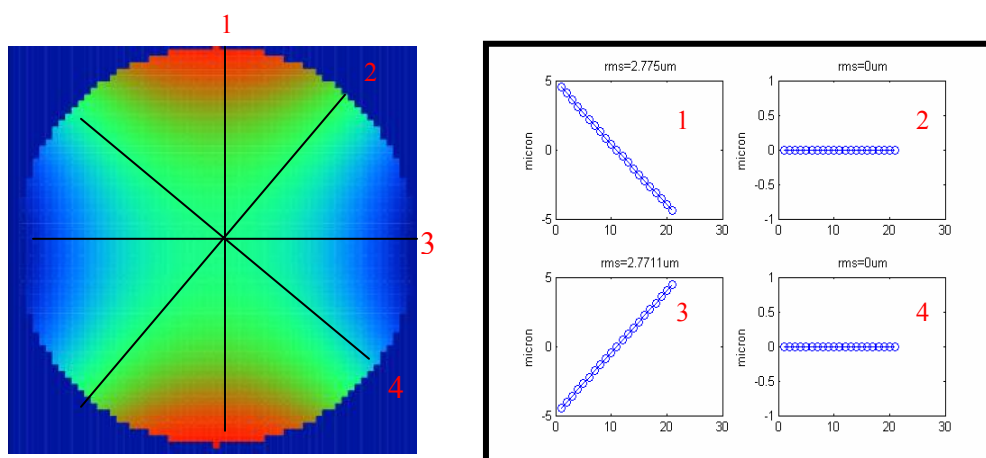
Figure 5.7 Spot diagram with 0.18 waves of cosine astigmatism
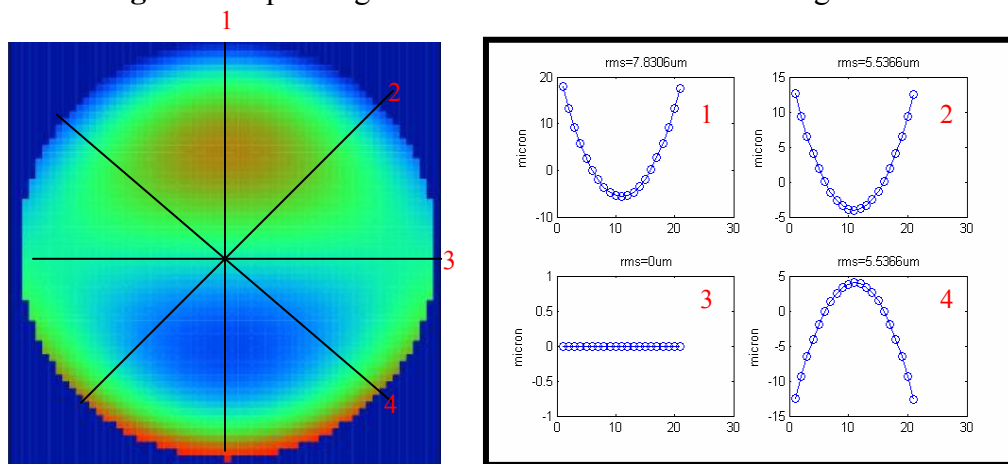
Figure 5.8 Spot diagram with 0.18 waves of sine coma
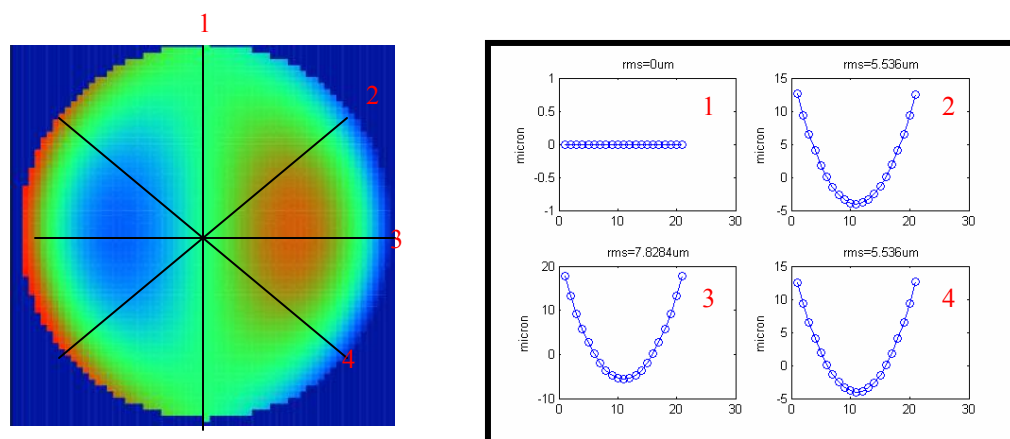
Figure 5.9 Spot diagram with 0.18 waves of cosine coma
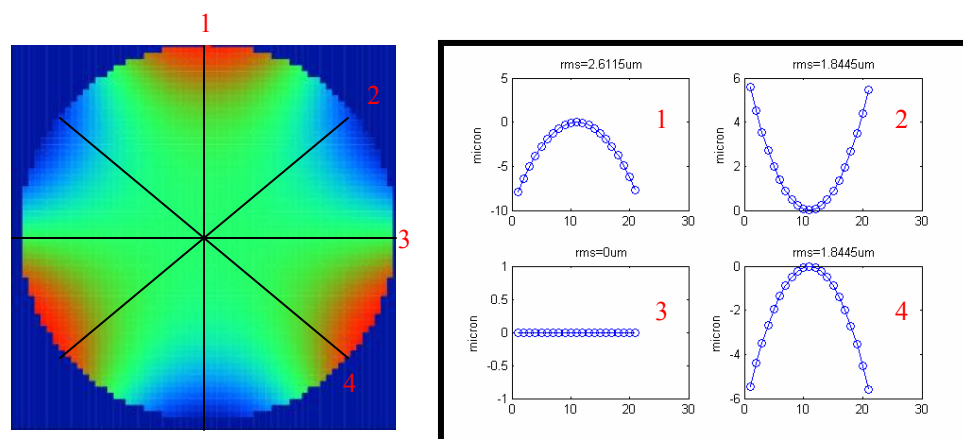
Figure 5.10 Spot diagram with 0.18 waves of sine trefoil
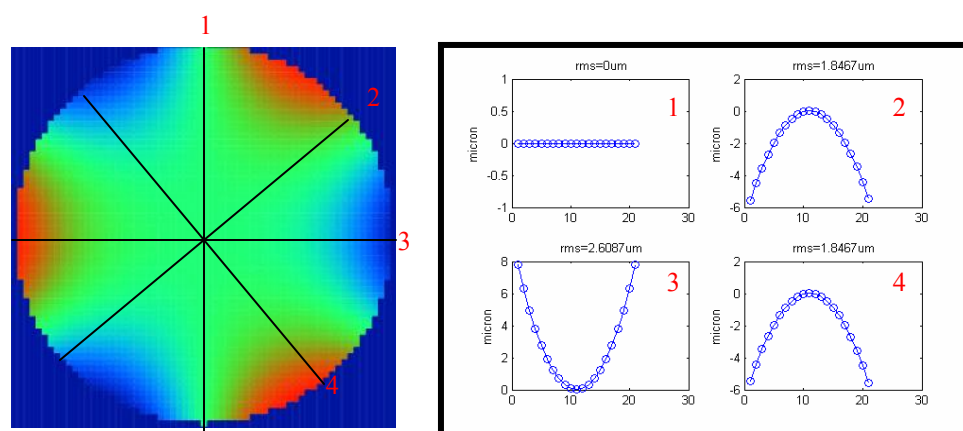
Figure 5.11 Spot diagram with 0.18 waves of cosine trefoil
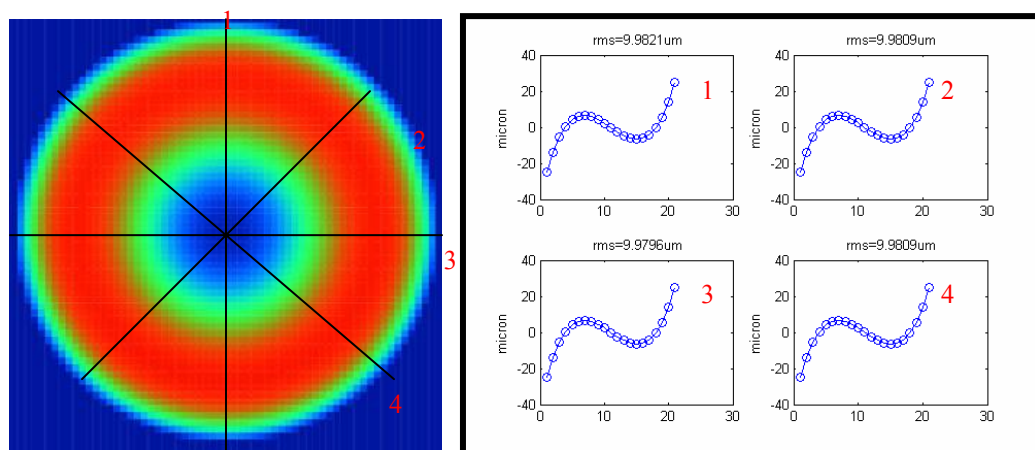
Figure 5.12 Spot diagram with 0.18 waves of spherical aberration

Another set of important plots are the spot diagrams for the four scans where field aberration exists. They are very useful for diagnosing the alignment. With the information of the field aberrations, one can find the right direction to make the field error smaller by focusing the light to another field position. Fig. 5.13-5.16 show the field spot diagrams.
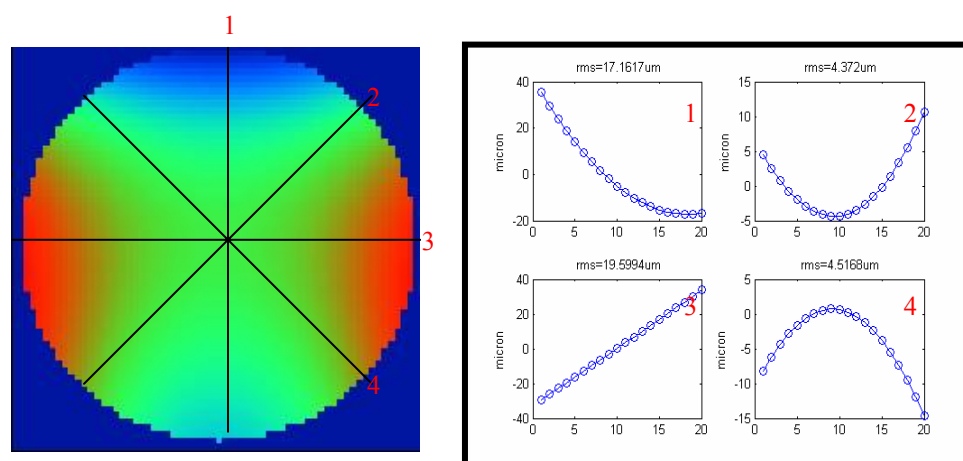
Figure 5.13 Spot diagram of 0.0104° y field
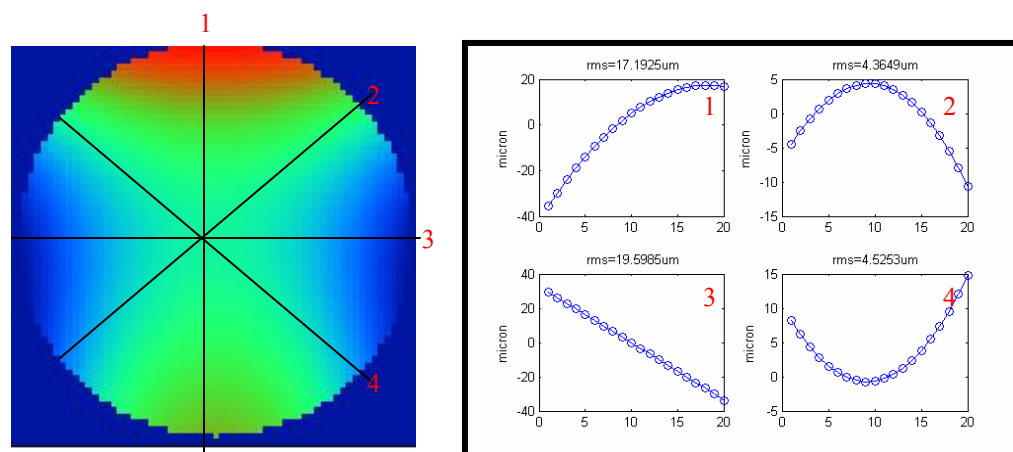
Figure 5.14 Spot diagram of -0.0104° y field
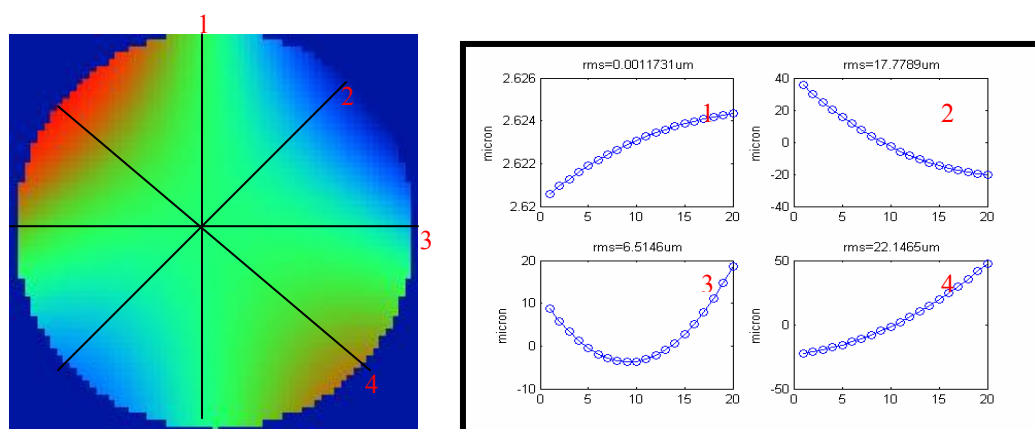
Figure 5.15 Spot diagram of 0.0104° x field
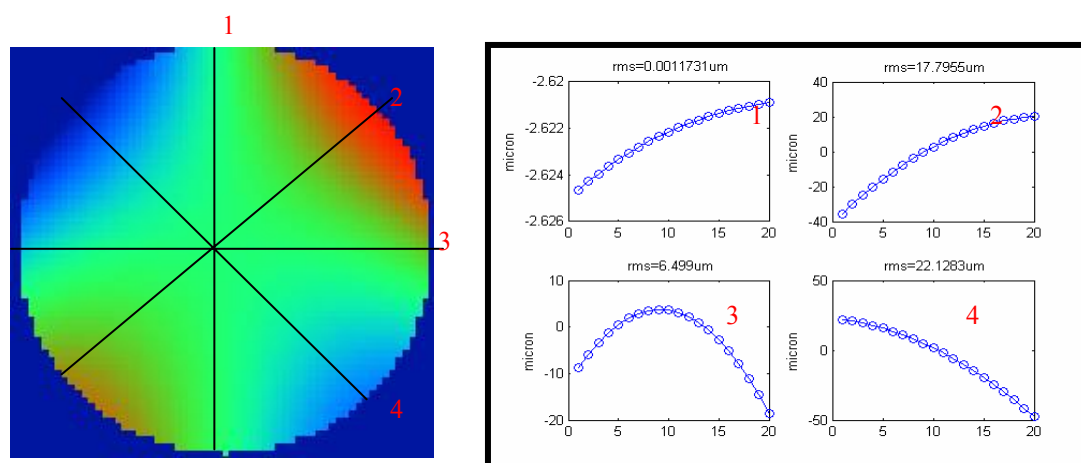
Figure 5.16 Spot diagram of -0.0104° x field

5.2.5. IN-SCAN DIRECTIONS IN THE DETECTOR PLANE

The pentaprism test for an off-axis parabola has some special characteristics when compared with the test for a flat mirror or rotationally symmetric surface.

As shown in the left of Fig 5.3, the four scans no longer pass toward the center of the parent axis of the mirror. Plane symmetry is not available for the scans 2, 3 and 4. Moreover, as an off-axis part of a parabolic surface, the mirror suffers field aberrations. Fig 5.17 shows the field coma in the parent parabola and corresponding field aberration (red) in the off-axis parabola (OAP). For the case of the NST, there is a 2.3:1 ratio between the image location (chief ray) shift and the coma blur in the tangential direction. Field aberration induced spot shift is not small relative to the chief ray shift.
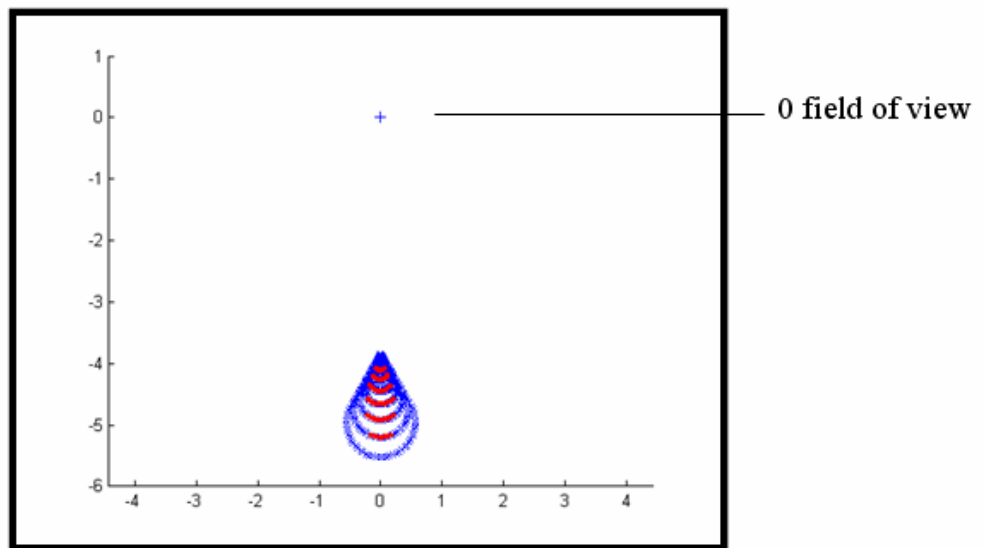
Figure 5.17 Field aberration in the parent parabola and OAP

Because of the two features mentioned above, the in-scan and cross-scan directions of the test in the detector plane are no longer perpendicular to each other but instead change orientation on different pupil locations of the mirror during a single scan.

An intuitive way to understand this is shown in Fig 5.18. A cross-scan motion would introduce a field to the mirror. In the figure, the red spots correspond to the scan 3 in Fig.5.3. The figure shows that as the field changes linearly, which represents pentaprism roll and yaw, the pattern of the field error would be linearly shifted and scaled. Connecting the spots from the same position on the mirror surface with lines, one can see that the scan directions in the focal plane are changing at different positions of the mirror due to the field aberration.

Zero field
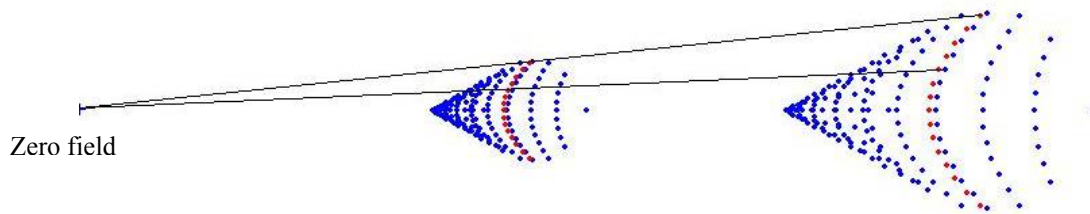
Figure 5.18 Field (scanning) will linearly shift and scale the spot diagram. The cross-scan direction is changed in different pupil positions.

Mathematically, this field effect can be understood by checking the spot trajectories due to the field coma in the parent surface. The spot position at the detector plane can be described by ε_x and ε_y, which are a function of field angles α_x and α_y and aberration W.

$$\varepsilon_x = \alpha_x \cdot f + f / y_p \cdot C \cdot (\frac{\partial W}{\partial x}) \qquad (5.1)$$

$$\varepsilon_y = \alpha_y \cdot f + f / y_p \cdot C \cdot (\frac{\partial W}{\partial y}) \qquad (5.2)$$

where f = the focal length

      C = a constant,

$$C = \frac{y_p^3}{4f^2} \tag{5.3}$$

      y_p = the radius of curvature of the parent surface

      W = field coma in the parent

$$W = (\alpha_x \cdot x + \alpha_y \cdot y)(x^2 + y^2) \tag{5.4}$$

  x and y = normalized pupil coordinates in the parent surface

From equation 5.4, the derivatives of the wavefront errors with respect to the pupil

coordinates can be calculated as:

$$\frac{\partial W}{\partial x} = \alpha_x \cdot (3x^2 + y^2) + \alpha_y \cdot 2xy, \tag{5.5}$$

$$\frac{\partial W}{\partial y} = 2\alpha_x \cdot xy + \alpha_y \cdot (xy + 3y^2). \tag{5.6}$$

Substituting equations 5.5 and 5.6 to 5.1 and 5.2, spot trajectories can be written as:

$$\varepsilon_x = \alpha_x \cdot f + f / y_p \cdot C \cdot (\alpha_x \cdot (3x^2 + y^2) + \alpha_y \cdot 2xy), \tag{5.7}$$

$$\varepsilon_y = \alpha_y \cdot f + f / y_p \cdot C \cdot (2\alpha_x \cdot xy + \alpha_y \cdot (xy + 3y^2)). \tag{5.8}$$

Scanning along line 1 (0°), we have:

$$x=0,$$

$$y=0.368 \text{ to } 1. \tag{5.9}$$

The derivatives of the spot trajectories relative to the field angle can be calculated as in

equations 5.10-5.12.

$$\frac{\partial \varepsilon_y}{\partial \alpha_x} = f / y_p \cdot C \cdot (2xy)_{x=0} = 0 \tag{5.10}$$

$$\frac{\partial \varepsilon_y}{\partial \alpha_y} = f + f / y_p \cdot C \cdot (xy + 3y^2)_{x=0} = 3850 + 1409.6y^2$$

$$\tag{5.11}$$

$$\frac{\partial \varepsilon_x}{\partial \alpha_y} = 0 \tag{5.12}$$

$\dfrac{\partial \varepsilon_y}{\partial \alpha_x}$ and $\dfrac{\partial \varepsilon_x}{\partial \alpha_y}$ are equal to zero. It means there is no coupling between the two

directions, the in-scan and cross-scan direction are perpendicular to each other.

Scanning along line 3, we get:

$$x = -0.316 \text{ to } 0.316,$$

$$y = 0.684, \tag{5.13}$$

and

$$\frac{\partial \varepsilon_x}{\partial \alpha_y} = f / y_p \cdot C \cdot (2xy)_{y=0.684} = 642.7912x \tag{5.14}$$

$$\frac{\partial \varepsilon_x}{\partial \alpha_x} = f + f / y_p \cdot C \cdot (3x^2 + y^2)_{y=0.684} = 3850 + 1409.6x^2 + 219.8346 = 4069.8 + 1409.6x^2$$

$$\tag{5.15}$$

$\dfrac{\partial \varepsilon_x}{\partial \alpha_y}$ is not equal to zero, so there is coupling between the two directions. The angle

between the two directions can be calculated from Equation 5.16. Fig. 5.19 shows that the

angle changes at different scanning positions, which is also verified by a numerical simulation in ZEMAX.

$$angle = \arctan(\varepsilon_y, \varepsilon_x)$$
$$= \arctan(\alpha_y f + \frac{y_p^2}{4f}\alpha_y(xy + 3y^2), \frac{y_p^2}{4f}\alpha_y(2xy)) \tag{5.16}$$

Pupil position
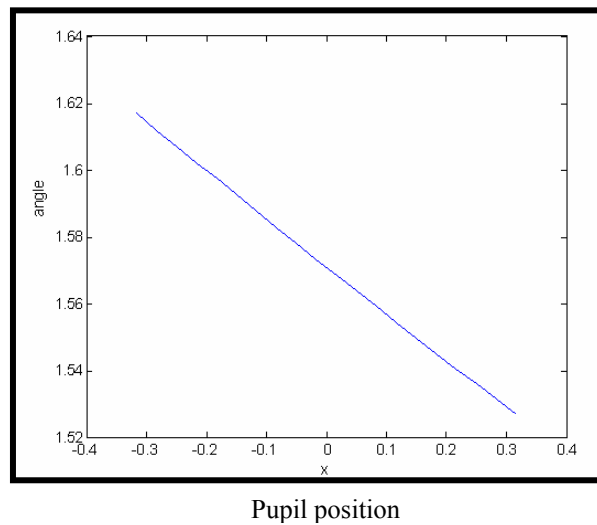
Figure 5.19 The angle between in-scan and cross-scan in detector plane

Similar results can be derived for scanning along lines 2 and 4.

5.2.6. DETECTOR ORIENTATION
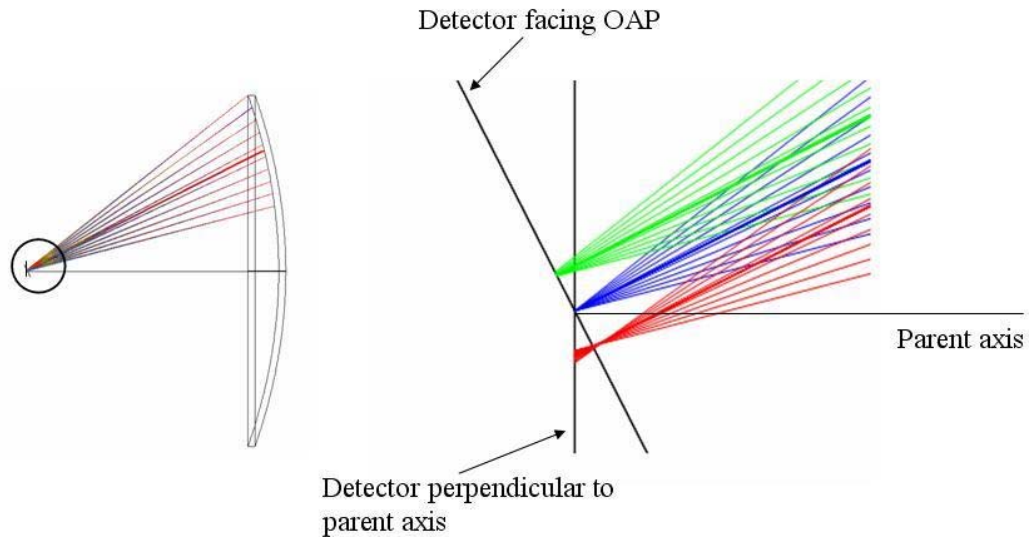
Figure 5.20 Ray tracing plot of the NST mirror at its focal plane

As shown in the ray-tracing result above, when the detector is facing the axis of the parent parabola, the field alignment error will introduce defocus to the spot distribution. When the detector is facing the axis of the *OAP*, the field will shift the image along the detector; power is automatically compensated for by the tilt of the detector. The angle between these two situations is 26.7°. In the experiment, the detector was mounted to face the center of the *OAP* to minimize the defocus effects.

5.2.7. CALIBRATION OF DETECTOR COORDINATES

During the pentaprism test, a detector was mounted at the focal plane of the mirror. Light after reflecting off the mirror focused at certain pixels of the detector. From the spot locations on the detector, the focal point of the mirror was determined in the

detector pixel coordinate system. Knowing the coordinate relation between the mirror and the detector, coordinates of the focal point relative to the mirror can be determined. This information can be used to determine focal length and other geometry parameters of the mirror as discussed in Section 5.3.5.2. To get the coordinate relation between the mirror and the detector, a laser tracker (an optical coordinate measuring machine) was used for coordinate measurements. Mirror coordinates were obtained by directly touching the mirror with the tracker ball and reading out the tracker ball coordinates. For detector coordinates, three laser tracker balls were attached to the mount of the detector. Detector coordinates were determined by calibrating the tracker ball locations relative to the detector pixels.

The calibration was done with a laser tracker and an interferometer. After light from the interferometer focused at a certain pixel of the detector, the laser tracker was used to read out the coordinates of the three tracker balls. Then the detector was moved away and another tracker ball was aligned to the interferometer so that the light was retro-reflected back to the interferometer. The coordinates of this tracker ball were also read by the tracker. Repeating the process above for different pixels in the detector, a mapping relationship between the pixel location of the focusing spot, its coordinate from the tracker measurement and the coordinates of the three balls were obtained. Coordinates of other pixel positions could be linearly interpolated from this mapping. So during a scanning pentaprism test, knowing the coordinates of the three tracker balls and which pixel the light focuses on, the coordinates of that pixel (focus of the light) in the tracker coordinate system can be calculated. With the mirror coordinates obtained by

touching the mirror with tracker balls, the position of the focal point relative to the mirror can also be determined.
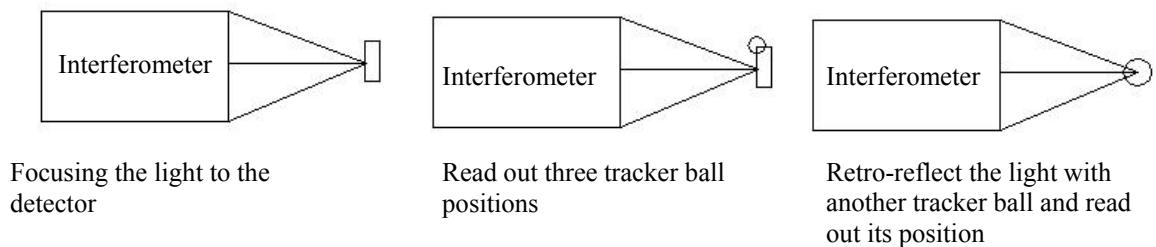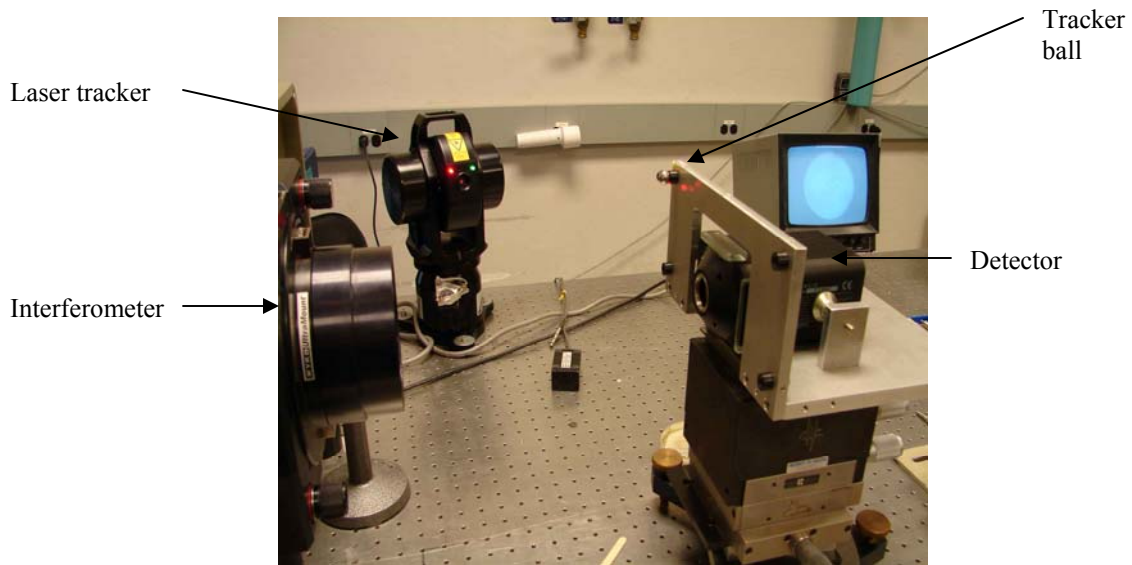
Figure 5.21 Detector calibration setup and procedure

5.3. SCANNING PENTAPRISM EXPERIMENT

5.3.1. SPA COMPONENTS

5.3.1.1. BEAM PROJECTOR: LIGHT SOURCE

The beam projector uses a single mode fiber coupled laser with a 635 nm wavelength as its light source. The numerical aperture (*NA*) of the light is 0.12. Assuming

a Gaussian distribution of the light irradiance with respect to *NA* as shown in Fig.5.22, light beam with *NA* less than 0.06 corresponds to an irradiance variation less than 80%.
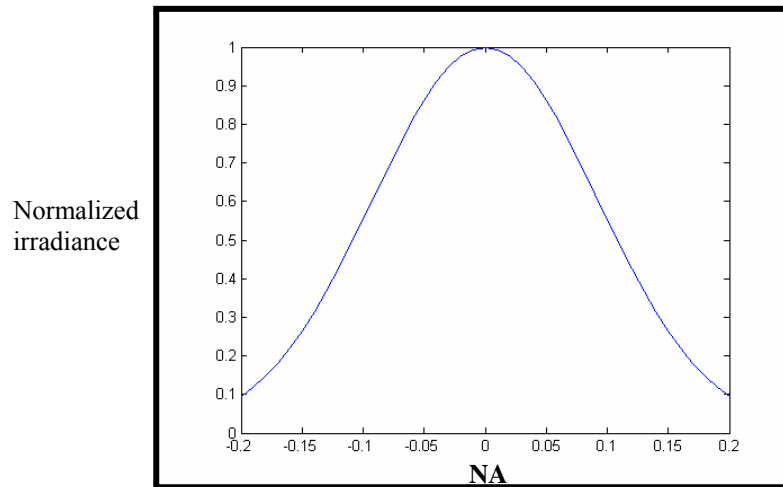
Figure 5.22 Light source irradiance distribution with respect to its NA

5.3.1.2. BEAM PROJECTOR: COLLIMATING SYSTEM

A 50mm diameter doublet with focal length 500mm is used to collimate the light. Fig.5.23-5.24 shows the design layout and its design on-axis performance in which the wavefront *rms* value is 0.006 waves. The image space *NA* is designed to be 0.05, which corresponds to less than 14% light intensity variation from the fiber coupled laser source. When the system is misaligned, the light source is off axis, and field aberrations will be introduced to the beam projector. Coma is well corrected by the doublet; astigmatism changes quadratically with the misalignment as shown in Fig. 5.25.

50mm collimated
beam
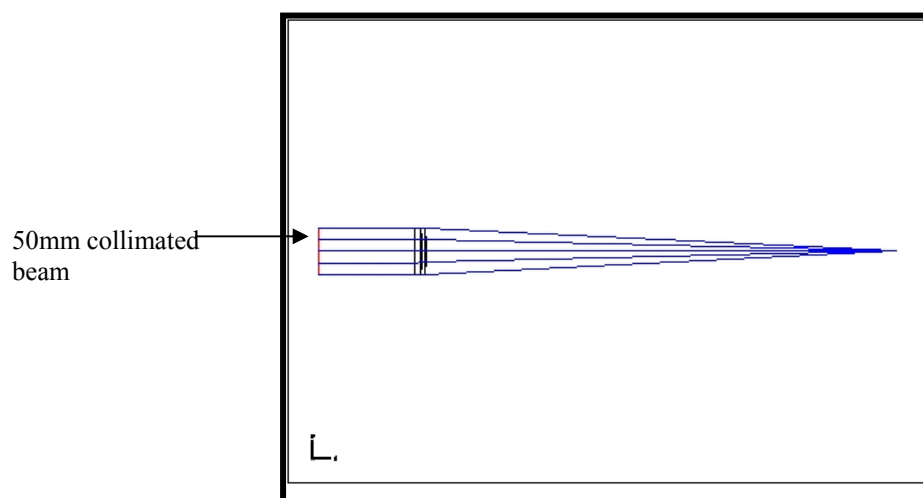
Figure 5.23 Design layout of the collimating lens
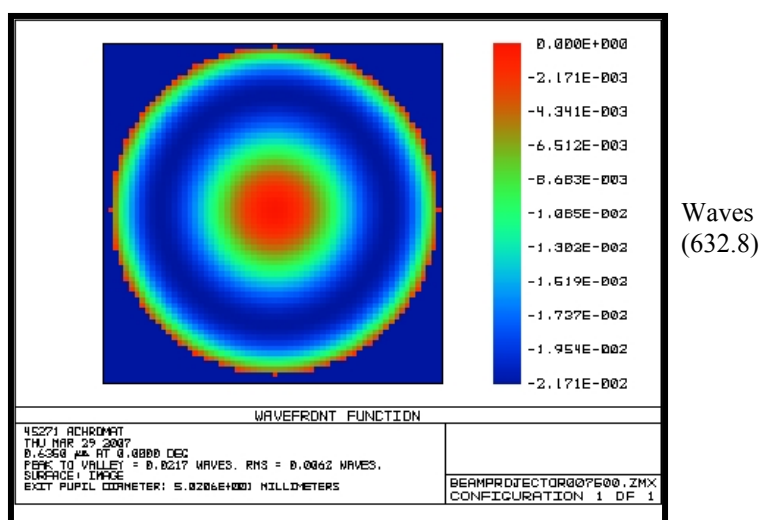
Waves
(632.8)

Figure 5.24 On-axis performance of the collimating lens based on nominal design,
rms=0.0062 waves
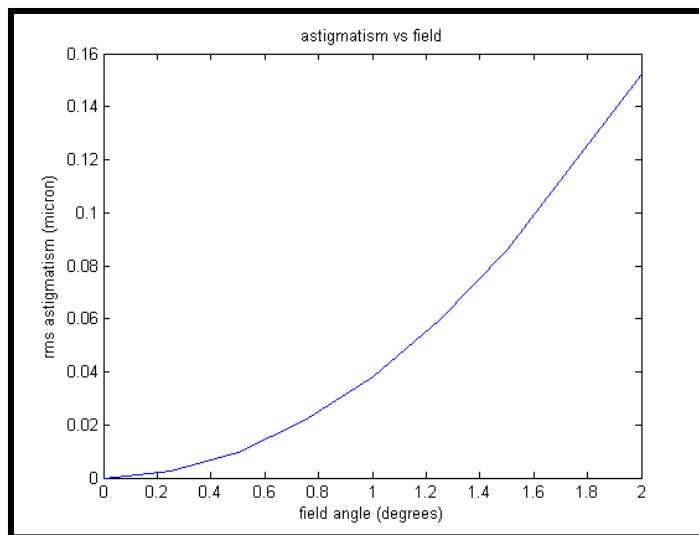
Figure 5.25 The relation between wavefront astigmatism in the 50mm collimated beam and misalignment of the light source

Because there is unexpected spherical aberration in the doublet we bought, only a 20mm aperture of the collimating lens was used in the experiment. The beam projector design has considered phase errors, amplitude variations and diffraction effects coupling with respect to the prism shift. These effects will be explained in the error analysis section.

5.3.1.3. SCANNING SYSTEM

The scanning prism was mounted to the rail on an actively controlled platform which was used to control the roll and yaw of the prism with Pico-motors. In addition, an autocollimator was mounted to the rail to monitor the yaw of the prism. The prism can be stabilized in roll and yaw using measurements of the prism yaw from the autocollimator and the cross-scan information measured in the detector plane.

5. 3.1.4. DETECTOR

The operation of the test used a single 1.6k x 1.2k x 7.4 micron pixel CCD at the focal plane of the NST mirror. The read-out rate of the detector is 18MHz. The signal to noise ratio is 58dB. Exposure time was controlled to 0.5ms during the experiment so that the light source would not saturate the CCD. There is a 850μm thick protecting silica glass plate on top of the CCD pixels. The glass plate contributes a small amount of spherical aberration to the test result and this effect was removed numerically using the parameters of the glass plate.

5.3.2. DEMONSTRATION SETUP
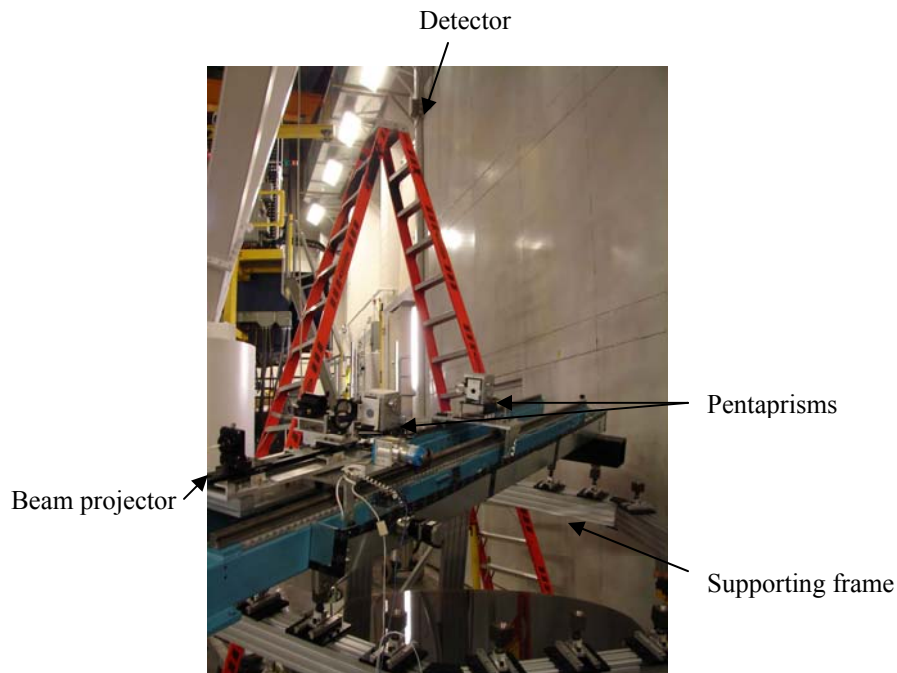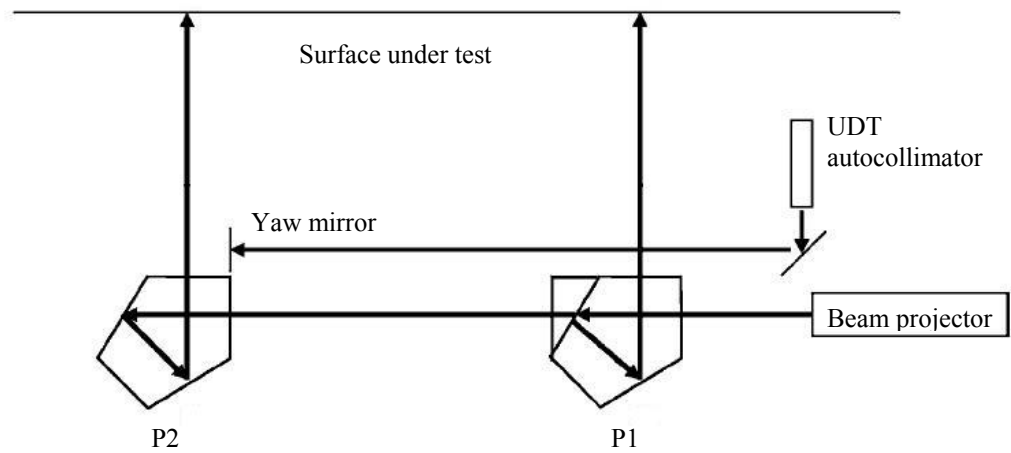
Figure 5.26 Scanning pentaprism demonstration layout and schematic plot of the scanning system
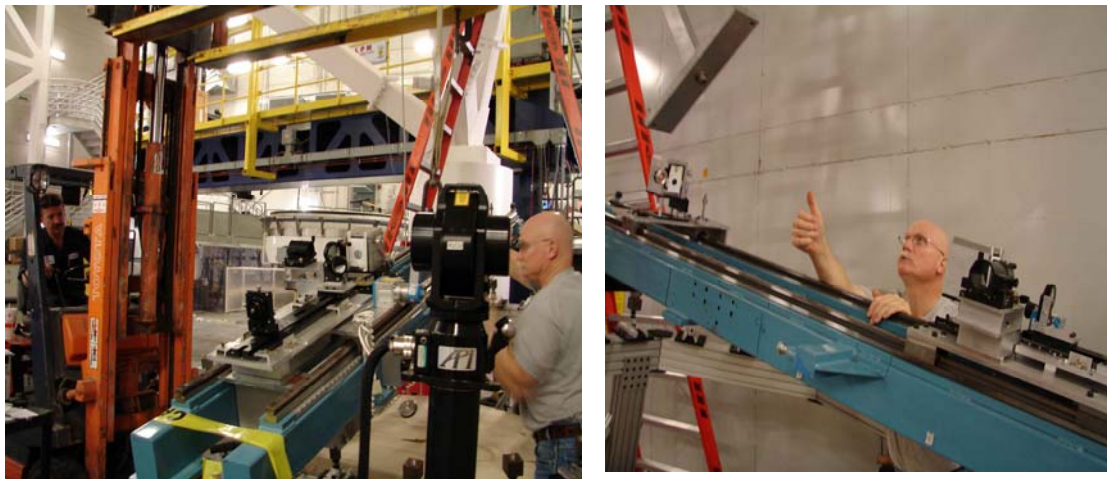
Figure 5.27 Jude and Rod are rotating the rail using a fork lift

The demonstration setup is shown in Fig. 5.26. A coordinate system was first built with the laser tracker. The mirror center was adopted as the origin; the North-South

direction was on the *y*-axis, and East-West was on the *x*-axis. Then the mirror, rail supporting frame and the mounting cups were set up to the design positions with the help of the laser tracker. The rail had the beam projector and pentaprisms on top of it. It had three balls on its back side, which sat in the mounting cups of the supporting frame during the scan. By adjusting the screws of the cups, the tilt angles of the rail could be changed. Scanning of the pentaprism was driven by a stepper motor. The position of the pentaprism was found by counting the steps of the motor. The yaw and roll of the pentaprisms could be adjusted with Pico-motors. A computer program written by Grant Williams was used to control the Pico-motors, step motor, and detector. Four scans were taken in a measurement. The rotation of the rail between the scans was realized by using a fork lift as shown in Fig.5.27.

5.3.3. SYSTEM ALIGNMENT

5.3.3.1. BEAM PROJECTOR ALIGNMENT

The beam projector was collimated with a shear plate interferometer. Because there was spherical aberration in the collimating lens, the size of the beam was stopped down to 20mm. When aligning the beam projector with the rail, an iris was used to shrink the beam to less than 1mm; the tip and tilt of the beam projector were adjusted so that the light spot falling on the scanning pentaprism stayed unchanged as the prism was moved to different positions along the rail. The beam projector was aligned to have less than 1mm spot movement throughout the 2m long rail.

5.3.3.2. PRISM YAW ALIGNMENT

Prism yaw has a second-order effect on the in-scan direction slope measurement, so the yaw angle of the prisms needed to be adjusted to within tolerance.

By looking at the spot reflected from the front surface of the pentaprism, the pentaprism yaw angle was primarily aligned to retro-reflect back the collimating beam. The prism yaw was further adjusted by perturbing the yaw with the Pico-motor and evaluating the projected value in the in-scan direction. The in-scan direction can be obtained by perturbing the roll of the pentaprism. The cross-scan direction due to the yaw can also be found by perturbing the yaw of the pentaprism. The cross-scan direction due to the yaw should finally match the cross-scan direction due to the roll. So by monitoring the yaw cross-scan direction, one can quickly adjust the yaw close to the preferred region. Finally, the prism yaw was adjusted so that the in-scan projection value stayed at its quadratic minimum. In the experiment, the yaws of both prisms were adjusted to better than 10urad. The scanning pentaprism yaw was changing due to the errors in the rail. It was monitored by the UDT, an electronic autocollimator. The variation of it was ~ 0.1mrad in the experiment.

5.3.3.3. PRISM ROLL CONTROL

Using the image spot location on the camera as feedback, the roll of the scanning pentaprism was maintained to its nominal position by adjusting it with the Pico-motor. In the experiment, the roll-induced cross-scan motions in the detector plane were controlled to less than 0.02mrad.

5.3.3.4. CALIBRATION OF THE IN-SCAN AND CROSS-SCAN DIRECTIONS

Due to the field coma effect, the projection of the cross-scan direction to the focal plane repeatedly changed at different locations of the mirror. The cross-scan directions were measured by changing the roll of the pentaprism to two extreme roll values. The direction was determined to better than 0.5mrad in the experiment. The cross-scan direction of the static pentaprism was different from that of the scanning pentaprism, so it also needed to be calibrated. After obtaining the cross-scan directions at 10 positions per scan, the cross-scan values at other positions were linearly interpolated. The linearity was verified by both a numerical simulation and experiments.

The in-scan direction is the direction perpendicular to the cross-scan direction. So the determination of the in-scan direction was accurate to 0.5mrad in the test. This coupled with the 0.02mrad cross-scan error to cause in-scan errors of 10nrad.

5.3.3.5. COMBINING SCANS

For each scan, the scanning pentaprism was first moved to the center of the mirror. Then the rail and the roll of the pentaprism were simultaneously adjusted so that the spot on the camera fell at a certain pixel position. Adjusting the spot to fall at the same pixel of the camera during the four scans ensured that the same field of view of the mirror was measured, if the positions of the mirror and the camera stayed unchanged during the scans.

5.3.4. DATA COLLECTION AND REDUCTION PROCESS

5.3.4.1. DATA COLLECTION AND REDUCTION

The scanning pentaprism was driven by the motor to sample different positions on the mirror. Images were recorded after the spot roll correction was performed. The correlation method was used to find the centers of the static and scanning spots. The centers were then projected to the in-scan directions. After that, the static-spot movements were subtracted out from the scanning-spot movements. After getting the in-scan spot displacements of the four scans, the spot displacements were divided by the focal length to get the slope values of the mirror. The slopes were then fitted to the Zernike slope polynomials to obtain the wavefront coefficients of the system. By further fitting the coefficients with field aberrations, which are certain combinations of coma and astigmatism, the field alignment requirement could be obtained for further adjusting the field of the pentaprism scanning system.

During data collection, a laser tracker was used to monitor the position changes of the mirror and the detector. This information was then used to add correcting values to each scan. In the experiment, the position changes were less than 25μm.

During data reduction, the surface high frequency data obtained from interferometric measurement were used to subtract out the high frequency surface data from the scanning pentaprism test. This reduced the high-frequency coupling effect as discussed in error analysis section. From the interferometric measurement results, the spot variation due to the high frequency errors in the mirror was 3~ 4μm *rms*.

Fig. 5.28 gives the data collecting and processing flow diagram.

Move the scanning pentaprism to the center of the mirror and align the moving spot to a certain pixel

Scan to different positions, correct roll of the pentaprism and record images

Find centroids, project to in-scan direction and subtract reference spot movement

Remove high frequency coupling effect from the spot data

Remove effect of changes in mirror and camera position

Fit slope data to get wavefront coefficients

Further fit to get alignment information

Report measurement results

Figure 5.28 Pentaprism test data collecting and processing flow diagram

5.3.4.2. A DATA PROCESSING EXAMPLE

5.3.4.2.1. IN-SCAN DATA COLLECTION
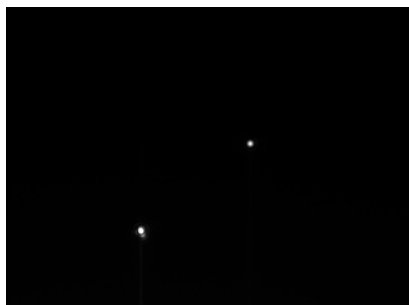
Figure 5.29 A scanning picture of a 90 ° scan

Fig. 5.29 shows an example of the spot images obtained in a 90° scan. The spot in the lower left is from the fixed prism, while the spot in the upper right is from the scanning prism. After collecting the spot images at different positions of the mirror in a scan, centers of the spots were calculated by the correlation method. Fig. 5.30 (a) shows the centers of the scanning spot in the 90° scan. Fig. 5.30 (b) shows the centers of the reference spot in the 90° scan.
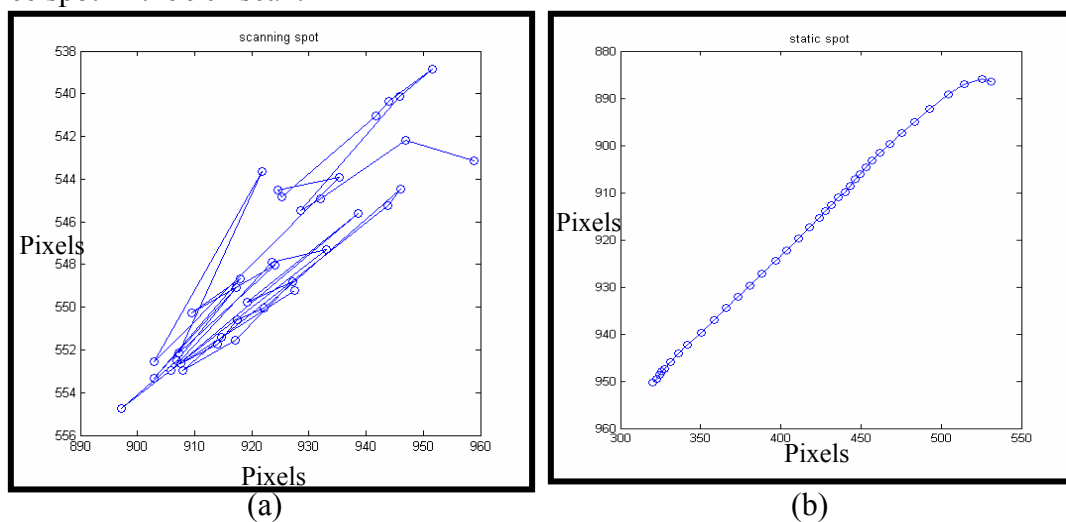
Figure 5.30 Center distributions of the scanning and reference spots from a 90° scan

Data were further reduced by projecting the spot centers to their corresponding in-scan directions. Fig.5.31 shows the in-scan data.
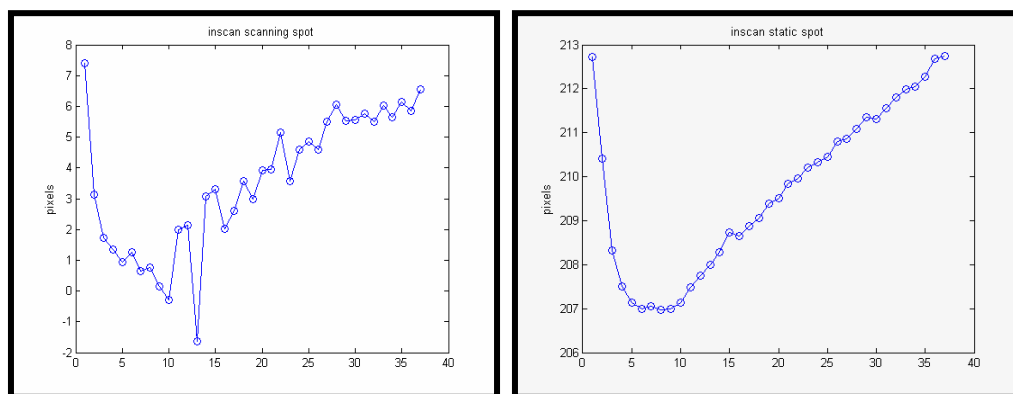
Figure 5.31 In-scan data of scanning and reference spots

Finally, an in-scan spot diagram related to surface slopes was calculated by removing the reference spot motions. Fig. 5.32 shows the finial in-scan data of the 90° scan.
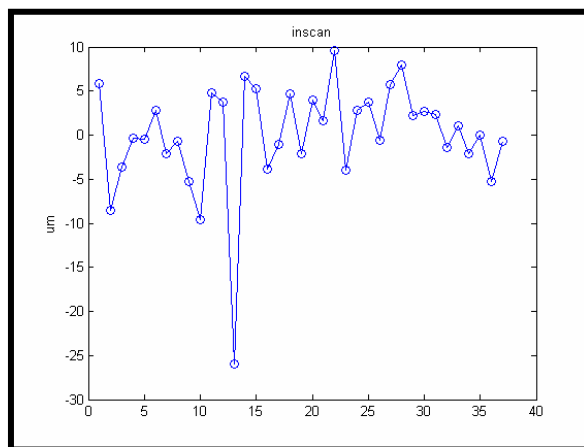
Figure 5.32 In-scan data of a 90° scan

5.3.4.2.2. Compensating field effect from beam projector pitch

The magnitude of the field aberrations is a function of position in the pupil. This caused the static spot and the scanning spot to have different amount of motions when the beam projector changed in pitch, since the two beams from the pentaprisms sampled different pupil positions. This effect was simulated with a ray tracing program. The motion scale factors between the static spot and the scanning spot were calculated and checked with experiments. Figure 5.33 shows the scale factors for the zero degree scan. Data were normalized to the value of the reference spot (point 38). As shown in the figure, the movement of the sampling point 1 due to the pitch of the beam projector can be obtained by multiplying the in-scan motion of the static spot by 0.978. Then this in-scan motion from beam projector pitch can be removed from the prism data.
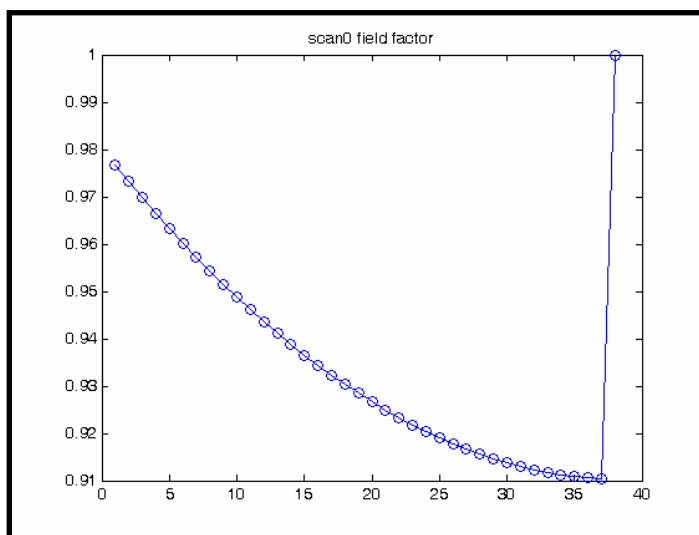
Figure 5.33 Field effect correction factors of the 0° scan

5.3.4.2.3. Mirror and detector motion compensation

The laser tracker was used to monitor the motions of the mirror and the detector during the four scans. Three tracker balls were mounted to the mirror, and another three balls were mounted to the camera. A coordinate system with the mirror center as the origin, the North-South direction as the *y*-axis, and the East-West direction as the *x*-axis, was used as the tracker coordinate frame. Table 5.2 shows the coordinate changes of the mirror and the detector during other scans relative to the 90° scan in a measure.

Table 5.2 Mirror and camera coordinates variation

	45°-90°			135°-90°			0°-90°		
	x	y	z	x	y	Z	x	y	z
Mirror coordinate variation (µm)	-11.9	-0.7	2.3	-11	-0.8	1.7	-14.4	-2	2.3
	-10.2	-2	0.4	-7.6	-0.9	0.4	-12.2	-0.2	2.5
	-10.9	1.5	4.9	-6.5	-0.4	2.2	-11.6	4.5	7.8
Camera coordinate variation (µm)	-3.6	23.2	-21.4	-3.6	-13.3	11.5	-0.2	19.7	-17.8
	-4.2	31.4	-28.2	4.3	1.7	-0.4	-4.4	16.1	-15.1
	-11.8	30.9	-33.2	5.3	7.4	-5.8	-10.6	29.9	-31.9

From the 45°-90° data, the detector moved 28µm in y and -27 µm in z. The shift in y is equivalent to a field angle of 0.00039419. The field coma shown in Fig.5.34 (a) and the 27µm power shown in Fig.5.34 (b) were generated from the simulation program and added to the 45° scan data for compensation.

(a)   (b)
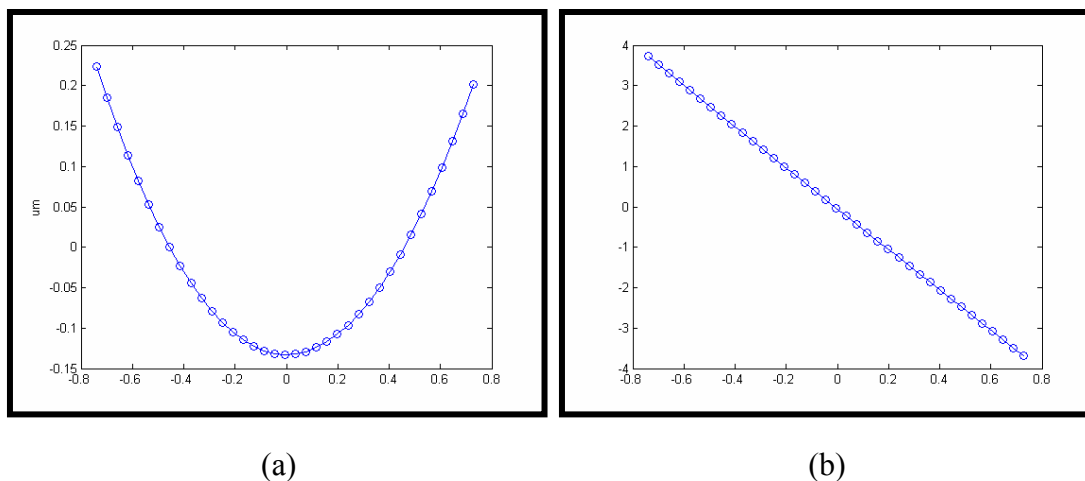
Figure 5.34 Generated mirror and detector compensation data for 45° scan

Similarly, from the 0°-90° data, the camera moved 22µm in y and -21µm in z. The resulting aberrations were also compensated in the data reduction process.

5.3.4.2.4. HIGH FREQUNCY DATA REMOVAL

Data from the scanning pentaprism test were used to estimate lower-order surface errors only. Higher-frequency errors in the mirror, as they join the estimate, will perturb the estimates of the lower-order aberrations. To reduce this coupling effect, high frequency data from the interferometric measurement were used to subtract the data from the pentaprism test.

Fig. 5.35 shows the data from the scanning pentaprism in red, which includes the wavefront low-order aberrations, and a small amount of residual field aberration. The data in blue were generated from interferometric measurement, in which low-order aberrations up to spherical aberration were removed from the data. The two sets of data matched very well as shown in the figure. This means that the higher-order aberrations in

the mirror had been well measured and could be well corrected. The only exception is the 45° scan, in which the data did not match well. Further experiments are needed to understand this discrepancy.
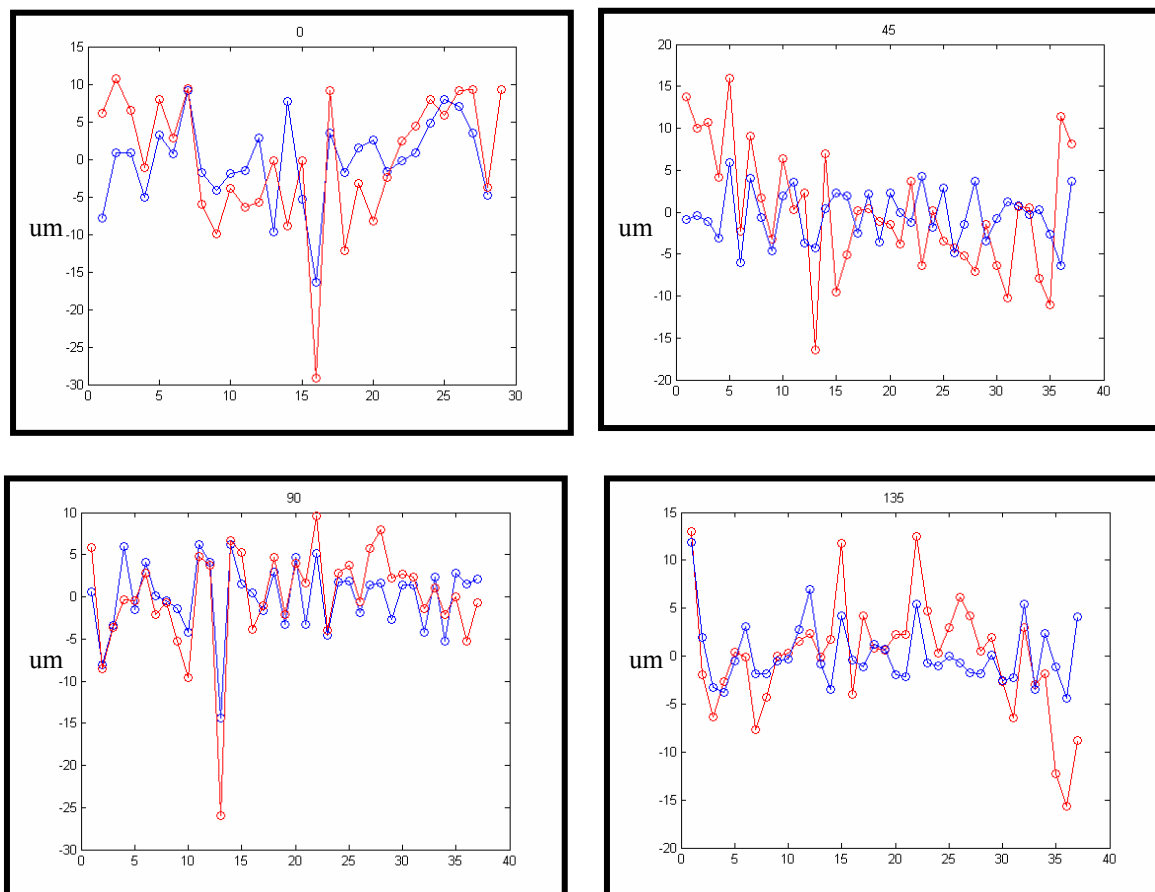
Figure 5.35 Interferometric data and scanning pentaprism data

5.3.5. DEMONSTRATION RESULTS

5.3.5.1. SURFACE MEASUREMENT RESULT

Four scans were taken to get a measurement of the surface figure. After several iterations of measuring and adjusting the alignment, the SPA was finally well-aligned to the mirror. Then two sets of measurements were taken on two different days. The

difference of the results was 13nm *rms*. Thirty-seven points were sampled during each scan. At each scanning position, the spot images were averaged five times. Fig.5.36 shows the spot diagrams obtained from the different scans without any compensation. The spot diagrams, only corrected with high-frequency data from interferometric measurement, are shown in Fig. 5.37. Since the 45° scan data did not match well with the interferometric data as mentioned above, it was not compensated with the interferometric data during the data process. Fig. 5.38 gives the spot diagrams only corrected for motion of the mirror and detector. Fig. 5.39 shows the spot diagrams used for the finial data reduction, which have been corrected with high-frequency data and tracker data. Fig.5.40 shows the polynomial fitting result, and Fig.5.41 shows the residuals after the fitting coefficients were removed. Fig. 5.42 shows the surface measurement. The coefficients of the surface errors are shown in Table 5.3.
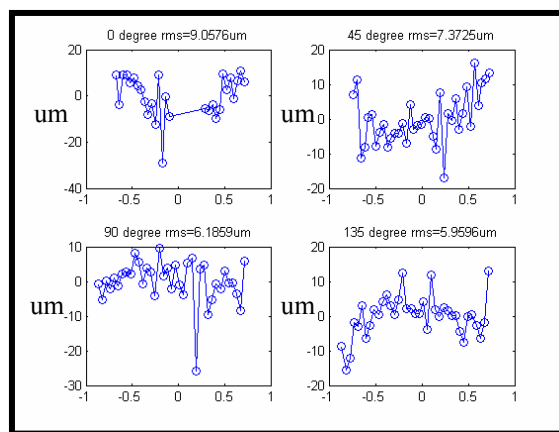
Figure 5.36 Spot diagram of the scanning data without compensations
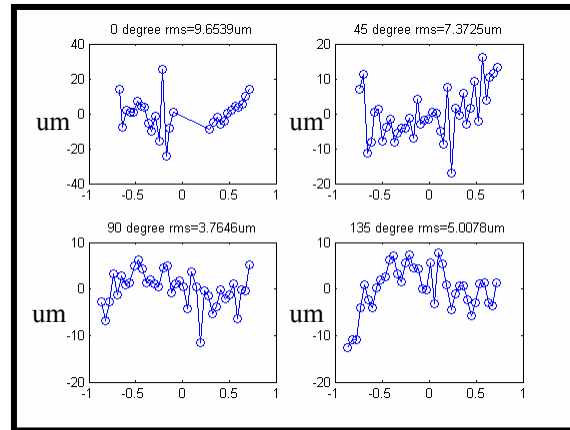
Figure 5.37 Spot diagram with compensation of high frequency errors
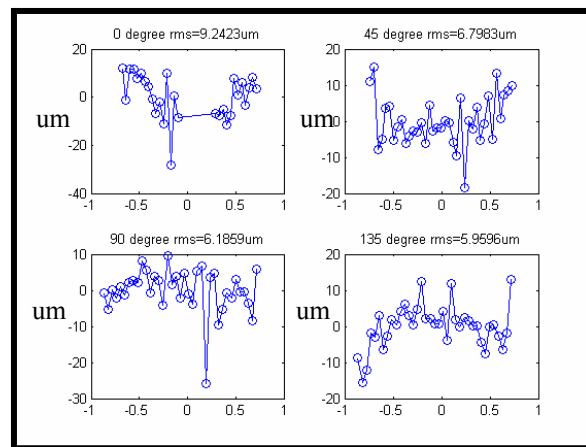
Figure 5.38 Spot diagram with compensation for motion of mirror and detector
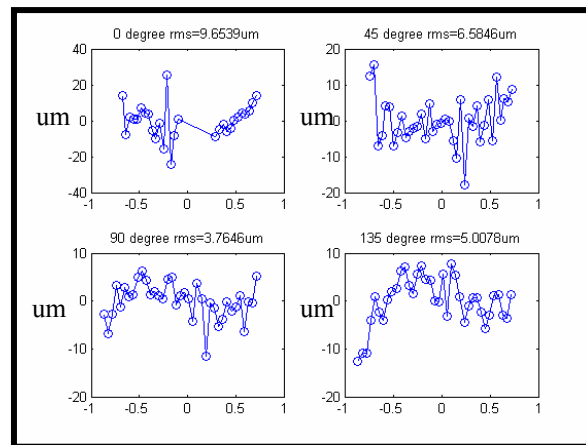
Figure 5.39 Spot diagram of the scanning data with both compensations
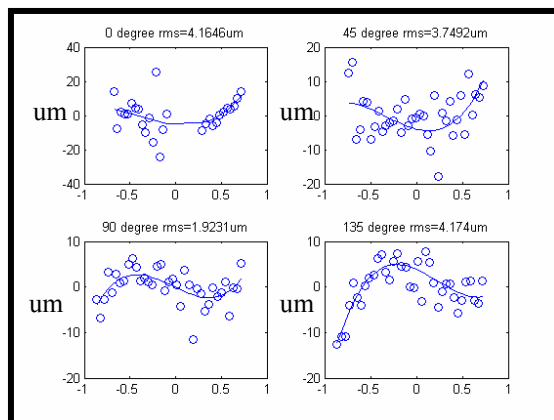
Figure 5.40 The fitting of the scanning data
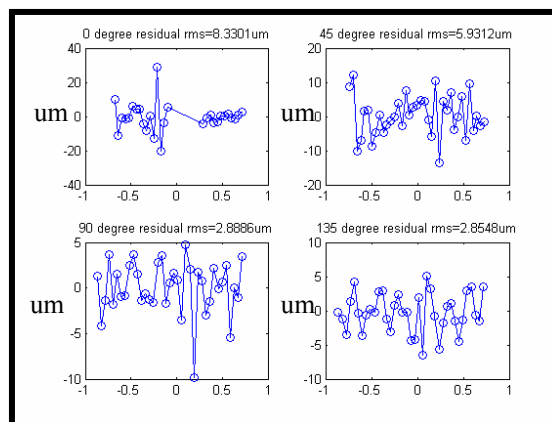
Figure 5.41 Residuals after removing polynomial fits and field aberrations
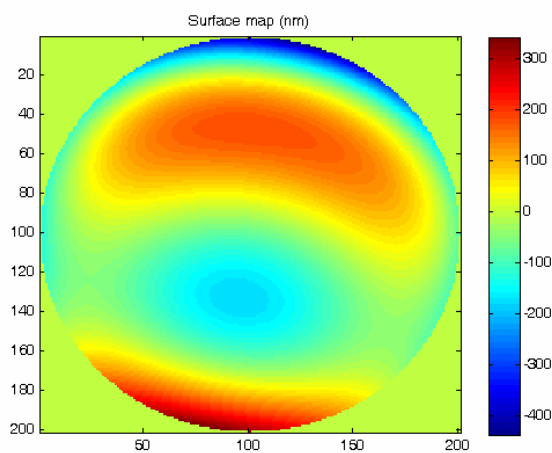
Figure 5.42 Surface estimate from the pentaprism test, rms=113nm

Table 5.3 Coefficients of the surface

Zernike Standard Polynomials	Surface coefficients (nm)
$\sqrt{6}\rho^2 \sin(2\theta)$	2
$\sqrt{6}\rho^2 \cos(2\theta)$	-12
$\sqrt{8}(3\rho^3 - 2\rho)\sin(\theta)$	-98
$\sqrt{8}(3\rho^3 - 2\rho)\cos(\theta)$	-16
$\sqrt{8}\rho^3 \sin(3\theta)$	32
$\sqrt{8}\rho^3 \cos(3\theta)$	23
$\sqrt{5}(6\rho^4 - 6\rho^2 + 1)$	-35
rms	**113**

5.3.5.2. MEASURING GEOMETRIC PARAMETERS

A complete measurement of the NST mirror also needs to give the mirror geometry, including radius curvature, off-distance, and clocking angle. This was investigated with equal optical path method.
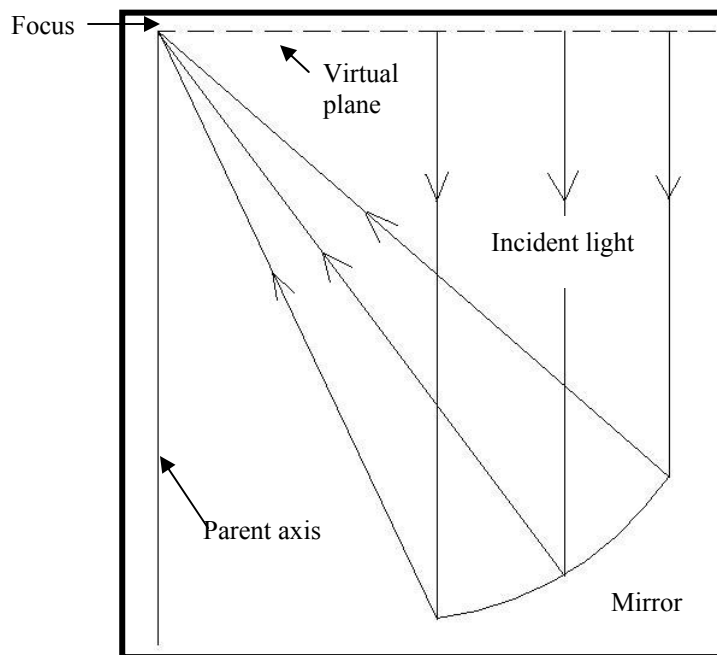
Figure 5.43 Equal optical path method

During the scanning pentaprism test, the rail was adjusted to focus the light to the same pixel in the detector, which corresponded to a certain field of view of the mirror. During data reduction, the field and focus alignment requirements can be obtained from the fitting. The focus of the mirror in the detector pixel plane can then be determined with the pixel position and alignment information. There were three tracker balls on the detector mount, and the coordinate relationship between the tracker balls and the detector pixel plane has been calibrated as discussed in Section 5.2.7. With the laser tracker, the coordinates of the balls on the detector and different positions on the mirror can be measured in the same coordinate system. Then the geometry between the focus of the mirror and the mirror can be determined.

Fig.5.43 shows the coordinate relations between the points on the mirror and the focus of the mirror. For on-axis light, the incident light is parallel to the parent axis of the mirror. A virtual plane passing through the focus of the mirror and perpendicular to its parent axis can be drawn as the dashed line shown in Fig. 5.43. This plane also intercepts the incident light at different points. The incident light is perpendicular to the virtual plane too. For a parabolic surface, different incident light should have same optical path from the point intercepted the virtual plane to the focus of the mirror. So the direction of the parent axis can be optimized to satisfy this requirement. With the direction of the parent axis and the coordinates of the symmetry marks known, the clocking angle of the mirror can then be calculated. With the laser tracker, the coordinates of the center of the mirror can be measured. The distance between the center and the focus gives the radius curvature of the mirror. And the distance between the center and the parent axis gives the off-axis distance of the mirror. A Monte Carlo simulation was done with a 0.1mm uncertainty of the focus and 5μm uncertainties of the coordinates on the mirror. A focal length uncertainty of less than 0.1mm and an off-axis distance uncertainty of less than 0.25mm were obtained. Experimental data was not collected yet when this dissertation was written.

5.4. ERROR ANALYSIS

The accuracy of the scanning pentaprism measurement is limited by random and systematic errors. The sources of these errors are described below.

5.4.1. CENTERING ERROR

The spot image motion was measured using a correlation method. There were 1.5µm *rms* errors in this determination. Since the spot center difference between the static and scanning pentaprism was measured, an uncertainty of 2.12µm *rms* ($\sqrt{2} \times 1.5$) for the spot location was expected. This was equivalent to 0.52urad *rms* slope error.

The effect of 1urad Gaussian random error was checked with a Monte Carlo analysis as shown in Table 5.4. In the experiments, some mirror edge points could not be sampled due to the configuration of the pentaprism test. This causes the estimate uncertainty in the experiment is relative larger than the situation where full aperture of the mirror is sampled as shown in the table.

Table 5.4 Monte Carlo analysis of 1urad random error

aberration	*rms* surface error (nm) Sample as in the experiment	*rms* surface error (nm) Sample uniformly
Focus	15	9
Sine Astigmatism	23	17
Cosine Astigmatism	23	17
Sine Coma	12	6
Cosine Coma	12	6
Sine Trefoil	35	20
Cosine Trefoil	30	17
Spherical aberration	8	4
RSS	**58**	**36**

5.4.2. ERROR INDUCED BY HIGH-FREQUNCY ERRORS IN THE MIRROR

As discussed in Section 5.3.4.2.4, high-frequency surface error was estimated from the interferometric measurement and then removed from the pentaprsim test data. Figure 5.44 shows the data from the interferometric measurement. Lower-order aberrations up to spherical aberration have been removed. Differential data was calculated along pentaprism scan lines in the interferometric phase map. The data was then divided by the separation to get the surface slopes. The slopes timing the focal length of the mirror give the spot displacements along a scan. These spot displacements as shown in Fig. 5.35 (blue curve) were subtracted from the pentaprism data. In the experiment, after removing the high-frequency data, surface fitting data and alignment data, the residuals in the 90° and 135° scans were 2.8μm or 0.69urad slope errors as shown in Fig.5.41. These included the 2.12 μm errors from the Centroid calculations, so the high-frequency residuals contributed ~1.7μm or 0.4urad slope errors in the 90° and 135° scans. For the 0° scan, after removing the point with biggest deviation, the residual shown in Fig.5.40 went down to ~ 4μm *rms*. Considering some data around the mirror center were lost due to blocking from the scanning pentaprism, higher residuals in the 0° scan are believed to be due to less data involved in the least squares estimate. High-frequency data was not well removed in the 45° scan; this was not well understood yet and more experiments are needed.

Treating the high-frequency data from interferometric measurement as random errors, a conservative estimate of their contribution to the measurement is 2.6μm or 0.64urad slope errors.
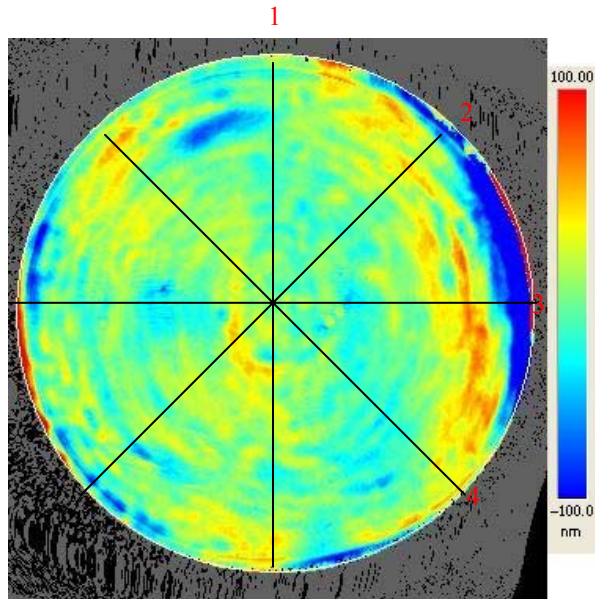
Figure 5.44 Interferometric test data (lower order aberrations up to spherical aberration were removed), rms=75nm

5.4.3. REMOVAL OF DETECTOR WINDOW ABERRATION

There is a protecting window with 850μm thickness in front of the detector pixels. The window introduces 2.5nm *rms* spherical aberration as simulated in ZEMAX. This spherical aberration was directly subtracted from the surface estimate result.

5.4.4. THERMAL ERRORS

Noah Siegel and Brian Cuerden (2003) have shown that a linear gradient of 0.01K /meter in the pentaprisms would cause the line of sight to deviate by 17nrad. Based on this, the temperature gradients in the prisms need to be limited to an acceptable level.

For the scanning pentaprism test, a single scan takes ~10 minutes. In the experiment, an allowable change of 0.2 K/m in the gradient was budgeted within the time of a scan. This gave 226nrad *rms* errors to the slope measurement. Here the prism saw different surfaces as it was driven along the rail, but the timescale was short compared to the prism's thermal time constant.

5.4.5. ERRORS FROM COUPLING LATERAL MOTION OF PRISMS

Phase or amplitude variations in the collimated beam from the beam projector do not affect the system performance to the first order because these effects are common to both prisms. However, these variations are coupled with lateral motion of the prism assembly relative to the collimated beam. In the experiment, the stop was set at the scanning prism so that the beam saw the same portion of the prism. This was done because the prism has more errors (index of refraction inhomogeneity, surface aberrations) than the beam.

Three basic couplings with lateral motion of the prism have been identified and analyzed (Mallik 2007):

1. Coupling of phase errors in the collimated beam with transverse motion of the prism.

2. Coupling of diffraction effects in the collimated beam with transverse motion of the prism.

3. Coupling of amplitude variations in the collimated beam with transverse motion of the prism.

These three effects give a change of slope that will be proportional to the lateral motion of the scanning pentaprism. The lateral motion of the prisms is likely to be systematic, with low-order dependence on scan position. The most troublesome error terms come from lateral motion that varies linearly and quadratically with scan position. A linear variation is interpreted as focus or astigmatism, while a quadratic variation is interpreted as coma and a cubic variation as spherical aberration.

We had a requirement for the straightness of the rail and aligned the pentaprism system to a tolerance as follows:

1 mm P-V linear variation from alignment with beam projector,

1 mm P-V quadratic variation from linearity across the full scan,

1 mm P-V cubic variation from linearity across the full scan,

0.25 mm *rms* variation from linearity after removing above terms.

The effect of the 0.25 mm *rms* residual is treated as a random error as in Section 5.4.1.

5.4.5.1. COUPLING OF PHASE ERRORS IN BEAM PROJECTOR

Phase errors in the wavefront are coupled to the prism motion according to the phase slope at the edge of the beam. Analysis shows this effect to be

$$\Delta\alpha = \frac{2\Delta x}{D}\frac{\partial W}{\partial r} \;. \tag{5.17}$$

where

$\Delta\alpha$ = effective change in beam angle

Δx = pupil shear

D = pupil diameter

$\dfrac{\partial W}{\partial r}$ = wavefront slope at the edge

5.4.5.2. COUPLING OF DIFFRACTION EFFECTS WITH LATERAL MOTION

A similar effect occurs due to diffraction as the collimated beam propagates. It cannot be eliminated by adjusting the beam projector's collimator because the slope at the edge of the beam varies with scan position. This may require using a smaller stop at the output face of the pentaprism. Prateek Jain (2003) shows that a 40mm stop on the output face reduces the error to 10nrad tilt in the deflected beam, for 1mm lateral displacement. The diffraction effects can thus be ignored compared with the effect of beam projector wavefront errors.

5.4.5.3. COUPLING FROM BEAM NON-UNIFORMITY

Using a stop on the pentaprism rather than at the beam projector makes the system nearly insensitive to wavefront errors in transmission through the pentaprism. A non-uniform intensity profile from the beam projector, however, acts like a soft stop fixed on the beam projector and creates a sensitivity to transmission through the pentaprism. Noah Siegel (2003) shows that a combination of 10% intensity variations, 1 mm lateral motion, and 122 nm quadratic error in the wavefront cause a 20nrad tilt error in the deflected beam.

5.4.5.4. LATERAL MOTION COUPLING ERRORS IN BEAM PROJECTOR DESIGN

The three coupling effects listed above have been considered in the design of the beam projector and the setting of the mechanical adjustment requirement.

From Equation 5.17 and simulations (Burge 2002) of the phase error coupling, the sensitivity to power and lateral displacement is 11μrad/mm/μm *rms*. With a 1mm lateral shift and 0.018 micron *rms* power (which corresponds to 50micron longitudinal defocus), a 0.2μrad error will be introduced. The sensitivity to Astigmatism is 7.8μrad/mm/μm *rms*. With 1mm lateral shift and 0.025micron *rms* astigmatism, a 0.2μrad error will be introduced, which corresponds to a 0.4° tilt of the lens. This analysis set the tolerance for aligning the beam projector.

Using a 20mm aperture at the pentaprisms, the diffraction effects can be ignored compared with the phase coupling effect.

By designing the beam projector with 0.05 *NA* and using only 20mm aperture, we control the light variation to less than 10%. Again the light irradiance variation effect can be ignored.

In the experiment, we slightly shifted the stop 1-2mm at the scanning pentaprism and checked the scan data variation before and after the changing. It showed around 2μm *rms* difference. Considering the 2μm *rms* variation already included the centering uncertainty discussed in Section 5.4.1, the beam projector error contribution can be ignored in the experiment.

5.4.6. FIELD AND FOCUS VARIATIONS BETWEEN THE SCANS

5.4.6.1. ERROR DUE TO FIELD VARIATION BETWEEN SCANS

During the test, the SPA was aligned to measure the same field of view of the mirror for all scans. This was done by focusing the light to the same pixel of the detector. In addition, the relative position changes between the mirror and the detector were monitored by the laser tracker and compensated numerically in the data reduction process.

The field variation effect has also been checked with a Monte Carlo simulation. Given a 25 micron measurement uncertainty in the laser tracker's absolute distance mode, a ±15.8urad field difference between each scan was randomly added to the simulation data. Tt produces an average wavefront error of 0.045micron *rms*, with 0.012micron *rms* power, 0.037micron *rms* astigmatism, 0.007 micron *rms* coma and 0.02micron *rms* trefoils.

Table 5.5 Effects of ±15.8 urad field variation between scans

aberration	*rms* system wavefront error (nm)
Focus	12
Astigmatism	37
Coma	7
Trefoil	20
Spherical aberration	0
RSS	**45**

5.4.6.2. ERROR DUE TO FOCUS VARIATION BETWEEN SCANS

System instability can also introduce defocus between the mirror and the detector. The effect of ±25microns defocus between each scan was checked with a Monte Carlo

analysis. It produces an average 0.12micron *rms* wavefront error, with 0.047micron *rms* power and 0.12micron astigmatism.

Table 5.6 Effects of ±25microns focus variation between scans

aberration	*rms* system wavefront error (nm)
Focus	47
Astigmatism	120
Coma	0
Trefoil	0
Spherical aberration	0
RSS	**120**

5.4.6.3. FIELD AND FOCUS VARIATION IN THE EXPERIMENT

From the tracker data, there is no apparent mirror tilt introduced. There was a ± 5μm uncertainty of the position change of the detector. It gave ± 1.2urad field variation between the scan. When aligning different scans to the same pixel (same field), a 0.5 pixel uncertainty was assumed, which corresponded to ±1urad field uncertainty. So in total, ±1.6urad field uncertainty was introduced in the test. From the Monte-Carlo analysis, it was known that ±15.8urad field variation will introduce a 45nm wavefront error, so a 2.25nm surface error due to field variation was introduced during the test. From the tracker data, a ±3μm focus uncertainty may exist, which corresponded to a 7.1 nm surface error.

5.4.7. ERROR DUE TO BEAM PROJECTOR PITCH

Due to the field aberration effect, when there was a beam projector pitch, the static spot and the scanning spot did not have the same amount of motion. Correction factors were calculated from the simulation, and these factors were verified by changing the pitch of the rail and checking the motion difference between the two spots. The factors matched to ~ 0.005. There were ~30urad (p-v) pitch motions in the test. With 30urad pitch motions and a 0.005 factor of uncertainty, pitch-induced slope errors were 0.15urad (p-v) or ~0.03urad *rms*.

5.4.8. ERRORS FROM MOTIONS AND MISALIGNMENT

There are only second order effects to the slope measurement due to angular motions and misalignment for the system. Table 5.7 lists the degrees of freedom of the sources of errors. Table 5.8 gives a summary of the error terms that couple to the measurement.

Table 5.7 Sources of errors due to angular motions and misalignment

	Pitch (x-shift for focal plane)	Yaw (y-shift for focal plane)	Roll
Beam projector	Yes	Yes	No
Prism	No	Yes	Yes
Focal plane	No	No	Yes

Table 5.8 Definition of alignment errors for prism system

Parameter	Description	Errors in the test
Beam projector pitch	It directly coupled into the slope measurement. It was fixed by using differential motion between the static and scanning pentaprisms. Its effect was further reduced by the numerical compensation discussed in Section 5.5.7	~0.03mrad *rms*
Δ(beam projector yaw)	Variation in beam projector line of sight in yaw direction	<0.4mrad *rms*
Prism yaw	Misalignment of prism in yaw direction due to initial alignment	<0.02mrad *rms*
Δ(Prism yaw)	Variation of yaw orientation for prism	<0.1mrad *rms*
Prism roll	Roll changes were removed with the feedback from the spot position variation in the camera	~0.4mrad
Focal plane roll	Determination of the in-scan direction	~0.5mrad

From Table 5.8, the slope measurement error is calculated as the sum in quadrature of the following terms:

$$(\text{prism yaw})^2$$

$$(\Delta\,(\text{prism yaw}) + \text{prism yaw}) \times \Delta\,(\text{beam projector yaw})$$

$$\text{prism roll} \times \Delta\,(\text{beam projector yaw})$$

$$\text{prism roll} \times \text{focal plane roll} \qquad\qquad (5.18)$$

The net slope error is 0.26 μrad rms.

5.4.9. ERROR CHECKING IN THE EXPERIMENTS

Several experiments were done to check the measurement errors in the NST pentaprism test.

One way was by making a scan of the surface and then flipping the rail and scanning the surface again. If the measurement errors were small, the results should be same for the two measurements, although some of the errors change sign as the rail was flipped. Fig. 5.45 shows the spot diagrams of the two scans and the difference between them. The *rms* difference before and after flipping the rail was 5µm. So the error in a single scan was ~3.5µm. This result was obtained before we stiffened the pitch of the rail and did not utilize measurement averaging. With those two improvements, the results should improve.
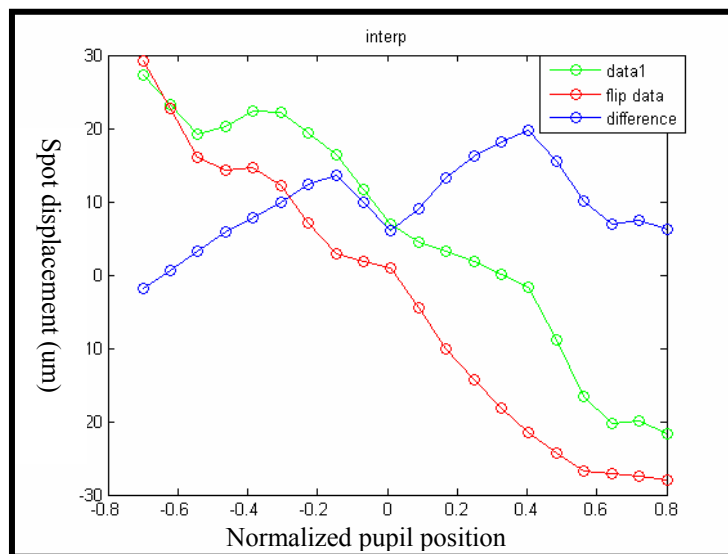
Figure 5.45 Error checking by flipping the rail

Measurement error was also checking by perturbing the alignment. In Fig. 5.46, the red curve was the measurement before perturbing the alignment. The green curve was

the measurement after the alignment was perturbed, where field aberration was introduced due to the misalignment. The blue curve was generated from the numerical simulation given the known misalignment. The difference between the measurement and the prediction was less than 4μm *rms*. So the error in a single scan was ~2.8μm. Again this result was obtained without measurement averaging.
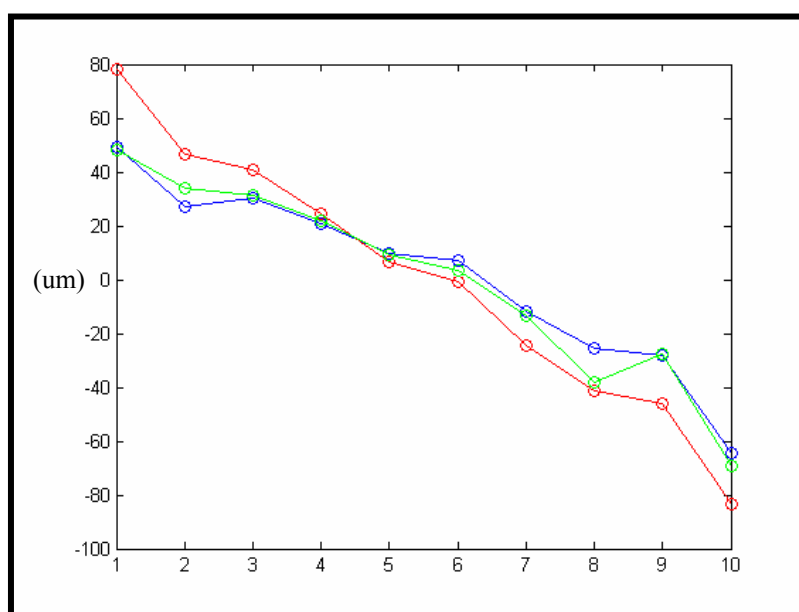
Figure 5.46 Error checking by perturbing the alignment

5.4.10. SUMMARY OF THE ERRORS

Table 5.9 and 5.10 summarize the different error sources. The total *rms* surface uncertainty of the test is estimated to be 53nm.

Table 5.9 Error described by surface rms

	Rms surface error (nm)	Explanation
Error due to field variation	2.25	±1.6 urad field difference between each scan
Error due to focus variation	7.1	±3 µm focus difference between each scan
RSS	**7.4 nm**	

Table 5.10 Error described by slope changes

	Scanning prisms (nrad *rms*)	Explanation
Centering error	523	1.5µm *rms* for each spot in focal plane
High frequency surface residuals	639	average 2.6 µm
Thermal effects	226	0.2 K/m
Coupling of phase errors in beam projector	neglectable	
Coupling diffraction effect with lateral motion		
Coupling of beam non-uniformity		
Motion and misalignment	260	Roll and yaw effect
RSS	**894 (52 nm rms surface error)**	

5.5. SUMMARY

The scanning pentaprism test has been successfully applied to measure flat and rotationally symmetric curved mirrors. Our work applied it to measure an off-axis surface which had significant amounts of field aberrations. Field aberrations introduce many new issues, as shown in Section 5.2 and Section on error analysis. They are now understood and solved experimentally and mathematically in our experiment. The scanning

pentaprism test is one of the verification tests for the GMT mirror. In that case, the surface is not a parabola, so the test will be a non-null test; however, the basic principle has been demonstrated in the NST test.

Finally, I would like to thank Jude, Rod and other people in Mirror Lab for helping in rotating the rail of the pentaprism test. During the early stage of the test, we rotated the rail many times each day in our efforts to more fully understand the system. I really appreciate their help and patience.

CHAPTER 6

SUMMARY

This dissertation describes some techniques developed at the University of Arizona for the absolute testing of large mirrors. These include a large flat mirror test, and two verification tests, a shear test and a scanning pentaprism test for aspheric mirrors. The principles, implementation, experimental results and error analysis of each test were described in detail. The maximum likelihood (ML) method, an important method used for data modeling and reduction, was explored from its principles to practical applications. It is useful as a general method to combine multiple interferometric measurements.

The ML method was used in the absolute test of a 1.6m flat. Errors in the reference surface were successfully separated from the flat under test. We measured the 1.6m flat mirror to 2nm *rms* accuracy. There is no limitation in extending the method to measure an even larger flat mirror (Yellowhair 2007). In the dissertation, finite terms of polynomials are used to represent surfaces in the ML method. This limits the description of local irregularities in the ML method. However, in principle, one can also use pixels as basis functions to describe surfaces. The disadvantage of a pixel basis is that it dramatically increases computing power and memory requirements. So an efficient basis is worth pursuing as future work.

The shear test described in Chapter 4 is an extension of the test for a rotationally symmetric surface. The data reduction method we developed can be used as a general tool for the shear test of an off-axis surface with an axis-symmetric parent. The shear test of a 1.7m off-axis parabolic mirror has obtained an accuracy of 12nm *rms*. In spite of the issue of basis functions for the ML method, the accuracy of the test was limited by the uncertainties in the single interferometric measurement of the lower order aberrations in the system. Deformations of the surfaces due to the change of the support need to be investigated and further addressed in data reduction.

We have successfully understood and controlled the field aberration issues in the scanning pentaprism test of the NST off-axis parabolic surface. The test error was well controlled to realize a 10nm measurement repeatability. The experience gained in testing the NST mirror will be very valuable for testing of GMT mirror segments in the future.

Techniques developed in this dissertation provide a framework for testing even larger flats and the GMT segments. New issues will surely arise, but the techniques developed here have laid the ground work for new analysis methods. New challenges in the fabrication will keep pushing metrology to new levels.

APPENDIX A

GENERAL LINEAR LEAST SQUARES AND VARIANCES OF THE ESTIMATE

(Press *et al.* chapter 15.4 1986)

A simple example of linear least squares fit is fitting data to a line ($a+bx$). The generalization of it is to fit a set of data points (x_i, y_i) to a linear combination of any specified functions of x. Here x is the coordinates of the data y, and x can be multidimensional, for instance, x is two dimensional when a wavefront map is to be fitted. Functions could be any forms, sines and cosines, Zernike polynomials or others. The general form of the linear least squares model is

$$y(x) = \sum_{k=1}^{M} a_k X_k(x) \qquad (A.1)$$

where $X_k(x)$ = any arbitrary fixed functions of x, called the basis functions.

The functions $X_k(x)$ can be nonlinear; the 'linear' of the least squares refers to that the model linearly depends on parameters a_k.

Solving Equation A.1 in a least squares sense, a merit function can be defined as

$$\chi^2 = \sum_{i=1}^{N} [\frac{y_i - \sum_{k=1}^{M} a_k X_k(x_i)}{\sigma_i}]^2 \qquad (A.2)$$

where σ_i =is the measurement error (standard deviation) of the ith data point,

presumed to be known. If the error levels are same for all the

measurements, σ_i can be set to a constant value $\sigma_i = 1$.

The parameters a_k can be estimated by minimizing χ^2. One way to find minimum is by

solving Normal equations as following derivations.

Let A be a matrix whose $N \times M$ components are constructed from the M basis

functions evaluated at the N coordinates x_i, and from the N measurements errors σ_i. Its

component can be written as

$$A_{ij} = \frac{X_j(x_i)}{\sigma_i} \quad . \qquad\qquad (A.3)$$

In general A has more rows than columns, $N > M$, since there must be more data points

than model parameters to be solved for.

A data vector b of length N can be defined as

$$b_i = \frac{y_i}{\sigma_i} \quad . \qquad\qquad (A.4)$$

And a solution vector a with length M can be composed from a_1, ..., a_M.

The minimum of χ^2 occurs where the derivative of it with respect to all M

parameters a_k vanishes. This condition yields the M equations

$$0 = \sum_{i=1}^{N} \frac{1}{\sigma_i^2} [y_i - \sum_{j=1}^{M} a_j X_j(x_i)] X_k(x_i) \qquad k = 1,...,M \qquad (A.5)$$

Interchanging the order of the summations, Equation A.5 can be written as the matrix

equation

$$\sum_{j=1}^{M} \alpha_{kj} a_j = \beta_k \tag{A.6}$$

where $\qquad \alpha_{kj} = \sum_{i=1}^{N} \dfrac{X_j(x_i)X_k(x_i)}{\sigma_i^2}$ or equivalently $[\alpha] = A^T \cdot A$ an $M \times M$ matrix,

$$\beta_k = \sum_{i=1}^{N} \dfrac{y_i X_k(x_i)}{\sigma_i^2} \qquad \text{or equivalently } [\beta] = A^T \cdot b \text{ a vector of length } M.$$

Equation A.5 or A.6 are called the normal equations of the least squares problem. They can be solved by *LU* decomposition, backsubstitution or other standard matrix methods. In matrix form, the normal equations can be written as

$$[\alpha] \cdot a = [\beta] \qquad or (A^T \cdot A) \cdot a = A^T \cdot b \tag{A.7}$$

The inverse matrix $C_{jk} = [\alpha]_{jk}^{-1}$ is closely related to the estimate uncertainty of the parameters **a**. parameters a_j can be solved as

$$a_j = \sum_{k=1}^{M} [\alpha]_{jk}^{-1} \beta_k = \sum_{k=1}^{M} C_{jk} [\sum_{i=1}^{N} \dfrac{y_i X_k(x_i)}{\sigma_i^2}] \tag{A.8}$$

The variance associated with the estimate a_j can be found from

$$\sigma^2(a_j) = \sum_{i=1}^{N} \sigma_i^2 (\dfrac{\partial a_j}{\partial y_i})^2 \tag{A.9}$$

Note that α_{jk} is independent of y_i, so that from Equation A.8 we obtain

$$\dfrac{\partial a_j}{\partial y_i} = \sum_{k=1}^{M} \dfrac{C_{jk} X_k(x_i)}{\sigma_i^2} \tag{A.10}$$

This leads to

$$\sigma^2(a_j) = \sum_{k=1}^{M} \sum_{l=1}^{M} C_{jk} C_{jl} [\sum_{i=1}^{N} \dfrac{X_k(x_i)X_l(x_i)}{\sigma_i^2}] \tag{A.11}$$

The final term in brackets is just the matrix $[\alpha]$. Since this is the matrix inverse of $[C]$, so

Equation A.11 reduces to

$$\sigma^2(a_j) = C_{jj} \qquad\qquad (A.12)$$

So the diagonal elements of $[C]$ are the variances of the fitted parameters **a**.

REFERENCES

Ai, C. and J. C. Wyant, "Absolute testing of flats using even and odd functions," Appl. Opt. **32,** 4698–4705 (1993).

Barrell, H. and R. Marriner, "Liquid surface interferometry," Nature (London) **162,** 529–530 (1948).

Barrett, Harrison H., Christopher Dainty, David Lara, "Maximum-likelihood methods in wavefront sensing: stochastic models and likelihood functions,**"** J. Opt. Soc. Am. A, Vol. 24, No. 2 (February 2007)

Born, M. and E. Wolf, Principle of Optics, Cambridge university press, p905 (1999)

Bray, M., "Stitching interferometer for large plano optics using a standard interferometer," Proc. SPIE **3134**, 39–50 (1997).

Burge, J. H., *Advanced Techniques for Measuring Primary Mirrors for Astronomical Telescopes*, Ph. D. Dissertation, Optical Sciences, University of Arizona (1993).

Burge, Jim, "Change in effective wavefront tilt due to lateral translation of the stop for low order Zernike wavefront aberrations, Rev. 2," Internal technical memo (Dec. 19, 2002)

Burge, J. H., L. B. Kota, H. M. Martina, R. Zehnder, C. Zhao, "Design and analysis for interferometric measurements of the GMT primary mirror segments, " Optomechanical Technologies for Astronomy, edited by Eli Atad-Ettedgui, Joseph Antebi, Dietrich Lemke, Proc. of SPIE Vol. 6273, 62730M (2006)

Burge, J. H., L. B. Kot, H. M. Martin, C. Zhao, T. Zobrist, "Alternate surface measurements for GMT primary mirror segments, " Optomechanical Technologies for Astronomy, edited by Eli Atad-Ettedgui, Joseph Antebi, Dietrich Lemke, Proc. of SPIE Vol. 6273, 62732T, (2006)

Chen, Shanyong, Shengyi Li, and Yifan Dai, "Iterative algorithm for subaperture stitching interferometry for general surfaces," J. Opt. Soc. Am. A, Vol. 22, No. 9, p1929-1936, (September 2005)

Chow,W. W. and G. N. Lawrence, "Method for subaperture testing interferogram reduction," Opt. Lett. **8**, 468–470 (1983).

Elssner, Karl-Edmund, R. Burow, J. Grzanna, and R. Spolaczyk, "Absolute sphericity measurement," APPLIED OPTICS, Vol. 28, No. 21, p4649-4661 (November 1989)

Evans, C. J. and R. N. Kestner, "Test optics error removal," Appl. Opt. **35,** 1015–1021 (1996)

Fleig, Jon, Paul Dumas, Paul E. Murphy, Greg W. Forbes, "An automated subaperture stitching interferometer workstation for spherical and aspherical surfaces," Advanced Characterization Techniques for Optics, Semiconductors, and Nanotechnologies, edited by Angela Duparré, Bhanwar Singh, SPIE Vol. 5188, p296-307 (2003)

Frieden, B. Roy, *Probability, Statistical Optics, and Data Testing*, Springer press p389 (1990)

Fritz, Bemard S., "Absolute calibration of an optical flat," Optical Engineering, Vol. 23 No.4, p379-383 (August 1984).

Golini, Donald, *et al*, "Method for self-calibrated sub-aperture stitching for surface figure measurement," United States patent application publication, Pub. No: 0117632 (2003)

Griesmann, Ulf, "Three-flat test solutions based on simple mirror symmetry," APPLIED OPTICS,Vol. 45, No. 23, p5856-5865 (August 2006)

Hou, Xi, Fan Wu, Li Yang, Shibin Wu, and Qiang Chen, "Full-aperture wavefront reconstruction from annular subaperture interferometric data by use of Zernike annular polynomials and a matrix method for testing large aspheric surfaces," APPLIED OPTICS, Vol. 45, No. 15, p3442-3455 (May 2006)

Jain, Prateek, "(LOTIS) Hartman Spot Position Sensing," internal technical memo (June 2002)

Jain, Prateek, "LOTIS scanning pentaprism and diffraction effects," Internal technical memo (May 15, 2003)

Jensen, S. C., W. W. Chow, and G. N. Lawrence, "Subaperture testing approaches: a comparison," Appl. Opt. **23**, 740–745 (1984).

Johns Matt, "The Giant Magellan Telescope (GMT)," in Ground-based and Airborne Telescopes, edited by Larry M. Stepp, Proc. of SPIE Vol. 6267, 626729 (2006)

Kim, C. and J. Wyant, "Subaperture test of a large flat on a fast aspheric surface," J. Opt. Soc. Am. **71**, 1587 (1981).

Kim, Taehee, James H. Burge, Yunwoo Lee, "Measurement of Highly Parabolic Mirror using Computer Generated Hologram," Interferometry XI: Applications, Wolfgang Osten, Editor, Proceedings of SPIE Vol. 4778 p119-126 (2002)

Mallik, Proteep C. V., Chunyu Zhao, James H. Burge, "Measurement of a 2-meter flat using a pentaprism scanning system," Optical Engineering 46(2), 023602 (February 2007)

Martin, H. M., J. H. Burge, B. Cuerden, S. M. Miller, B. Smith, C. Zhao, "Manufacture of 8.4 m off-axis segments: a 1/5 scale demonstration," Optical Fabrication, Metrology, and Material Advancements for Telescopes, edited by Eli Atad-Ettedgui, Philippe Dierickx, Proceedings of SPIE Vol. 5494, p62-70 (2004)

Martin, H. M., J. H. Burge, S. M. Miller, B. K. Smith, R. Zehnder, C. Zhao, "Manufacture of a 1.7 m prototype of the GMT primary mirror segments," Optomechanical Technologies for Astronomy, edited by Eli Atad-Ettedgui, Joseph Antebi, Dietrich Lemke, Proc. of SPIE Vol. 6273, 62730G, (2006)

Palusinski, Iwona A., Jose´ M. Sasia´n, "Sag and phase descriptions for null corrector Certifiers," Opt. Eng. **43**(3) 697–701 (March 2004)

Parks, R. E., "Removal of test optics errors," in Advances in Optical Metrology, N. Balasubramanian and J. C. Wyant, eds., Proc. SPIE **153,** 56–63 (1978).

Parks, Robert E., Lianzhen Shao, and Chris J. Evans, "Pixel-based absolute topography test for three flats," APPLIED OPTICS, Vol. 37, No. 25, p5951-5965 (September 1998)

Powell, Ian and Emmanuelle Goulet, "Absolute figure measurements with a liquid-flat reference," APPLIED OPTICS, Vol. 37, No. 13, 2579-2588 (May 1998)

Press, William, Brian Flannery, Saul Teukolsky, William Vetterling, *Numerical Recipes*, Cambridge University Press (1986)

Reichelt, Stephan, Christof Pruss, and Hans J. Tiziani, "Absolute interferometric test of aspheres by use of twin computer-generated holograms," APPLIED OPTICS, Vol. 42, No. 22, p 4468-4479 (August 2003)

Schulz, G. and J. Schwider, "Precise measurement of planeness," Appl. Opt. **6,** 1077–1084 (1967)

Schulz, G. and J. Schwider, *Progress in Optics XIII*, chapter 3, North Holland, Amsterdam (1976)

Siegel, Noah, "Analysis of Scanning and Staring Pentaprism Tests: Noise and Aliasing simulations Rev. 2**,**" Internal technical memo (May 15, 2003**)**

Siegle, Noah, "Thermal Gradient Effects on Line of Sight Error, Rev. 2," Internal technical memo (June 30, 2003)

Sprowl, Robert A., *Sub-Aperture Fizeau Test for a 1.6 Meter Flat*, Master degree report (May 2006)

Stuhlinger, T. W., "Subaperture optical testing: experimental verification," Proc. SPIE **656**, 118–127 (1986).

Su, Peng, Josh Hudman, Jose M. Sasian and William J. Dallas, "Dual beam generation at a ray caustic by a multiplexing computer-generated hologram," OPTICS EXPRESS Vol. 13, Issue 13, pp. 4843-4847 (2005)

Su, Peng, Jim Burge, Robert A. Sprowl and Jose Sasian, "Maximum likelihood estimation as a general method of combining sub-aperture data for interferometric testing," International Optical Design Conference 2006, edited by G. Groot Gregory, Joseph M. Howard, R. John Koshel, SPIE Vol. 6342, 63421X (2006)

Su, Peng, James H. Burge, Jose Sasian, "Shear test of the off-axis surface with an axis-symmetric parent," Optical Manufacturing and Testing VII, edited by James H. Burge, Oliver W. Faehnle, Ray Williamson, Proc. of SPIE Vol. 6671, 66710R, (2007)

Thunen, J. G. and O. Y. Kwon, "Full aperture testing with subaperture test optics," Proc. SPIE **351**, 19–27 (1982).

Toronto, Maria, "review of various MTF measurement methods comparison of bar target variance and modulation", MS thesis, OSC QC350 O77 Vol. 274 (1995)

Wikipedia, http://en.wikipedia.org/, 2007

Yellowhair, Julius, Peng Su, Robert Sprowl, Robert Stone, Jim Burge, "Development of a 1 meter vibration insensitive Fizeau interferometer, " to be submitted to Optical Express (2007)

Zehnder, Rene, James H. Burge and Chunyu Zhao, "Use of computer generated holograms for alignment of complex null Correctors," Optomechanical Technologies for Astronomy, edited by Eli Atad-Ettedgui, Joseph Antebi, Dietrich Lemke, Proc. of SPIE Vol. 6273, 62732S, (2006)

Zhao, Chunyu, Rene Zehnder, James H. Burge, Hubert M. Martin, "Testing an off-axis parabola with a CGH and a spherical mirror as null lens," Optical Manufacturing and Testing VI, edited by H. Philip Stahl, Proc. of SPIE Vol. 5869 (2005)

Zhao, Chunyu, Robert A. Sprowl, Michael Bray, James H. Burge, "Figure measurement of a large optical flat with a Fizeau interferometer and stitching technique," Interferometry XIII: Applications, edited by Erik L. Novak, Wolfgang Osten, Christophe Gorecki, Proc. of SPIE Vol. 6293, 62930K (2006)